

Engineered Magnetoconductance in InAs Nanowire Quantum Dots

Inauguraldissertation

zur
Erlangung der Würde eines Doktors der Philosophie
vorgelegt der
Philosophisch-Naturwissenschaftlichen Fakultät
der Universität Basel

VON

Gábor Fábrián
aus Serbien und Ungarn

Basel, 2016

Originaldokument gespeichert auf dem Dokumentenserver der Universität Basel
<http://edoc.unibas.ch>



Dieses Werk ist lizenziert unter einer [Creative Commons Namensnennung - Nicht kommerziell
- Keine Bearbeitungen 4.0 International Lizenz](https://creativecommons.org/licenses/by-nc-nd/4.0/).

Genehmigt von der Philosophisch-Naturwissenschaftlichen Fakultät
auf Antrag von
Prof. Dr. C. Schönenberger
Prof. Dr. J. Nygård
Prof. Dr. T. Schäpers

Basel, 15.9.2015

Prof. Dr. Jörg Schibler
Dekan



Namensnennung-Keine kommerzielle Nutzung-Keine Bearbeitung 3.0 Schweiz
(CC BY-NC-ND 3.0 CH)

Sie dürfen: Teilen — den Inhalt kopieren, verbreiten und zugänglich machen

Unter den folgenden Bedingungen:



Namensnennung — Sie müssen den Namen des Autors/Rechteinhabers in der von ihm festgelegten Weise nennen.



Keine kommerzielle Nutzung — Sie dürfen diesen Inhalt nicht für kommerzielle Zwecke nutzen.



Keine Bearbeitung erlaubt — Sie dürfen diesen Inhalt nicht bearbeiten, abwandeln oder in anderer Weise verändern.

Wobei gilt:

Verzichtserklärung — Jede der vorgenannten Bedingungen kann **aufgehoben** werden, sofern Sie die ausdrückliche Einwilligung des Rechteinhabers dazu erhalten.

Public Domain (gemeinfreie oder nicht-schützbarer Inhalte) — Soweit das Werk, der Inhalt oder irgendein Teil davon zur Public Domain der jeweiligen Rechtsordnung gehört, wird dieser Status von der Lizenz in keiner Weise berührt.

Sonstige Rechte — Die Lizenz hat keinerlei Einfluss auf die folgenden Rechte:

- Die Rechte, die jedermann wegen der Schranken des Urheberrechts oder aufgrund gesetzlicher Erlaubnisse zustehen (in einigen Ländern als grundsätzliche Doktrin des **fair use** bekannt);
- Die **Persönlichkeitsrechte** des Urhebers;
- Rechte anderer Personen, entweder am Lizenzgegenstand selber oder bezüglich seiner Verwendung, zum Beispiel für **Werbung** oder Privatsphärenschutz.

Hinweis — Bei jeder Nutzung oder Verbreitung müssen Sie anderen alle Lizenzbedingungen mitteilen, die für diesen Inhalt gelten. Am einfachsten ist es, an entsprechender Stelle einen Link auf diese Seite einzubinden.

Acknowledgements

Almost 4 years have passed since I embarked on my journey towards the culmination of my PhD project, the present thesis. Ambivalently, it seems like this time just flew away, yet also as if ages have passed since I moved to Basel. I feel I have learned an immense amount about not just my field of research but about myself as well.

Firstly, I have to express my gratitude towards Prof. Christian Schönenberger for giving me the opportunity to take part in world-class research, meet leading physicists, and investigate an interesting and challenging topic in our field. It never ceases to amaze me how much passion he has for physics and nanoscience, and still "getting his hands dirty" with hands-on research. Furthermore, he has always put emphasis on group activities, and I really appreciated the group skiing trips and excursions (except the seemingly common theme of summer rain).

I thank my referees Prof. Thomas Schäpers, Prof. Jesper Nygård for taking the time to read and appraise this thesis, and for giving comments on possible improvements.

I am immensely grateful to Andreas Baumgartner for the day-to-day supervision during the thesis. He has never failed to bring new ideas for improvements and to motivate me when I had my moments of doubt. Although at the time I might not have been as appreciative, I feel I have, under his tutelage, greatly improved my skills and style of presenting my research in scientific writing, posters, and talks. Without his help, many of the results in this thesis would not have been possible. Péter Makk also deserves a vast amount of credit. In a manner of speaking, he has gone above and beyond the call of duty in providing assistance and support without hesitation whenever I needed it.

The research in this thesis would also have not been possible without the high-quality material that was provided by our colleagues at the Niels Bohr Institut in Copenhagen: Morten Hannibal Madsen and Prof. Jesper Nygård. Nanowire placement, using micromanipulators would not have been possible without Prof. Martino Poggio letting us use his group's lab facilities.

In a way, I took over the torch of carrying the semiconducting nanowire project in the group from Samuel d'Hollosy. He introduced me to the methods and techniques, and I learnt the tools of this trade as his "apprentice". I am happy that I could work in tandem with such a skilled colleague. Soon this torch will be passed on to Christian Jünger, who I thank for his help with the measurements of the cobalt side gate devices.

Simon Zihlmann and Péter Makk have provided invaluable help with characterizing the magnetic structures used in this thesis. Without the experience of Peter Rickhaus and Romain Maurand regarding the use and applications of LOR, my task to develop quasi-suspended contacts would have been much more daunting, I thank them for sharing their know-how for this resist. I am grateful to Hagen Aurich, Julia Samm, and Jörg Gramich for the experience in using Permalloy which I have inherited from them

and I have to specifically mention Jörg Gramich who made significant improvements to our sample fabrication process by developing the protocol for the use of ZEP520.

I also acknowledge all the people who have been part of the group and have in some way woven themselves into the tapestry of my time as a PhD student: Matthias Bräuninger, Frank Freitag, Stefan Nau, Jens Schindele, Minkyung Jung, Markus Weiss, Gulbostan Abliz, Clevin Handschin, Thomas Hasler, Mihai-Cezar Harabula, Vishal Ranjan, Samuel Hess, Jan Overbeck, Ralph Stoop, Mathias Wipf, Claire Barrett, Jan Brunner, Toni Fröhlich, Wangyang Fu, Cornelia Nef, Alexey Tarasov, Axel Fanget, Maria El Abbassi, Kishan Thodkar, and Anton Vladyka.

I am indebted to all the people who have helped in proof-reading the thesis at various points of its evolution, helped to spot plenty of absent-minded mistakes I would have never noticed, and also improved the thesis with helpful comments and criticism: Andrew Horsley, Péter Szirmai, Gergő Fülöp, András Deák, Péter Boross, Péter Kovács, Samuel d'Hollosy and Vishal Ranjan. I have to give special thanks to Andreas Baumgartner for providing guidance in writing and playing an instrumental role in how the thesis took its current form, and Péter Makk, who combed through so many versions of the thesis, that I lost track after a while.

The tasks of a researcher is not limited to science but many administrative issues also pose a considerable burden. Luckily, the Physics Department is fortunate enough to have people like Ms. Barbara Kammermann and Ms. Astrid Kalt, who have always been helpful in navigating the treacherous waters of bureaucracy and subsequently made it easy for us to focus on science.

I would not have gotten here without former mentors, who have helped start my scientific career. The groundwork for my journey in physics was laid out by my primary school physics teacher, Mrs. Aranka Amstadt, who went above and beyond the call of duty in her extracurricular study sessions. The experience I gained during summer internships in the group of Prof. László Forró has proven invaluable by giving me insight into different aspects of cutting-edge research. I acknowledge the role of Prof. Szabolcs Csonka, whose course introduced me to the field of quantum electronics and the work of the Nanoelectronics group in Basel. Most importantly, the infectious enthusiasm of Prof. Ferenc Simon and our fruitful work during my Bachelor's and Master's projects was instrumental in my decision to pursue a PhD degree. I am immensely grateful for his help in getting my professional career started.

Last but not least, I dedicate this thesis to all the family and friends who have given constant unwavering support in times of personal or professional turmoil. I cannot overestimate the importance of their patience towards me even at stressful times, which has helped me tremendously in the last few weeks of the thesis writing process.

Contents

Acknowledgements	v
Contents	viii
1. Introduction	1
2. Theoretical Background	7
2.1. Ferromagnetism	7
2.1.1. Microscopic origin: Exchange interaction, Stoner model	8
2.1.2. Magnetic anisotropies	9
2.1.3. Stoner–Wohlfahrt model	11
2.1.4. Magnetoresistance effects	12
2.2. Quantum dots	15
2.2.1. Basics of quantum dots	16
2.2.2. The Kondo effect	20
2.2.3. Quantum dot states in magnetic field	21
2.2.4. Magnetotunnelling	22
2.2.5. Magneto-Coulomb Effect	23
2.2.6. Double quantum dots	24
3. Indium Arsenide Nanowires	27
3.1. Nanowire growth	27
3.2. Magnetotransport experiments in nanowires	30
4. Fabrication and experimental techniques	33
4.1. Device fabrication	33
4.1.1. Nanowire deposition and location	33
4.1.2. Lift-off technique	35
4.1.3. Wire bonding	37
4.2. Experimental setup	37
4.2.1. Cryogenic techniques	38
4.2.2. Measurement setup	39
5. g-factor Anisotropy in InAs Nanowire Quantum Dots	43
5.1. Experimental results	45
5.1.1. Zeeman shift of resonance position	45
5.1.2. Kondo Splitting	47
5.1.3. Discussion	48
5.2. Summary	50

6. Quasi-suspended Ferromagnetic Contacts for InAs NW Spin-valve Devices	51
6.1. Fabrication of quasi-suspended contacts	52
6.2. Magnetic properties	53
6.3. Electrical contact, quantum dot formation	55
6.4. Magnetoconductance measurements	57
6.5. Applicability and shortcomings	58
6.6. Summary	58
7. InAs Nanowire Device with Normal Metal Side Gates	59
7.1. Device specifics	60
7.2. Electrical tuning via side gates	60
7.3. Magnetic field dependence	63
7.4. Summary	65
8. Magnetic Side Gating of InAs Nanowire	67
8.1. Device specifics	68
8.2. Magnetic properties of Permalloy side gate pairs	69
8.3. Zero-field conductance characteristics	71
8.4. Overview of magnetotransport features	76
8.5. Magnetoconductance in different regimes	81
8.5.1. Single-dot regime	81
8.5.2. Strongly coupled double-dot regime	83
8.5.3. Weakly coupled double-dot regime	85
8.6. Discussion	89
8.6.1. From amplitudes and widths to tunnel couplings	89
8.6.2. Effects behind changes in the coupling	91
8.6.3. Model of local DOS for strongly coupled double dots	94
8.6.4. Toy model for magnetoconductance changes from ground-state transitions	97
8.7. Outlook: cobalt side gates	101
8.8. Conclusions	105
9. Summary and outlook	107
Bibliography	109
A. Fabrication Recipes	121
A.1. Wafer Characteristics	121
A.2. Wafer Cleaning	121
A.3. EBL Process for PMMA	121
A.4. EBL Process using ZEP	122
A.5. O ₂ Plasma cleaning	122
A.6. Argon Ion Beam Milling	122
Curriculum Vitae	125
Publications	127

1 Introduction

Magnetoconductance (or magnetoresistance) is the change in the electrical transport properties of a solid state system in response to an applied magnetic field, determined by both its magnitude and orientation. Such effects arise in many shapes and forms, depending on how the magnetic field couples to the charge carriers and thus affect the resistance.

The most straightforward manifestation of the B magnetic field is its effect on the trajectories of charged particles via the Lorentz force, demonstrated in the Hall effect [1]. The magnetic field can also affect the electron phase indirectly, via its vector potential, leading to quantum interference effects like in the Aharonov–Bohm effect [2]. The magnetic field also couples to another intrinsic attribute of the electrons – the *spin* – leading to the Zeeman splitting [3] of two quantized energy levels. The range of magnetoresistive phenomena are considerably expanded with the incorporation of magnetic materials as contacts. In this case, the magnetic field will also couple to the magnetization of the material, indirectly affecting the transport properties. This approach allows the engineering of well-controlled changes in transport, which has made it highly attractive for applications.

Magnetoresistive devices – spearheaded by the discovery of *giant magnetoresistance (GMR)* [4, 5] – have been successfully applied in information storage, creating improved hard drive read heads. The observation of such spin-based magnetoresistance phenomena has led to the emergence of the field of spintronics [6] – or spin transport electronics –, an interdisciplinary field on the interface of magnetism and electronics. Spintronics aims to harness the electron’s spin degree of freedom in addition to its charge, opening up new avenues of information storage and processing. Magnetic tunnel junctions show great promise for new generations of read heads, as well as magnetic memories (MRAM) using the phenomenon of spin transfer torque (STT) [7]. Advances in semiconductor spintronics [8, 9] are pivotal for the realization of spin logic, based on the concept of a Datta–Das spin field effect transistor [10, 11], which envisages the control of the spin channel by electric means.

As one moves to nanoscale objects which can support single spins, the quantum nature of the spins becomes prominent [12]. Quantum dots (QDs) [13, 14] provide a well-controlled platform for the study of single electron spins and spin-polarized currents. Coupling a quantum dot to two spin-polarized contacts in a spin-valve geometry, one can achieve spin injection and detection to probe the spin physics of the nanostructure. Conversely, the well-controlled nature of quantum dots allows one to affect the conduction channel connecting the injector and detector, providing means for the electrical control of spin currents [15–17]. Furthermore, the spin of an electron

stored in a quantum dot can be used as a so-called *spin qubit*, a device for storing and manipulating information in quantum computers [18, 19].

Therefore, investigating the magnetoconductance of nanoscale objects is interesting on multiple levels: understanding the intrinsic magnetoconductance of the structure, using magnetoconductance phenomena to probe it, and then turning it around and using the nanostructure to affect the manifestation of magnetotransport.

InAs nanowires provide a versatile platform which allows one to address different details of magnetoconductance. As indium arsenide does not form Schottky barriers at metal interfaces, achieving ohmic contact to ferromagnets does not pose an obstacle [20]. Owing to their large g factor [21, 22], its electron spins are strongly affected by magnetic fields. Furthermore, the presence of strong spin-orbit interaction [23, 24] carries the possibility of controlling electron spins [25] and magnetoconductance using electric fields.

In this thesis, we investigate various aspects of magnetoconductance arising in quantum dots defined in InAs nanowires. Firstly, the direct coupling of the spins and the external magnetic field is addressed by examining the g factor in InAs nanowire quantum dots. Secondly, we explore nanowire-based quantum dot spin-valve devices, where the magnetic field affects the conductance through the magnetization of the ferromagnetic leads, focusing on the novel fabrication aspects of our devices. Thirdly, the combined effect of local electric and magnetic fields is investigated in depth for devices with ferromagnetic split-gate geometries. This approach utilizes the locally strong magnetic stray fields of ferromagnetic nanostructures. Such a scheme can be used to address novel concepts like fractional fermions [26–28] or entanglement detection [29] of split electron pairs generated by a Cooper pair splitter [30, 31].

The magnetoconductance of a device can be changed directly by the magnetic field affecting the electron spin. This coupling strength is formulated in the so-called g factor, which determines the magnitude of the Zeeman splitting [3] between spin-degenerate levels. It plays an instrumental role in the magnetoconductance of a quantum dot, as magnetic field evolution of the quantum dot spectrum. The g factor is strongly influenced by the band structure and confinement potential, and has been shown to be strongly anisotropic [22, 32] and state-dependent [21, 32] in InAs quantum dots. Thus, the energy difference between the spin-up and spin-down levels will vary as a function of the magnetic field. Understanding the nature of this orientation dependence and the factors behind it is essential for finding the optimal field direction for maximal spin splitting. Furthermore, controlled modulation of the g factor is crucial for the selective addressing of spin qubits [33]. Here, the orientation dependence of the g factor is examined using two methods for two different charge states of an InAs nanowire quantum dot. We find considerable anisotropy which varies between charge states. This work – performed in tandem with S. d’Hollosy –, was published in Ref. [34]. A similar study on self-assembled InAs nanowires was published by Takahashi *et al.* concurrently.

Spin valves are one of the most simple magnetoresistive devices and offer a straightforward method of investigating the spin physics in solid state systems through spin-polarized currents. The two ferromagnetic contacts of the spin valve serve as analogues of a polarizer and analyzer in optics. By engineering the magnetic

properties of these contacts, one can determine how the spin polarizations of the contacts change in external magnetic fields. Ensuring that the ferromagnetic thin films deposited on large-diameter nanowires retain their favourable magnetic properties poses a substantial technical challenge. Here, the fabrication aspect of creating such structures is examined, and a new processing scheme is introduced for the creation of quasi-suspended ferromagnetic contacts.

Magnetoresistive phenomena can also be investigated using the stray fields of magnets. Patterned ferromagnetic films, often referred to as micro- or nanomagnets, offer a means of creating local magnetic fields and field gradients through their stray field. Many novel concepts in the field of nanoelectronics require the creation and control of sub-micron-scale spatial variations in the magnetic field, attainable with such magnetic structures.

Nanomagnets have been successfully employed in creating the field gradients required to achieve coherent manipulation of a spin-charge qubit [35–38] or singlet-triplet qubit [39]. Moreover, engineering the stray-field profile by modifying the magnet geometry [40] offers a way of electrically manipulating electron spins in a scalable way. The concept of using field gradients for the manipulation of spin qubits is sketched in Fig. 1.1.a).

Semiconducting InAs and InSb nanowires have gained significant attention in recent years, as a solid state system for realizing Majorana fermions [41–45]. Theoretical calculations have suggested the existence of further exotic excitations with fractional charge form, so-called *fractional fermions* [26–28]. A spatially varying magnetic field, created by an array of nanomagnets, has been proposed as a feasible setup for the observation of such non-Abelian quasiparticles [46–48], shown in Fig. 1.1.b).

Cooper pair splitters are another system which nanomagnets could help in reaching their full potential. Devised as an on-chip source of entangled electrons, these devices aim to extract Cooper pairs from the spin-singlet ground state of superconductors, and split its electrons into quantum dots on opposite branches of the device [49] via the process of Crossed Andreev Reflection (CAR) [50, 51]. Such devices have been successfully realized in bottom-up systems, finding correlations in current [30, 52] and charge noise [44]. While many aspects of the underlying physics have been examined [31, 44, 53–56], the proof of entanglement is still lacking. To address this issue, spin correlation measurements are required. However, the superconductor limits the maximum applicable external magnetic field to induce spin splitting on the quantum dots and the requirements imposed on the quality of the spin-polarized detectors for entanglement witnessing are also quite stringent [57–59].

A recent proposal by Branuecker *et al.* suggested a scheme of entanglement detection in a Cooper pair splitter [29] which did not require microwave fields [60–62]. This relied on different spin projection axes on the two quantum dots, achieved by locally different \mathbf{B} magnetic fields. We propose a realization of this scheme using the stray fields of nanomagnet split gates [40], shown in Fig. 1.1.c), where the combined effect of the stray field and external field results in a locally different spin projection axis for QD2 than that of QD1.

Following the proposal, we introduce a new magnetic split gate design for the creation of a local magnetic stray field on a quantum dot. We first investigate the effect of electrostatic gating with normal metals. We present proof-of-principle measurements

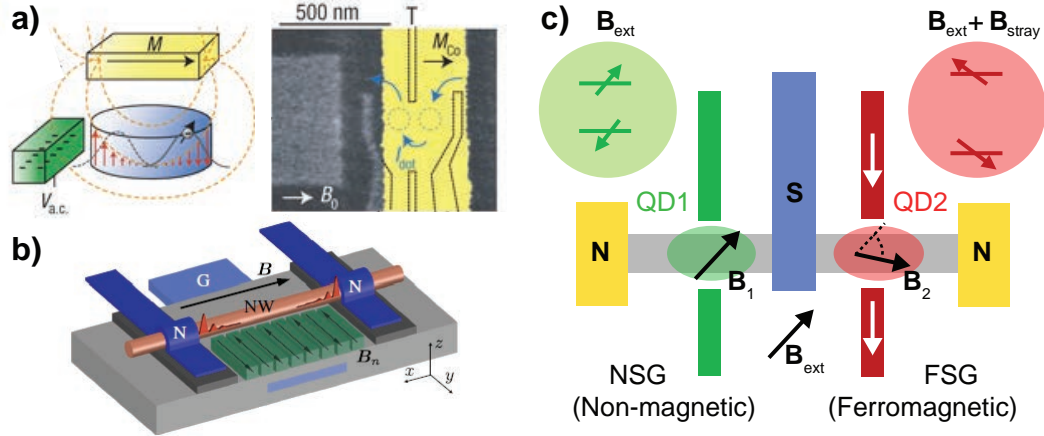


Figure 1.1.: Nanomagnets exploited in nanoelectronics devices | a) Single electron spin resonance setup in a slanted magnetic field created by the stray field of a nanomagnet (from [36]). b) Fractional fermion phase realized via modulated magnetic fields created by an array of ferromagnets (from [46]). c) Entanglement detection scheme in Cooper pair splitters based on local spin projection axes created by a pair of ferromagnets.

on devices with permalloy side gates, finding ~ 50 mT stray fields. We observe a dependence of the magnetoconductance on the quantum dot state and side gate voltages, which we attribute to changes in the coupling energies of the quantum dot. Furthermore, for some resonances, exotic spin-valve signals are found, with relative changes in conductance up to $\sim 50\%$.

Thesis outline

The thesis is organized as follows:

- Chapter 2 summarizes the theoretical background of the physics of the phenomena encountered in later chapters: ferromagnetism and magnetoresistance phenomena, quantum dots in different geometries;
- Chapter 3 gives an overview of the growth and properties of InAs nanowires as a platform for transport experiments;
- Chapter 4 presents the employed fabrication and experimental techniques.

Following the synopsis of the field, the experimental results on the magnetoconductance of InAs quantum dots is presented:

- The effect of confinement on the magnitude and anisotropy of the g factor examined in Chapter 5 – in collaboration with Samuel d’Hollosy [34];
- In Chapter 6 a novel method of creating high-quality ferromagnetic contacts to nanowires is introduced, the magnetic and contact properties of the contacts are examined on as-fabricated devices, and preliminary magnetoresistance measurements are presented;

-
- The electrostatic gating effect of a pair of normal metal side gates is investigated in Chapter 7;
 - In Chapter 8, a new magnetic split-gate design is introduced and characterized, and proof-of-principle magnetoresistance experiments using permalloy nanomagnets are presented and discussed;
 - The findings of the thesis are summarized in Chapter 9, in which we also discuss the possible follow-up experiments.

2 Theoretical Background

In this chapter, the theoretical background is provided for the phenomena encountered in this thesis.

In Sec. 2.1, we systematically address the topic of ferromagnets, which were employed as either contact or gate electrodes in the presented work. The section discusses the origin of ferromagnetism, the energy terms which determine the magnetization, and introduces the most common transport phenomena arising from the use of ferromagnets.

Quantum dots are the basic building block around which all investigated devices are constructed. Sec. 2.2 briefly discusses the basic concept of quantum dots and their characteristic transport properties in both single- and double-dot geometries. The effect of magnetic fields on the quantum dots is also discussed, as it is crucial to gain insight into the physics of spins enclosed in the system to subsequently manipulate them.

2.1. Ferromagnetism

The origin of magnetism in materials is the magnetic moment of electrons, stemming from their orbital motion and the electron spin. The response of a material to an external field can be: para-, dia-, ferro-, and antiferromagnetism, depending on the alignment of the elementary magnetic moments. This response is formulated in the magnetization, a vector field that expresses the density of magnetic dipole moments in the material.

In the case of ferromagnetism, the elementary moments retain alignment, resulting in a non-zero magnetization in the absence of an external field. This is the so-called remanent magnetization, M_r in Fig. 2.1.a). The magnetization is only reversed when an applied magnetic field is sufficiently large to overcome the ferromagnetic ordering. This is referred to as the coercive field, $B_c = \mu_0 H_c$ in Fig. 2.1.a). At high magnetic fields, all magnetic moments are aligned parallel with the field, and the material reaches saturation magnetization, denoted by M_S .

The magnetic field dependence of the magnetization is strongly affected by the magnetization history, revealing a loop in the magnetization curve of the magnet, seen in Fig. 2.1.a). This is referred to as magnetic hysteresis. The width of this loop determines the ability of the material to withstand external magnetic fields, without losing its magnetization. Magnets with low and high coercivity are categorized as *soft* and *hard* magnets, respectively.

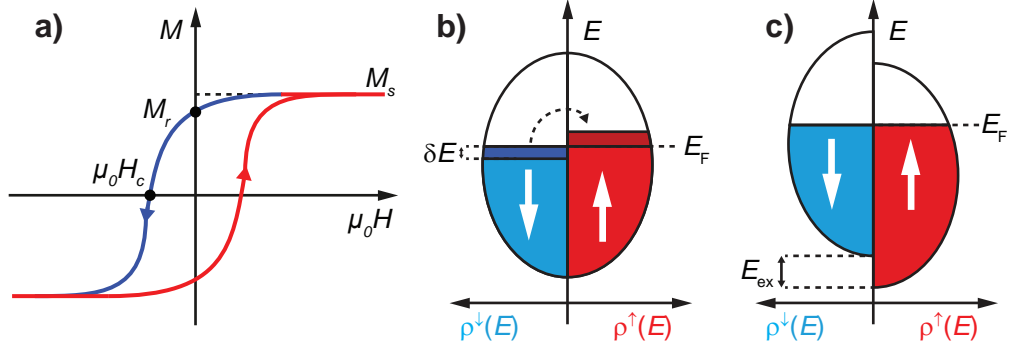


Figure 2.1.: Characteristics of ferromagnetism a) Magnetization curve of a ferromagnet. Red and blue curves denote positive and negative sweep directions. b) Schematic illustration of the density of states for spin-up and spin-down electrons. Spin-flip processes are denoted by the dashed arrow. c) Illustration of exchange-split spin bands, predicted by the Stoner model.

2.1.1. Microscopic origin: Exchange interaction, Stoner model

According to classical physics, it is energetically favourable for magnetic dipoles to align in opposite relative orientations. However, in quantum mechanics, one has to consider the so-called exchange interaction. The exchange interaction is sometimes referred to as Pauli repulsion as it is closely related to the Pauli exclusion principle. The fermionic statistics of electrons requires the wave function to be antisymmetric under the exchange of two particles, which means that the spatial distribution of the electrons will depend on their spin configuration. For magnetic materials, the parallel spin configuration is energetically favourable due to the enhanced Coulomb repulsion for the antiparallel arrangement. The alignment of the spins is only possible if thermal fluctuations do not dominate the exchange interaction: above the so-called "Curie temperature" (T_C), ferromagnetism is destroyed. Whilst direct exchange is the core principle behind ferromagnetism, other interactions can also play a significant role in determining the magnetic ordering of certain systems, such as antiferromagnetic superexchange, antisymmetric exchange (Dzyaloshinskii–Moriya interaction), or indirect exchange of conduction electrons with the magnetic moments of nuclei or localized electrons through the RKKY interaction. Nevertheless, it is sufficient here to consider only the direct exchange interaction.

The picture so far illustrates the magnetic ordering of electrons in an atomic environment and can be applied to models of localized electrons within the bounds of statistical physics. For metallic systems, we turn to the Stoner model for itinerant electrons, and consider bands. This model assumes two separate bands for the spin up and spin down conduction electrons and calculates the energies associated with the creation of spontaneous magnetization from the imbalance of the two spin species. As electrons are transferred from one spin band to the other, the kinetic energy will increase, as seen in Fig. 2.1.b). Concurrently, the potential energy of the magnetic

moments in the generated molecular field decreases. Thus spontaneous magnetization can only be sustained for $E_{\text{tot}} \leq 0$, yielding the Stoner criterion:

$$U\rho(E_F) \geq 1, \quad (2.1)$$

where U is the strength of the exchange interaction and $\rho(E_F)$ is the density of states at the Fermi energy.

Despite the simple nature of the model, it provides a good explanation for why Fe, Co, and Ni, the only elementary metals that exhibit ferromagnetic behaviour. This is due to the fact that in these transition metals, the Fermi energy lies within the narrow $3d$ band, leading to a large density of states.

If the Stoner criterion is fulfilled, the two bands shift with respect to each other, since the chemical potential in the two bands must be equal in thermal equilibrium. This leads to a situation of spin-split bands, where the two bands are separated by the exchange splitting E_{ex} , sketched in Fig. 2.1.c).

Depending on whether one considers the magnetization of the material or the main contribution to the conductivity, the term *majority spin* can denote the spin species for which the total number of spins is superior ($n_{\uparrow} > n_{\downarrow}$) or which has a higher density of states at the Fermi energy ($\rho_{\uparrow}(E_F) > \rho_{\downarrow}(E_F)$). Similarly, the term *spin polarization* may be defined using the absolute number of spins $P = \frac{n_{\uparrow} - n_{\downarrow}}{n_{\uparrow} + n_{\downarrow}}$ or the ones close to the Fermi level $P = \frac{\rho_{\uparrow}(E_F) - \rho_{\downarrow}(E_F)}{\rho_{\uparrow}(E_F) + \rho_{\downarrow}(E_F)}$.

2.1.2. Magnetic anisotropies

The magnetization in the Stoner model is homogeneous over the whole of the material, with no preferred orientation. So we can see that while the microscopic model gives us a tangible explanation for the origin of the phenomenon, it cannot be applied for the description of a bulk magnet of a certain geometry.

For realistic samples one needs to consider the variation of the $\mathbf{M}(\mathbf{r})$, and minimize the total energy of the magnetic structure. For this thesis, we shall restrict ourselves to a brief overview of the most important energy terms and their anisotropies, and the resulting consequences.

Firstly, let us consider the coupling of the magnet and an external field. This is given by the Zeeman energy density [3]:

$$\mathcal{E}_Z = -\mathbf{M}\mathbf{B}, \quad (2.2)$$

which is minimized for the magnetization parallel to the external field, illustrating how a sample can be magnetized in arbitrary directions for sufficiently strong fields.

Now we turn on exchange interaction. We have seen that this interaction aligns spins of adjacent sites parallel. This can be adapted to a continuous vector field as an energy density term that penalizes the variation of the magnetization:

$$\mathcal{E}_{\text{ex}} = A(\nabla\mathbf{M})^2. \quad (2.3)$$

This short-range interaction explains the microscopic magnetic ordering, however, it fails to account for the fact that ferromagnets have stable zero-field configurations, where the magnetization has a preferred orientation. This requires a type of "built-in" magnetic anisotropy. The internal energy density of the such magnets depends on their magnetization direction and is minimal along the so-called *easy axis* of the solid, defined by its crystal structure. Conversely, the term *hard axis* refers to the orientation of the maximal energy.

In the case of *magnetocrystalline anisotropy*, the internal energy of the magnet depends on the crystalline structure of the solid due to crystal-field and spin-orbit effects. This is usually described by the leading term of an expansion for uniaxial anisotropy:

$$\mathcal{E}_{mc} = K_u \sin^2 \theta, \quad (2.4)$$

where θ is the angle between the magnetization and the easy axis. Such an expression has two minima for parallel and antiparallel configurations, and as we shall see for the Stoner–Wohlfahrt model is already sufficient to account for magnetic hysteresis.

Another term one has to consider is the dipolar (or magnetostatic) energy density. This is determined by the energy of the local magnetization in the the dipolar field generated by the sample itself:

$$\mathcal{E}_d = -\mathbf{M}(\mathbf{r})\mathbf{B}_d(\mathbf{r}) \quad (2.5)$$

Due to the implicit and non-local nature of \mathbf{B}_d , the treatment of this term can pose difficulties and can only be accounted for by costly numerical simulations. Unfortunately, the devil lies in the details, and the importance of this term cannot be underestimated for samples of finite dimensions, due to its determining role in non-uniform magnetization configurations and exotic domain wall configurations.

The dipolar field generated by the magnet is usually separated into the field inside the body of the source and outside of it. We refer to these as the *demagnetizing* and stray fields, respectively. The effect of the former can be briefly summarized as a tendency of the magnet to reduce surface magnetic charges, i.e., align the magnetization parallel to the body edges. This is highly important for soft magnetic materials, such as Permalloy, as the magnetization of the sample can be engineered in a desired direction by simply choosing the appropriate geometry. Hence, it is referred to as *shape anisotropy*. A good example is an extended thin film which keeps the magnetization vector in-plane or an elongated strip where it will tend to align with the long axis. In turn, the stray field is the observable field of the magnet and is of crucial importance in some of our experiments, in which we exploit them to generate local magnetic fields.

It should be noted that this is not an exhaustive list of the possible energy terms, and other external influences can also significantly affect the sample magnetization, e.g. strain through inverse magnetostriction.

The ground state of the ferromagnet is determined by many competing interactions. Considering the built-in anisotropy, the magnetostatic energy of the stray field, and the exchange term, some situations will favor the formation of clusters with short-range magnetic ordering, called magnetic domains. These clusters are separated by

narrow boundaries, so-called *domain walls*, across which the magnetization is changed smoothly but rapidly, sketched in Figs. 2.2.e-f).

To demonstrate different domain structures, we consider a strip of a ferromagnetic material. If the exchange and anisotropy terms dominate, a single domain is formed as shown in Fig. 2.2.a). If contribution of the generated stray field becomes more significant (e.g. by increasing the dimensions of the structure), the ferromagnet forms an array of domains with opposite magnetization rather than a single-domain structure (Figs. 2.2.b-c). In this situation, the reduction of the dipolar energy outweighs the energy cost of domain wall formation. If the magnetocrystalline anisotropy is weak, the stray fields can also be further reduced by the formation of so-called closure domains, which exhibit perpendicular magnetization at the ends of the sample, as shown in Fig. 2.2.d).

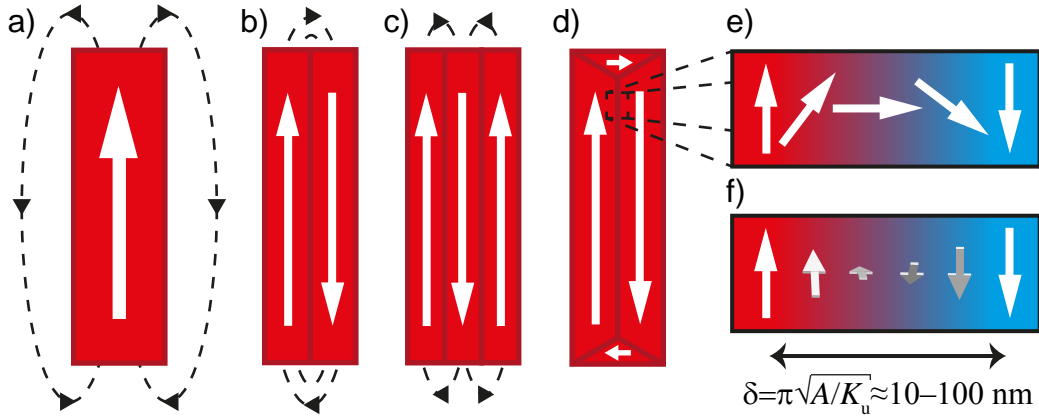


Figure 2.2.: Formation of domain structures. a-d) Single to multi-domain patterns. d) Soft magnets allow the formation of closure domains which further reduce the stray fields of the structure. e-f) Néel- and Bloch-type domain walls.

2.1.3. Stoner–Wohlfahrt model

The treatment of a ferromagnet becomes significantly easier once we simplify our system to a single-domain structure, as most aforementioned energy terms can be neglected. Stoner and Wohlfahrt introduced a model [63] to calculate the magnetization curve of an ellipsoid with homogeneous \mathbf{M} for magnetic fields of arbitrary orientation. Only two energy terms were considered, a uniaxial anisotropy term stemming from magnetocrystalline or shape anisotropy, and the Zeeman energy of the magnet in the external field. This gives

$$\mathcal{E}_{\text{SW}}(B) = K_u \sin^2 \theta - \mathbf{M}\mathbf{B} = K_u \sin^2 \theta - M_S B \cos(\theta - \alpha), \quad (2.6)$$

where θ and α are the respective angles between \mathbf{M} and \mathbf{B} , and \mathbf{M} and the easy axis. The magnetization is restricted to the plane containing the magnetic field direction and the easy axis, which allows us to use the defined angles.

By minimizing this energy density with respect to θ , one obtains the orientation of \mathbf{M} . For low enough fields, this expression yields two solutions, which corresponds to magnetic hysteresis. Consequently, as the magnetic field is swept, the magnetization exhibits a sudden sharp reversal as only one solution becomes sustainable.

Considering the special case of $\alpha = 0^\circ$ (in Fig. 2.3.b), the rotation of the magnetization is energetically unfavourable. Hence, upon reaching the coercive field of

$$H_c = \frac{2K_u}{\mu_0 M_S}, \quad (2.7)$$

the magnetization is reversed. For $\alpha = 90^\circ$, no sudden reversal or hysteresis is observed, as the field slowly rotates the magnetization towards the hard axis.

2.1.4. Magnetoresistance effects

The magnetic characteristics of ferromagnets make them an obvious tool to investigate spin physics in transport experiments. The spin-polarized nature of the contacts allows preferential injection and detection for one spin species, which can thus be discerned. This, in turn, means that \mathbf{M} and \mathbf{B} have an impact on the resistance. Here, the signatures and consequences of the most common magnetoresistance effects are examined.

Anisotropic magnetoresistance (AMR)

First, the effect of the magnetic field on the resistance of a ferromagnet is discussed. It was already observed in the 19th century, that magnetic materials exhibit different electrical resistivity as the angle between the electrical current and sample magnetization is changed. This is referred to as *anisotropic magnetoresistance (AMR)*.

The underlying mechanism of AMR stems from the spin-orbit interaction, which allows a larger scattering probability between the s and d bands when the \mathbf{k} wave vector of the electrons is parallel to the magnetization [64]. The resistivity of the material can thus be described as:

$$\rho(\varphi) = \rho_\perp + (\rho_\parallel - \rho_\perp) \cos^2 \varphi, \quad (2.8)$$

where φ is the relative angle between \mathbf{k} and \mathbf{M} and ρ_\parallel (ρ_\perp) is the resistance for the parallel (perpendicular) arrangement.

The resistivity of ferromagnets is typically described in Mott's two-current model, where the currents carried by the two spin species are separated in two parallel arms. The majority of the current is carried by s electrons due to their small effective mass, while flat d electron bands contribute minimally. However, the d electrons have a significant contribution to the resistivity of the sample where $s-d$ scattering processes are dominant. Hence, the d electrons play a crucial role in the scattering events. The origin of the anisotropy lies in the spin-orbit interaction which allows spin-flip scatterings between s and d bands, as the spin bands are hybridized. The selection rules for the d orbitals involved are determined by the relative orientation of the current and magnetization direction [64].

In a heuristic picture, one can consider the d orbitals to be reorientated in a plane perpendicular to \mathbf{M} , leading to the scattering cross-section to be maximal for $\mathbf{k} \parallel \mathbf{M}$ and minimal for $\mathbf{k} \perp \mathbf{M}$. While this hand-waving explanation is easy to visualize and seems to apply for most cases where $\rho_{\perp} < \rho_{\parallel}$, a more precise description requires thorough treatment of the scattering matrix elements and the type of spin-orbit interaction. In case of the Dresselhaus interaction [65], the sign of anisotropy can be reversed for different current directions [64].

The direction of the magnetization vector can be affected by an external magnetic field. As \mathbf{B} is increased, the \mathbf{M} vector first tilts toward and then eventually aligns with \mathbf{B} . As the direction of the current is unchanged, the effect of the magnetic field on the resistivity can be obtained if we consider the induced change in φ . A qualitative $\varphi(B)$ dependence can be obtained by minimizing the Stoner–Wohlfahrt energy density at different fields. The sample resistance can then be calculated by inserting the resulting $\varphi(B)$ into Eq. (2.8). Typical AMR curves are plotted in Fig. 2.3.

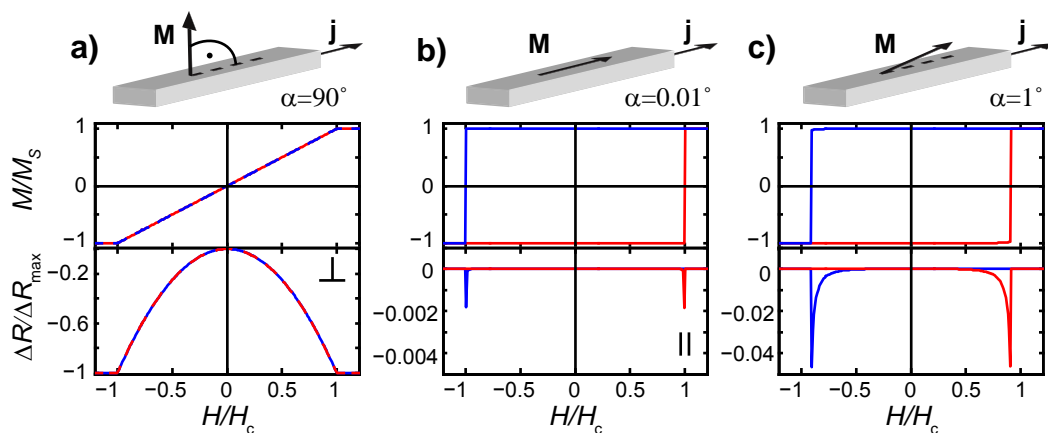


Figure 2.3.: Illustration of the anisotropic magnetoresistance (AMR). a) Magnetic field dependence for fields perpendicular to the long axis of the strip. b-c) Magnetic field dependence for fields nearly parallel to the long axis of the strip for $\alpha = 0.01^\circ$ and $\alpha = 1^\circ$, respectively. Red and blue curves denote up and down sweeps, respectively.

In Fig. 2.3.a), the AMR typical for fields perpendicular to the current is shown. In this case, the magnetization slowly rotates towards the hard axis, eventually lining up and reaching saturation. The resistance will thus reduce and follow a parabolic curve, the width of which is governed by the strength of the magnetic anisotropy. In real samples, demagnetizing fields leads to a more asymptotic convergence to the hard axis.

For fields parallel to the current, no resistance change is predicted as the magnetization is simply expected to suddenly reverse as the H_c coercive field is reached. However, already a slight misalignment causes the magnetization to briefly rotate towards the hard axis before inverting its sign. This leads to a characteristic resistance line shape, exhibiting small dips as magnetization reversal is approached, as shown in Figs. 2.3.b-c).

Although this single domain model and empirical resistance formula are a very simplistic treatment, they provide a good qualitative prediction for the behaviour of our magnetic electrodes. This also allows us to use AMR data to characterise individual strips by determining the coercive fields from the signature of magnetization reversal in their resistance. This is in sharp contrast to standard vibrating sample magnetometry (VSM) where such measurements require $\sim 10^4$ strips.

Spin valves, tunnelling magnetoresistance (TMR)

Spin valve structures have been at the forefront of industrial applications of spintronics for the last 30 years. Such structures have been applied in data storage solutions with great success, allowing significant improvements in capacity as well as read/write speeds. Spin valves structures can be implemented in a variety geometries and using different materials, with the basic design concept being the coupling of a non-magnetic material to two ferromagnetic contacts is the same. In Fig. 2.4.a), we show the sketch of a lateral spin valve, the most common geometry in the case of nanostructures. The two ferromagnetic electrodes possess significantly different coercive fields, and so an antiparallel orientation of the magnets can be sustained, as shown in Fig. 2.4.a). The parallel and antiparallel arrangements produce different resistances, yielding a typical signal which is characterized by the magnetoresistance:

$$\text{MR} = \frac{R_{\text{AP}} - R_{\text{P}}}{R_{\text{P}}} = \frac{G_{\text{P}} - G_{\text{AP}}}{G_{\text{AP}}}, \quad (2.9)$$

where $R_{\text{AP/P}}$ is the resistance and G_{AP} is the conductance of antiparallel and parallel orientations, respectively.

The change in resistance can be achieved exploiting different phenomena. For most commercial products such structures rely on the phenomenon of *giant magnetoresistance (GMR)*, which arises in structures where two ferromagnets are connected by a conductive material [4, 5].

In nanostructures, we use a seemingly similar effect, which can be achieved in the case of non-magnetic tunnel barriers. These tunnel junctions also exhibit different resistances for parallel and antiparallel electrode magnetizations. Accordingly, this phenomenon is referred to as *tunnelling magnetoresistance (TMR)*.

In the case of TMR, the resistance of the structure is determined by the tunnelling probabilities of the two spin species. These rates can be calculated using the Jullière model [66] from the density of states at the Fermi energy where the tunnelling process takes place. The conductance is given as a sum of two independent spin channels as $G = \frac{e^2}{h}(T^{\uparrow} + T^{\downarrow})$, with transmissions

$$T_{\text{AP}}^{\uparrow/\downarrow} = \rho_{\text{AP},1}^{\uparrow/\downarrow}(E_{\text{F}})\rho_{\text{AP},2}^{\uparrow/\downarrow}(E_{\text{F}}), \quad (2.10)$$

$$T_{\text{P}}^{\uparrow/\downarrow} = \rho_{\text{P},1}^{\uparrow/\downarrow}(E_{\text{F}})\rho_{\text{P},2}^{\uparrow/\downarrow}(E_{\text{F}}) \quad (2.11)$$

where $\rho^{\uparrow/\downarrow}(E_{\text{F}})$ is the density of states at the Fermi energy for spin-up and spin-down electrons, and subscripts AP and P refer to the antiparallel and parallel orientations of the contacts. In this model, spin-flip processes are neglected.

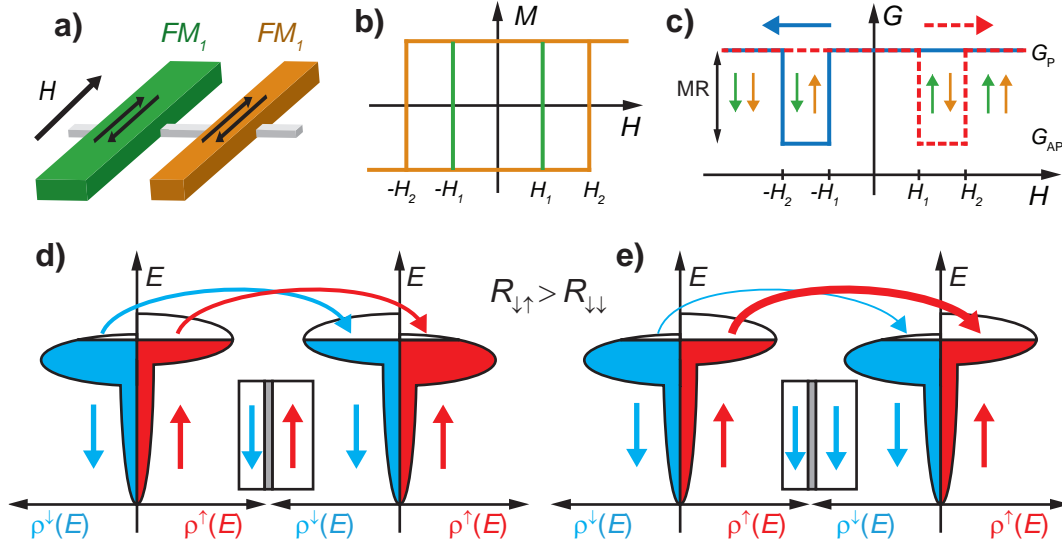


Figure 2.4.: Illustration of spin valves and tunnel magnetoresistance (TMR) | a) Schematic illustration of a lateral spin valve. b) Ideal magnetization curves of the ferromagnetic electrodes of a spin valve. c) Illustration of the magnetoresistance of a spin valve. d-e) Density of states for the two spin bands of the two ferromagnetic contacts in antiparallel and parallel arrangement, respectively. Note the different tunnelling probabilities illustrated by the arrows.

As seen in Fig. 2.4.d-e), the density of states can be significantly different for the two configurations of the contacts. The tunnel magnetoresistance can be formulated as a function of the spin polarizations ($P_{1,2}$):

$$\text{TMR} = \frac{G_P - G_{AP}}{G_{AP}} = \frac{2P_1P_2}{1 - P_1P_2}. \quad (2.12)$$

Magnetoresistances of several hundred percent have been achieved in such structures [67–69]. However, for mesoscopic spin valves, TMR values do not exceed 10% [15–17].

2.2. Quantum dots

Quantum dots are one of the cornerstones of mesoscopic physics, in which a well-controlled number of charge carriers can be confined. These quasi-zero-dimensional structures are small enough to resolve the quantized energy spectrum of the confined electrons, and are thus regarded as artificial atoms.

Quantum dots have been realized in large variety of solid state systems and by many different means, however, in this section we shall restrict ourselves to focusing on the electron transport properties of quantum dots defined in bottom-up nanostructures.

2.2.1. Basics of quantum dots

Low-dimensional structures like quantum dots behave as nanoscale capacitors with small capacitances (few aF). This leads to a large electrostatic energy penalty for the addition of one electron, referred to as the *charging energy* and given by $E_C = \frac{e^2}{C}$. The number of electrons on the quantum dot can thus be changed on a single electron level. Similarly, the *level spacing* in the energy spectrum becomes increasingly pronounced as the size is reduced, which can be approximated as $\delta E \propto \frac{1}{L^2}$ ¹, however, it is strongly dependent on the dot geometry. At low temperatures, the energy cost of adding one electron to the quantum dot surpasses the energy of thermal fluctuations, thus one can precisely control the number of electrons confined to the system.

Owing to their well-controlled nature, quantum dots are an ideal test bed for the study of electronic quantum phenomena, which can be investigated using electron transport spectroscopy. This requires weakly coupled quantum dots so that electrons can tunnel on and off the quantum dot, while keeping it isolated from the environment.

Constant interaction model

A schematic illustration of a quantum dot circuit is shown in Fig. 2.5.). The quantum dot (QD) is tunnel-coupled to the source (S) and drain (D) electrodes, with corresponding Γ coupling strengths. The dot is capacitively coupled to both the leads and all (G,G',G",...) gate electrodes, quantified by their capacitances to the structure. The electronic states of a quantum dots are usually described within the simple framework of the constant interaction model [13, 14]. This treatment assumes the E_n single-particle energy spectrum of the quantum dot to be unaffected by the charge state, i.e., the electron filling of the dot. Furthermore, all Coulomb interactions of an electron with all other electrons (on and off the quantum dot) are considered within a constant C_Σ , which is a sum of all capacitively coupled electrodes $C_\Sigma = C_S + C_D + C_G + C_{G'} + \dots$. The total energy of the N -electron quantum dot is given by

$$U(N) = \frac{1}{C_\Sigma} \left(-|e|(N - N_0) - \sum_i C_i V_i \right)^2 + \sum_{n=1}^N E_n \quad (2.13)$$

where $N = N_0$ for $V_i = 0$ for all electrodes. The first term is the electrostatic energy of the dot, where the total charge $Q_{tot} = -|e|(N - N_0) - \sum_i C_i V_i$ is a sum of the N electrons, and the charge induced by all electrodes.

For zero-bias transport properties, one should only care about the ground state transitions, i.e., the conditions of adding electrons. To treat this with ease, one can thus construct a "ladder" of states, considering the electrochemical potential of the dot holding N electrons. This is defined as $\mu_N = U(N) - U(N - 1)$, i.e., the energy for adding the N^{th} electron to the dot, and is given as

$$\mu_N = E_N + \frac{e^2}{C_\Sigma} \left(N - N_0 - \frac{1}{2} \right) - \frac{|e|}{C_\Sigma} \sum_i C_i V_i. \quad (2.14)$$

¹This is assuming electrons of quadratic dispersion $E \propto k^2$

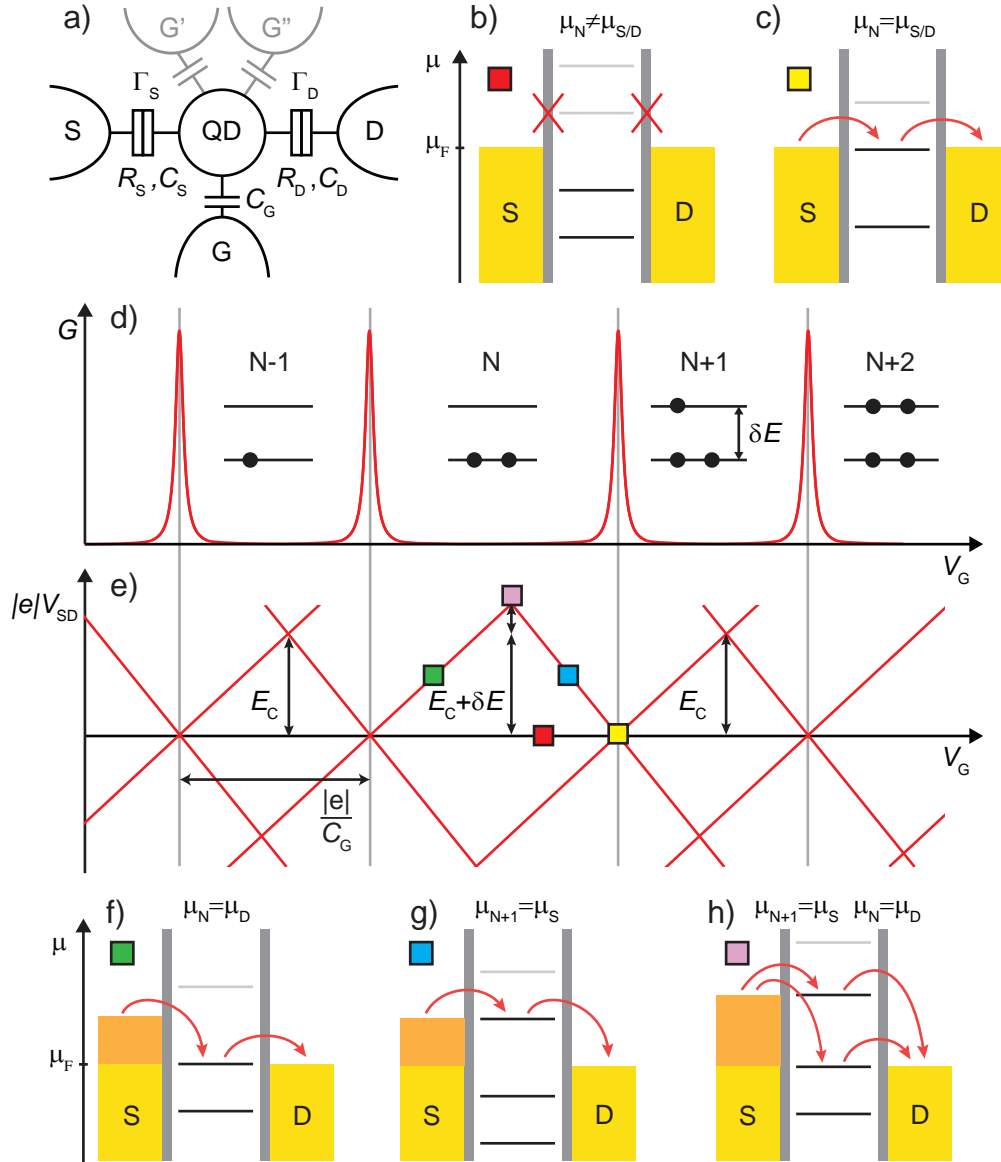


Figure 2.5.: Coulomb blockade and Coulomb diamonds. a) Schematic picture of a single quantum dot device, tunnel-coupled to the leads and capacitively coupled to multiple gates. b) Illustration of Coulomb blockade, current is blocked when no levels are aligned with the leads. c) Illustration of resonant tunnelling, arising when a level is aligned with the leads. d) Gate voltage dependence of zero-bias conductance in Coulomb blockade regime. Conductance peaks arise when resonant tunnelling is allowed. The filling of the energy levels and the level spacing are shown in the inset. e) Illustration of bias and gate voltage dependence of conductance in Coulomb blockade regime. Red lines refer to conductance peaks due to ground state transitions, excited state lines are omitted. f-g) Illustration of finite-bias transport process, when quantum dot level is aligned with the drain and source, respectively. These refer to the lines with positive and negative slopes in e), respectively. h) Illustration of finite bias transport process when the bias is sufficiently large to span two levels. Here, both source and drain electrodes are aligned with separate levels, corresponding to the apex of the diamond in e).

With the gate electrode, one can modify the electrostatic potential of the QD, and thus its chemical potential as well. By tuning V_G , one can therefore modify the ground state of the quantum dot, as filling the QD with more electrons becomes energetically favourable. The change in the chemical potential is connected to the change in gate voltage through the so-called *lever arm*, given by

$$\alpha_G = \frac{\Delta\mu}{|e|\Delta V_G} = \frac{C_G}{C_\Sigma}. \quad (2.15)$$

Coulomb Blockade and Single Electron Tunneling

The main signature of QD behaviour in transport experiments is the so-called Coulomb blockade. This refers to the phenomenon that due to the weak coupling to the leads and the large charging energy, current can only flow when the electrochemical potential of a QD level is aligned with that of the leads. In blockade, sketched in Fig. 2.5.b), the number of electrons on the quantum dot cannot fluctuate at zero bias, thus electron transport is blocked and the electron filling remains constant.

As we tune the electrochemical potential of the quantum dot with a gate electrode, the ladder of states is shifted with respect to the Fermi energy of the leads. In case one of the levels ($\mu(N)$) is aligned with the leads ($\mu_{S/D}$), sketched in Fig.2.5.c), the ground state of the quantum dot holding N and $N + 1$ electron become degenerate allowing electrons tunnelling off and on to the QD. Thus a resonant channel for current flow is created which is manifested as a peak in the conductance of the device, whenever a level is aligned with the leads (Fig.2.5.d).

For electrons on a degenerate level, the level spacing is zero ($\delta E = 0$), thus the addition of an extra electron to this level increases the total energy of the QD by the $\frac{e^2}{C_\Sigma}$ charging energy. Such a situation is shown in Fig. 2.5.d) for the QD holding $N - 1$ and $N + 1$ electrons. This leads to a peak spacing of $\Delta V = \frac{e}{C_G}$, as shown in Fig. 2.5.d-e)

In case a degenerate level is filled, for the addition of the next electron, the level spacing also needs to be overcome, as seen for the $N \rightarrow N + 1$ transition in Fig. 2.5.d) leading to a larger distance between the conductance peaks. In InAs QDs, a 2-fold pattern of the conductance peaks is expected due to spin degeneracy, as seen in Fig. 2.5.d-e).

Resonance line shape

Now we turn to the shape of the conductance resonances. Our system can be simplified as a double barrier system, defined by the $\Gamma_{S/D}$ tunnel couplings to the source and drain electrode, as in Fig. 2.5.a). The conductance peak is then approximated by a Lorentzian curve [70]:

$$G(V_i) = \frac{2e^2}{h} \frac{\Gamma_S \Gamma_D}{\Gamma_S + \Gamma_D} \frac{\Gamma}{(e\alpha_i V_i)^2 + (\Gamma/2)^2}, \quad (2.16)$$

where $\Gamma = \Gamma_S + \Gamma_D$ is the effective width of the resonance.

This picture applies for situations where the thermal broadening of the Fermi distribution in the leads is negligible compared to the tunnel couplings ($k_B T \ll h\Gamma$). By better decoupling the QD from the environment or by increasing the temperature, the reverse situation of $k_B T \gtrsim h\Gamma$ can be attained, for which the resonance line shape [71] is given by:

$$G(V_i) = \frac{e^2}{h} \frac{1}{4k_B T} \frac{\Gamma_S \Gamma_D}{\Gamma_S + \Gamma_D} \cosh^{-2} \left(\frac{e\alpha V_i}{2k_B T} \right). \quad (2.17)$$

The smearing of the peak thus results in an $1/T$ reduction of the maximum peak conductance and a linear broadening of its width: $e\alpha \Delta V_i^{FWHM} \approx 3.5k_B T$.

Analysis of the peak shapes thus allows one to extract absolute values for $\Gamma_{S/D}$, however, these values cannot be assigned to a specific electrode.

Coulomb diamonds

Mapping out the conductance of the quantum dot device as a function of the gate and bias voltages reveals a characteristic pattern in Fig. 2.5.d), known as *Coulomb diamonds*. If a dc bias voltage is applied to between the source and drain electrodes, charge transport is possible whenever a level is within the bias window. Consequently, a peak is observed in the differential conductance when a level is aligned with either of the electrodes. Both leads also couple capacitively to the QD, meaning that as the bias voltage is applied it also affects the chemical potential (see the additional terms in the sum in Eq. (2.14)). The gating of the leads is compensated for with the gate electrode in order to maintain a constant μ . The onset of charge transport thus occurs along lines with a positive (negative) slope, corresponding to a dot level coming into alignment with the source (drain) electrode, as seen in Fig. 2.5.e-f), respectively. At the apexes of the diamonds in Fig. 2.5.d), both source and drain leads are aligned with a dot level (sketched in Fig. 2.5.g). In this case, the bias is sufficiently large to overcome the charging energy (and the level spacing), i.e., $|e|V_{SD} = E_C(+\delta E) = E_{\text{add}}$. Thus the size of the diamonds, just like the spacing of the peaks can be used to determine the addition energy, E_{add} .

The capacitances of the source electrodes and gate lever arm, as defined in Eq. (2.15), can be determined from the slopes of the Coulomb diamonds:

$$\alpha_G = \frac{C_G}{C_\Sigma} = \frac{\beta^+ |\beta^-|}{\beta^+ + |\beta^-|}, \quad (2.18)$$

where $\beta^{+/-}$ are the slopes of edges of the Coulomb diamonds with the corresponding sign. These slopes can also be used to calculate the capacitances of the leads [72]. In the usual case of a grounded drain electrode, these slopes correspond to

$$\beta^- = -\frac{C_G}{C_S} \quad \text{and} \quad \beta^+ = \frac{C_G}{C_\Sigma - C_S}. \quad (2.19)$$

2.2.2. The Kondo effect

Until now, we have considered quantum dots that were weakly coupled to the leads. As the coupling is increased, higher-order co-tunnelling processes become more prominent. A striking example is the Kondo effect, which refers to the appearance of a conductance ridge in the in the blockaded region of the Coulomb diamonds at odd occupancy [73, 74], as illustrated in Fig. 2.6.b). This arises when an unpaired spin on the dot hybridizes with the Fermi sea in the leads, forming a global singlet state. Thus an additional zero-bias conductance channel is created where electrons are transferred through elastic spin-flip co-tunnelling. This is usually represented as an additional narrow peak in the density of states of the QD, pinned to the Fermi level [73], as sketched in in Fig. 2.6.a). When a bias voltage is applied to the leads, their electrochemical potentials no longer remain aligned and conductance drops as the elastic electron transfer process cannot take place.

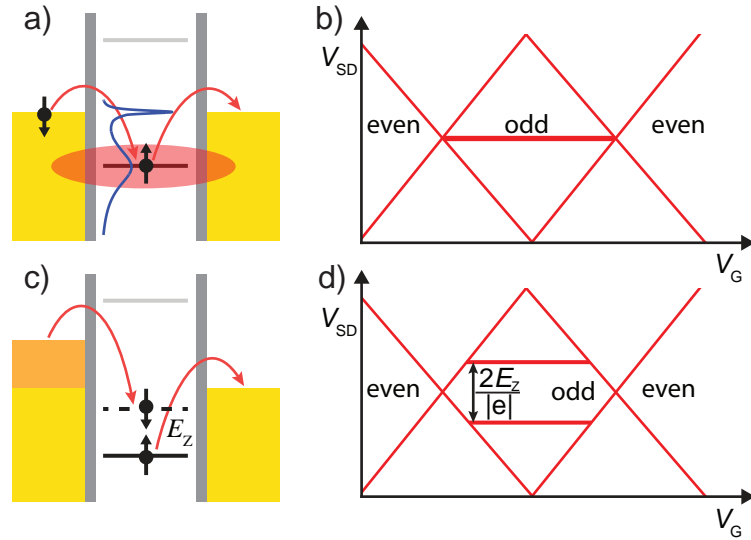


Figure 2.6.: The Kondo effect in a quantum dot. a) Schematic of the elastic spin-flip process stemming from the Kondo effect. The enhanced co-tunnelling leads to a narrow peak in DOS at E_F . b) The elastic process results in a zero-bias feature in Coulomb blockade for odd QD occupancy. c) Schematic of the inelastic Kondo process in a magnetic field. The applied bias is equal to the Zeeman splitting of the spin-split levels. d) The zero-bias feature is split into two branches in a magnetic field. The conductance features appear at $V_{SD} = \pm E_Z/e$

The width of this resonance is determined by the so-called Kondo temperature which determines the onset of Kondo correlations and below which the zero-bias conductance channel can develop. This temperature depends on the strength of the QD coupling (Γ), the charging energy (E_C), and the relative energy of the singly-filled level relative to E_F (ϵ_l) as follows [74]:

$$k_B T_K = \frac{1}{2} \sqrt{\Gamma E_C} \exp\left(\frac{\pi \epsilon_l (E_C + \epsilon_l)}{\Gamma E_C}\right) \quad (2.20)$$

As a magnetic field is applied, the spin degeneracy of the odd-filled level is lifted, as in in Fig. 2.6.c). Therefore, the spin-flip co-tunnelling process can only occur if a sufficient bias is applied to overcome the the Zeeman splitting of the levels with the inelastic process leaving the QD in the Zeeman-split excited state. Hence, as illustrated in Fig. 2.6.d), the Kondo ridge is consequently also split into two ridges [21, 73–75], occurring at

$$eV_{\text{sd}} = \pm E_Z = \pm g^* \mu_B B. \quad (2.21)$$

As one follows the evolution of the Kondo feature, the zero-bias peak is split into two branches that separate linearly as the field is increased. For higher fields, the contribution of excited states becomes increasingly prominent and the two conductance peaks slowly evolve into step-like features, eventually merging with the flat inelastic co-tunnelling conductance steps.

One should keep in mind that while the presented single-electron picture provides a tangible way of tackling the problem, the Kondo ground state is an extended many-body state with complicated electron-electron interactions. So in many cases one should exercise caution in applying this hand-waving interpretation.

Interestingly, the Kondo effect term was coined for the phenomenon of logarithmic resistance increase in metals at low temperatures. While this manifestation of the effect is drastically different to that encountered in mesoscopic systems, the underlying physics is identical, as it is due to the creation of an extended cloud of electron around localized magnetic impurities in order to screen the magnetic moment of the impurity.

2.2.3. Quantum dot states in magnetic field

Electrons in a quantum dot occupy doubly degenerate levels. The two-fold spin degeneracy of these levels is lifted by applying an external magnetic field. The energy of the parallel and antiparallel spin configurations is thus shifted linearly in opposite directions as the field is increased, due to the Zeeman effect [3]. Furthermore, the energy of all levels shows a state-independent parabolic dependence, referred to as the diamagnetic shift [70]. The energy of the levels can thus be written as

$$E_{N,s_z}(B) = g_N^* \mu_B B s_z + \gamma B^2, \quad (2.22)$$

where $s_z = \pm 1/2$ denotes the spin-up and spin-down states, and γ is the experimentally determined constant accounting for the diamagnetism of the QD. This is not an exhaustive description as the only orbital effect accounted for by this expression is the diamagnetic response of the quantum dot, nevertheless it explains the most common features present in a spectrum.

As the electron is treated as a non-interacting particle, all the interactions are actually accounted for within the effective g factor (g^*). The g^* of band electrons of semiconductors can be easily treated in the perturbation theory approach of the 8-band $\mathbf{k} \cdot \mathbf{p}$ approximation. Following through such calculations [76], one arrives at the expression:

$$g^* = 2 - \frac{2E_P \Delta}{3E_g(E_g + \Delta)}, \quad (2.23)$$

where E_g is the semiconducting gap, Δ is the energy difference between the valence band and the spin-orbit split-off band, and E_p is the energy equivalent of the principal interband momentum matrix element.

Substituting the appropriate parameters reveals that for bulk InAs, the effective g factor of $g_{\text{InAs}}^* = -14.7$ is considerably different from the free electron value of $g_e = +2.0023$. InAs nanostructures, like their bulk counterparts, possess large effective g factors [21, 22, 32, 34], although as the dimensions are reduced, the effect of confinement is increasingly prominent and can significantly change the value of g^* [77], bringing it closer to the free electron value. This is due to a combination of the energy gap being rescaled by the confinement potential, and more significantly, the QD not being able to support the excited states. This phenomenon is sometimes referred to as quenching of the orbital momentum [78, 79], an allusion to the quenching of L in solids due to the crystal field.

In transport spectroscopy, one measures the addition spectrum of the quantum dot, the levels in Eq. (2.22) are further separated by the charging energy. Thus by measuring the conductance as a function of gate voltage and magnetic field, the Coulomb resonances will exhibit position shifts following Eq. (2.22), which determines the changes of the QD chemical potential, as seen in Eq. (2.14). If the Zeeman energy $\Delta E_Z(B)$ exceeds the level spacing $\delta E(B)$, a ground state transition takes place and thus the N electron state will evolve following the lower energy state in the $E_N(B)$ spectrum. This also means that for low level spacings the Zeeman shifts are often obscured, as ground state transitions may occur at lower B fields.

2.2.4. Magnetotunnelling

The conductance of quantum dots can be significantly affected by applying an external magnetic field. As the electrons injected to the quantum dot tunnel through the barrier, they attain a transversal momentum as they are deflected by the Lorentz force stemming from the magnetic field. This momentum is given by

$$k_t = \frac{elB}{\hbar}, \quad (2.24)$$

where l is the effective tunnelling distance, given by the width of the barrier. This effect is referred to as *magnetotunnelling*.

The tunnelling matrix element M can then be calculated using the \mathbf{k} -space wave functions of the quantum dot (ϕ_{QD}), and the emitter (ϕ_e), where the deflection due to the Lorentz force is taken into account. The matrix element is thus given as

$$M(\mathbf{k}_t) = \int \phi_e(\mathbf{k} - \mathbf{k}_t) \phi_{QD}(\mathbf{k}) d\mathbf{k}, \quad (2.25)$$

and the tunnel current can be expressed as $I \propto |M(\mathbf{k}_t)|^2$. By approximating the emitter wave function with a delta function, the magnetoconductance will be determined by the Fourier transform of the QD wave function.

$$G(\mathbf{B}) \propto |\phi_{QD}(\mathbf{k}_t)|^2 \quad (2.26)$$

Such measurements have been employed to map out the wave function in an ensemble of self-assembled quantum dots [80, 81]. This shows how the transversal distribution of the wave function plays an important role in determining the quantum dot magneto-conductance. This can ultimately explain conductance variations in magnetic fields, which have been observed in our experiments.

2.2.5. Magneto-Coulomb Effect

Quantum dots are extremely sensitive to the electrostatics of their surroundings and can be affected by minute changes in the electrochemical potential of ferromagnets. The effective gating action on a quantum dot induced by applying an external magnetic field to a ferromagnet in close proximity is referred to as the magneto-Coulomb effect [82], and is well documented for quantum-dot based spin valves [82–84].

In a metal, an external magnetic field shifts the electron energies of the two spin species by a $\pm \frac{1}{2}g_{FM}\mu_B B$ Zeeman term of opposite sign. As we are dealing with a ferromagnet, the electron filling of the two spin bands differ, and so the corresponding densities of states $\rho_{\uparrow/\downarrow}(E_F)$ are also different, as seen in Fig. 2.7.a). The ferromagnet is connected to a normal metal, a charge reservoir. To preserve the total charge, the chemical potential of the ferromagnet will be shifted by:

$$\Delta\mu = -\frac{1}{2}Pg_{FM}\mu_B B, \quad (2.27)$$

where g_{FM} is the g factor, μ_B is the Bohr magneton, and $P = \frac{\rho_{\uparrow} - \rho_{\downarrow}}{\rho_{\uparrow} + \rho_{\downarrow}}$ is the spin polarization of the ferromagnet.

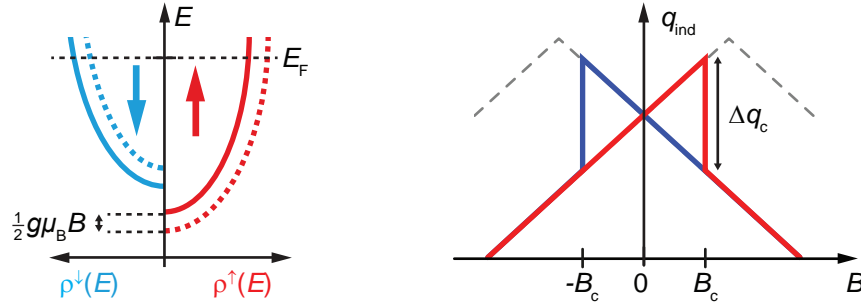


Figure 2.7.: The magneto-Coulomb effect a) Sketch of the spin bands in a ferromagnet. The magnetic field shifts the band energies in opposite directions, as shown by the dashed curves. b) Illustration of the characteristic sawtooth-like magnetic field dependence of the charge induced on the QD. Red and blue lines refer to positive and negative sweep directions.

The change in chemical potential effectively acts as a gate voltage applied to the quantum dot, inducing an additional charge on the island:

$$\Delta q_{\text{ind}}(B) = \frac{C_{FM}}{2e} P g_{FM} \mu_B B, \quad (2.28)$$

where C_{FM} is the capacitance of the ferromagnet to the quantum dot. We can thus see that the magneto-Coulomb effect would lead to a linear shift of the quantum dot spectrum as the magnetic field is changed. Let us consider the effect of applying antiparallel magnetic fields, which can lead to the reversal of the magnetization of the ferromagnet. In the simplest case, this can be treated as an instantaneous change from P to $-P$ as the magnetic field is swept through the B_c coercive field of the strip. This then leads to a sudden change in the induced charge,

$$\Delta q_c = \frac{C_{FM}}{e} P g_{FM} \mu_B B_c, \quad (2.29)$$

which in turn means the field dependence is discontinuous as the coercive field is reached, leading to a characteristic, sawtooth-like profile in the induced charge, as seen in Fig. 2.7.b). Accordingly, the positions of the resonances in the addition spectrum of the quantum dot are also shifted in a similar manner.

2.2.6. Double quantum dots

So far, only single quantum dot systems have been considered. By coupling multiple quantum dots, one can create systems, which can be considered as artificial molecules, following the analogy of artificial atoms. In the following, we discuss double quantum dots connected in series, as well as the effect of interaction between the dots, and how it is manifested in the transport properties.

The constant interaction model can also be used to successfully describe weakly interacting double (multiple) quantum dot systems. For this description, one has to consider the capacitances of all elements to all quantum dots, as well as the interdot capacitive couplings. A model system is shown in Fig. 2.8.a), where the coupling of two quantum dots is given by Γ_t . In such small systems, capacitive crosstalk between gates is hard to avoid, meaning that neither gate acts independently of the other. Both gates tune both dots to different extents. We find resonances with different slopes in the charge stability diagram of a double quantum dot as a function of the two gate voltages, as shown in Fig. 2.8.b). The slopes of these lines are determined by the ratio of the gate capacitances to the individual QDs. These lines delimit states with constant charge on both dots. The charge states of the double QD system are denoted as (n, m) , where n and m are the electron numbers of the individual quantum dots.

Since the considered quantum dots are in close proximity to each other, the charge state of one will influence the chemical potential of the other, effectively gating it due to their capacitive coupling (C_t). Accordingly, the intersection of the chemical potential lines will reveal a fine structure, where the intersection point is split into two triple points, delimiting the $(n, m) - (n + 1, m) - (n, m + 1)$ and $(n + 1, m) - (n, m + 1) - (n + 1, m + 1)$ charge states, shown in Fig. 2.8.d). This leads to the honeycomb pattern in the charge stability diagram, a characteristic signature of double quantum dot systems.

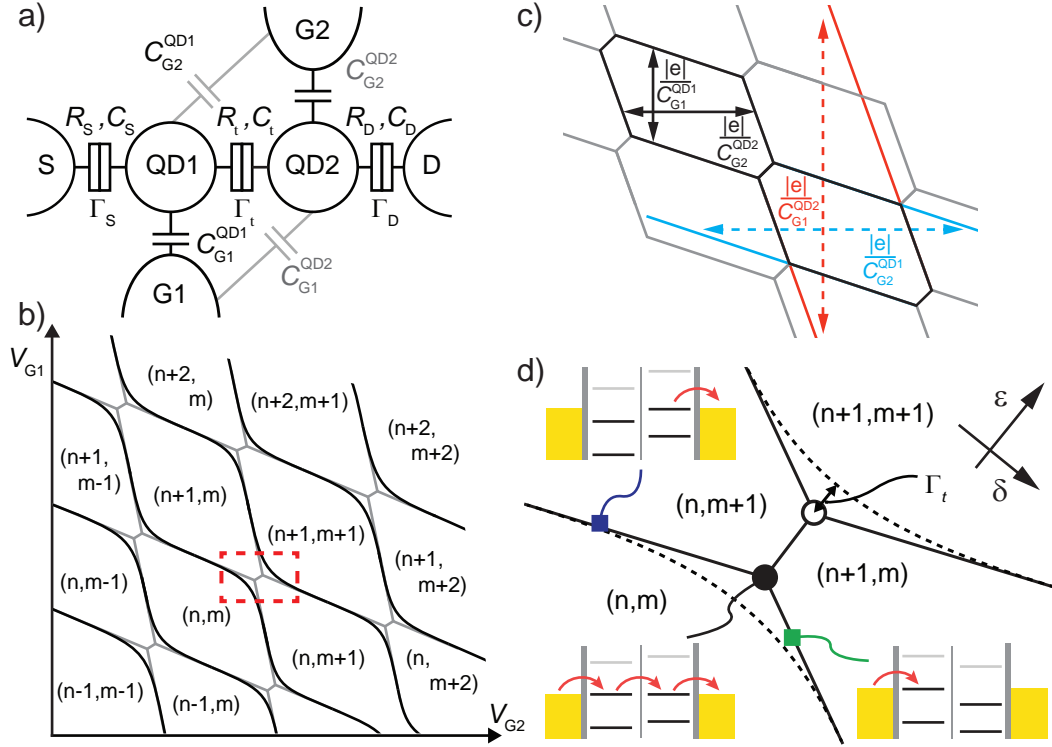


Figure 2.8.: Basics of double quantum dots | a) Capacitive model for tunnel-coupled double quantum dots in series. b) Charge stability diagram as a function of the two gate voltages for a weakly and a strongly coupled double quantum dot in gray and black, respectively. c) Hexagonal limits of an (n, m) charge state in the charge stability diagram. The peak spacing of the appropriate resonance lines yields the capacitive coupling of the gates to individual QDs. d) Close-up of highlighted area in the charge stability diagram. Full and dashed line refer to quantum dots with weak and strong coupling, respectively. The strength of the avoided crossing is determined by the Γ_t interdot tunnel coupling. Insets show possible charge transfer processes along the lines of the stability diagram.

These capacitances can be extracted in a similar manner as for a single quantum dot. The lines delimiting an (n, m) charge state, where $\delta E = 0$ for both dots is shown in Fig. 2.8.c). The peak spacing in gate voltage of the appropriate lines yields the capacitance of the examined gate to the corresponding quantum dots. These values are highlighted in Fig. 2.8.c).

For weakly interacting quantum dots (Fig. 2.9.a), considering only the capacitive coupling of the two dots is sufficient. For such QDs connected in series, electron transport can only take place if both dots are in resonance, i.e., at the degenerate triple points. In two-terminal conductance measurements, these points are usually made visible by applying a finite bias. In this case, the charge stability diagram can only be mapped out via secondary structures which are sensitive to the charging of the quantum dots, so-called *charge sensors*.

As the coupling is increased, the two quantum dot states are hybridized. The degeneracy at the triple point is thus lifted, leading to avoided crossings in the charge stability diagram (Fig. 2.9.b), where the rounding-off of these features is determined by the Γ_t intradot coupling. The increased intradot coupling will relax the conditions for electron transport, meaning conductance is visible along the avoided crossings around the triple points. For even stronger coupling, while conductance is still maximal near the triple points, it is never fully suppressed, even when one dot is detuned from resonance. In this case, the interaction of the two dots cannot be treated in a perturbation of the two wave functions, and a single molecular wave function is created. However, the local gates still have a different effect on the two lobes of the wave function, thus in Fig. 2.9.b) we map out molecular states with different character.

As the coupling is increased even further, the honeycomb-like pattern of the charge state diagram will turn into parallel lines (Fig. 2.9.c), corresponding to a large quantum dot tuned by both gates. While the transport signature points to a single quantum dot structure, the charge spreading between the two coupled dots is impeded and takes place on a $t \sim \frac{\hbar}{E_C}$ time scale [85].

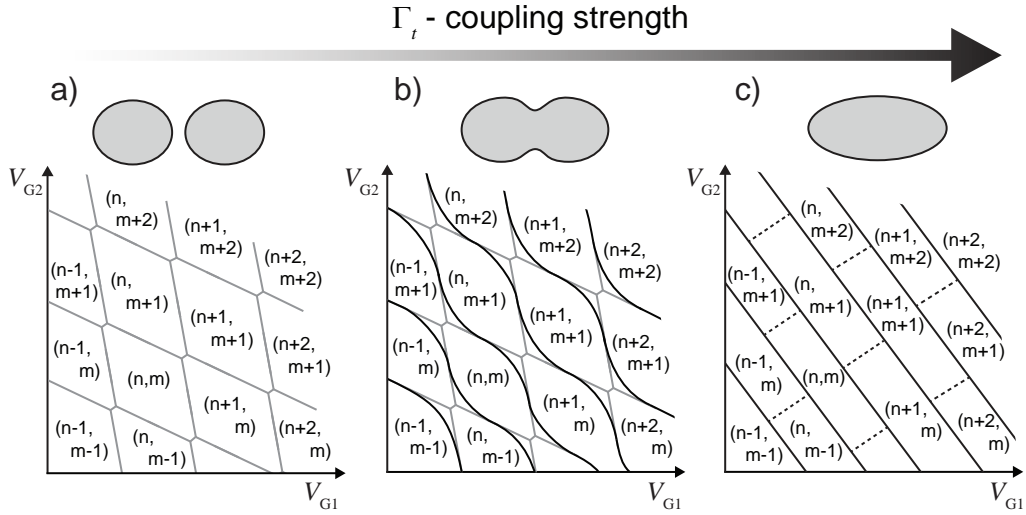


Figure 2.9.: The effect of intradot coupling on double quantum dots | Conductance of a double dot as a function of two gate voltages for different tunnel coupling strengths: a) weak ($\Gamma_t/E_C \ll 1$), b) intermediate ($\Gamma_t/E_C \approx 1$) and c) very strong ($\Gamma_t/E_C \gg 1$)

3 Indium Arsenide Nanowires

Semiconducting nanowires are crystalline quasi-one-dimensional nanostructures with diameters on the scale of a few tens of nanometers and lengths ranging from sub-micrometer to several micrometers. These nanostructures, sometimes referred to as nanowhiskers, have been synthesized from Group IV materials (Si, Ge), Group III-V (Al, Ga, In – N, P, As, Sb) and Group II-VI (Cd, Zn – Se, O) alloys and even tertiary compounds (AlGaAs).

Nanowires offer a versatile material system, put to use in a variety of applications [86,87], ranging from on-chip sensors [88,89] to nanoscale LEDs [90], photodetectors [91] and even lasers [92]. Nevertheless, it has most widely been studied as a platform for bottom-up electronics, producing high-mobility nanoscale transistors [93–95], highly efficient wrap-gated field effect transistors in lateral samples and vertical arrays alike [96–98].

The low effective mass, high mobility and small band gap make InAs nanostructures an exciting platform for investigating quantum effects. Owing to the pinning of the Fermi energy at metal interfaces, low-ohmic contact can be achieved with relative ease [99,100], making the choice of contact materials far less restricted than in two-dimensional electron gas (2DEG) systems. This has opened up the possibility to create hybrid devices [101], coupling nanostructures to superconductors [30,102] and ferromagnets [103]. The sizeable spin-orbit coupling in semiconducting nanowires has ignited renewed interest in the material system recently, for realizing solid-state devices like spin-orbit qubits [25,104] which exploit this interaction. Furthermore, it was thrust in the limelight as it served as the basis of novel research in the field of particles with non-Abelian statistics, namely Majorana fermions [42–45] and fractional fermions [26–28,46–48].

Here, the most important features of InAs nanowires are briefly reviewed, discussing the growth and crystal structure as well as the most important properties affecting electron transport. We also review the findings of previous magnetotransport experiments.

3.1. Nanowire growth

Since its discovery around 50 years ago, the vapour-liquid-solid (VLS) method has been the standard approach towards the bottom-up growth of semiconducting nanowires [105,106]. The name refers to the formation of solid crystals from vaporized precursors facilitated by liquid catalyst. Although catalyst-free self-assisted growth methods have been demonstrated and rapidly developed in recent years [107], they do

not yet rival the appeal of metal-assisted growth as they lack the yield and control over the crystal structure [108]. In the VLS process, precursor materials from the vapour phase alloy with the catalyst. As the catalyst droplet supersaturates, no further material can be accumulated and nucleation is initiated at the liquid-solid interface (Fig. 3.1.a). As the incoming vapour is incorporated in the crystal via the seed, the nanowire grows axially, while radial growth is suppressed, lifting the catalyst during the process (Fig. 3.1.b). The diameter of such a nanowire is thus determined by the size of the seed. Since the substrate is the base of the seeded growth, its crystal structure acts as a template for the first layer of the crystal.

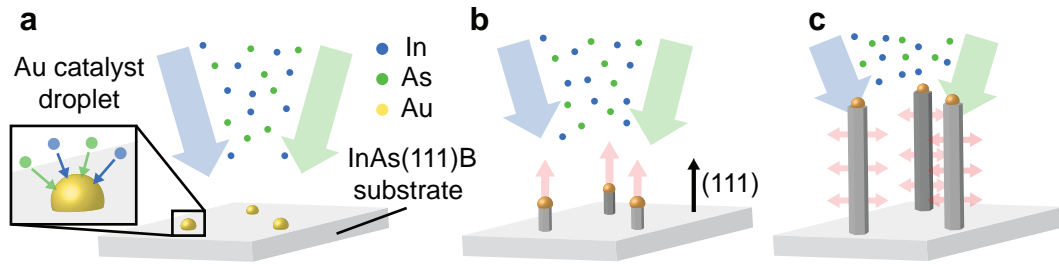


Figure 3.1.: Illustration of nanowire growth | a) Elemental In and As_2 vapour is incorporated in nanometer-scale gold catalyst droplets, facilitating seeded nucleation at the liquid-solid interface. b) Growth in the axial direction. c) Epitaxial growth in the radial direction can be achieved, as seeded growth is suppressed at lower temperatures.

Gold is regarded as the universal material of choice for metal-assisted growth, due to a variety of reasons, including its great alloying capability and inertness to oxygen [109]. Gold catalysts are most commonly created from an evaporated thin film by dewetting. By engineering the film thickness, temperature and time of the annealing, uniform droplets of the desired diameter can be formed. This method of self-assembly is preferred when high cleanliness is crucial, since it can be performed in-situ, prior to the growth process. Catalyst seeds can also be deposited from a colloidal or aerosol suspension of nanoparticles to achieve better uniformity or patterned in arrays using lithography and evaporation.

A variety of methods can be employed to feed the epitaxial growth: Metalorganic Vapour Phase Epitaxy (MOVPE)¹, Chemical Beam Epitaxy (CBE) or Molecular Beam Epitaxy (MBE). As the name suggests, MBE relies on atomic beams of the desired constituent materials are created by effusion in a UHV chamber. As the precursors are deposited, epitaxial growth is achieved in a purely physical process, contrary to CBE or MOVPE which rely on chemical decomposition of metalorganic precursors. Hence, despite the advantages of the latter methods (higher growth rate, lower expenses) - when it comes to purity - MBE is superior, since no residual materials are present in the process. [108, 110]

¹This also referred to as Metalorganic Chemical Vapour Deposition (MOCVD)

The flux of the precursors determines the growth rate, and can influence the reaction kinetics. By lowering the growth temperature, the catalyst can be deactivated, quenching axial and allowing radial growth. By changing the precursor materials, the synthesis of axial and radial heterostructures can be achieved. Prominent examples include embedded quantum dots defined by as-grown barriers (e.g.: InAs/InP structures) [111, 112] and core-shell (e.g.: InAs/GaAs) nanowires [113, 114].

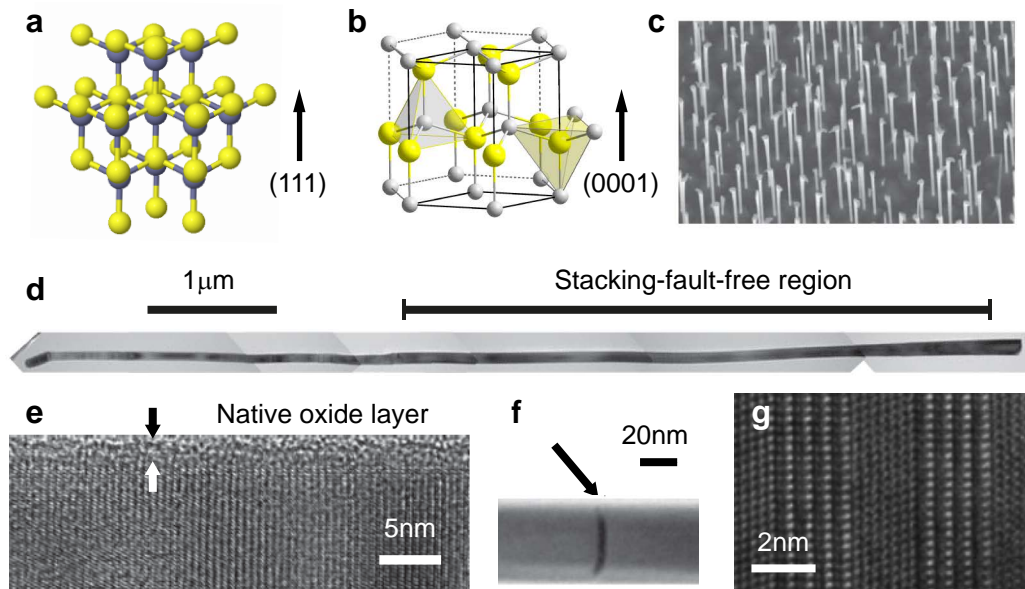


Figure 3.2.: Crystal structure of InAs NWs | a) Zinblende crystal structure [115]. b) Wurtzite crystal structure [116]. c-d) Scanning electron micrograph of as-grown nanowire forest and single nanowire, from [108]. e-f) Transmission electron micrograph of wurtzite nanowire capped by a native oxide layer and a stacking fault, from [108]. g) High resolution transmission electron micrograph of a NW with engineered twinning between ZB and WZ structure, from [117].

The focus of the studies presented in this thesis were InAs nanowires, provided at our disposal by the group of Prof. J. Nygård. These were synthesized by Au-assisted MBE growth using self-assembled catalyst droplets. Although this method ensures the high adatom purity of the samples, crystalline defects can significantly diminish the quality of nanostructures [117, 118]. The crystal structure of InAs has two configurations which fundamentally differ in the stacking sequence of layers: cubic zinblende (ZB) and hexagonal wurtzite (WZ), shown in Figs. 3.2.a-b), respectively. While the former is the characteristic crystal structure of most III-V semiconductors, the latter is typical for nitrides and structures with high surface-to-volume ratios. Hence, for nanowires there is a competition between these two phases. Defects arise as sudden changes between ZB and WZ ordering, as stacking faults or crystal twinning, shown in Fig. 3.2.f-g), respectively. Since these sudden changes can considerably modify the transport properties and lead to potential barriers, creating unwanted confinement [119], the crystal phase engineering of nanowires is of utmost importance.

To ensure monocrystalline structure, the studied nanowires were grown in a two-step process developed for the growth of stacking-fault-free NWs [120]. In the first step, small-diameter (~ 20 nm) nanowires are grown in the axial (111) direction² on an (111)B InAs substrate. Such thin NWs adopt WZ structure. In the second step, the Au-assisted growth is stopped by lowering the temperature, leading to the radial formation of a homoepitaxial shell. This shell follows the WZ structure of the core [108, 120–122], as shown in Fig. 3.1.c). This procedure thus allows the synthesis of fault-free, purely wurtzite NWs with diameters of 50-100 nm (Fig. 3.2.d).

3.2. Magnetotransport experiments in nanowires

As this thesis focuses on the investigation of magnetotransport phenomena in InAs quantum dots, here we present a brief overview of previous magnetoconductance experiments in InAs nanowires. A detailed discussion of the contact formation and summary of electronic properties can be found in Refs. [54, 123].

Electron mobility in InAs nanowires is expected to be large, due to the small effective mass, $m^* = 0.023 m_e$. Field effect measurements have yielded a large range of mobilities from a few hundred $\frac{\text{cm}^2}{\text{Vs}}$ up to $6600 \frac{\text{cm}^2}{\text{Vs}}$ [93]. Hall measurements provide a more reliable way of extracting these values, however realizing such a geometry in InAs nanowires is difficult and requires high precision lithography. Only recently could such measurements be performed by Blömers *et al.*, reporting $\mu_H = 3590 \frac{\text{cm}^2}{\text{Vs}}$ Hall mobility.

The radial charge distribution of the nanowires has been thoroughly investigated in magnetotransport experiments. While studies of small-diameter (< 40 nm) nanowires find ballistic transport [124], resolving sub-bands [125–127] which are assumed to extend over the whole cross section of the structure, most calculations [128, 129] suggest that the Fermi level pinning leads to a cylindrical charge accumulation layer near the surface, like in bulk InAs [20]. Measurements of the diameter dependence of the nanowire conductance point to the existence of such a layer [130].

Magnetoconductance measurements in magnetic fields parallel to InAs nanowires have not revealed any clear periodicity in the magnetic field, which would provide direct proof of a charge accumulation layer just below the surface of the nanowire [131]. This is in contrast to hollow InAs nanowires [132], GaAs/InAs core/shell nanowires [113, 114], or InN nanowires [133], where flux quantization effects could be observed.

Jespersen *et al.* examined universal conductance fluctuations in InAs nanowire devices as a function of the gate potential, magnetic field, and the angle between the field and the nanowire axis [134] and found no signs of electrons confined to a surface accumulation layer. In both Refs. [131] and [134], a high density of stacking faults is cited as the possible reason behind the disruption of the a surface electron gas, thus a significant improvement should be expected for stacking-fault-free nanowires.

The vast majority of magnetotransport experiments in semiconducting nanowires have focused on the study of the spin-orbit interaction, as it has been the center of attention for this material system. The spin-orbit coupling has been investigated extensively in diffusive nanowires by examining the phenomenon of weak anti-

²For WZ this is referred to as the (0001) direction.

localization [128, 135–138]. These studies have shown the spin–orbit length to be in the 60–250 nm range, giving experimental evidence of the expected strong spin–orbit coupling. Furthermore, these experiments could also be used to determine the phase coherence length of the wires, finding values of 100–800 nm [128, 131, 135–137]. Moderate (within an order of magnitude), but appreciable electric tunability of the spin–orbit length has been demonstrated in top-gated [129, 138], side-gated [139], and liquid-gated [138] devices.

The spin–orbit energy has also been directly measured in single quantum dots from the magnitude of avoided singlet-triplet crossing in excited state spectroscopy [23, 24, 140] and from the hybridization induced by the orbital Kondo effect in strongly coupled devices [141]. These studies also revealed its anisotropic [24] and tunable nature via externally applied electric fields [141]. Another approach for the study of the spin–orbit coupling in quantum dots is investigating the leakage current in spin blockade in double quantum dot systems, either induced by hyperfine mixing [140, 142] or through electron dipole spin resonance [104]. All these studies reported measurements which point to a Rashba-type spin–orbit interaction [143].

The strong spin–orbit interaction results in a large g factor in InAs ($g_{\text{InAs}}^* = -14.7$), which is retained in nanostructures. This attribute has been investigated by many studies [21, 22, 32, 34, 144, 145], since a tunable g factor can be used to selectively address individual qubits [33]. In Chapter 5, we discuss our own measurements of g -factor anisotropy and we will review the progress in this field along with presenting our findings.

4 Fabrication and experimental techniques

The success of research projects in the field of quantum electronics hinges on producing sub-micron-scale devices in a reliable manner. The fabrication of these requires state-of-the-art facilities in a cleanroom environment. However, this is only one part of the puzzle. Cryogenic temperatures and high-sensitivity measurement equipment are absolutely crucial in realizing experiments on quantum dots.

In this chapter, the standard fabrication and sample processing required to create nanoelectronic circuits are introduced. The experimental setup used for the electrical measurements and the details of the cryogenic techniques necessary to resolve quantum phenomena are also discussed.

4.1. Device fabrication

Over the course of this thesis project, a vast number of devices were fabricated in a large variety of geometries using different materials. While the peculiarities and design of the samples varied depending on the goal of our experiments, the fabrication of all InAs nanowire-based devices relies on the patterning of contact and gate electrodes, which is based on the same process and described in the following sections.

4.1.1. Nanowire deposition and location

The initial step of sample fabrication is the cleaning of the substrates. All devices discussed in this thesis are fabricated on $\approx 500 \mu\text{m}$ thick highly p -doped silicon wafers, capped with a 400 nm thick silicon oxide layer. These wafers are diced to sizes appropriate for lithography and then cleaned. The substrates are cleaned in subsequent ultrasonic bath treatments in acetone, deionized water and 2-propanol. The wafer is subsequently exposed to an ultraviolet light and ozone treatment to further remove organic residues.

In order to be able to locate nanostructures and design electronic circuits on them, a predefined frame of reference is needed. To achieve this, a so-called *base structure* needs to be created using standard electron-beam lithography (EBL) and metallization procedure (described in Sec. 4.1.2). The $2 \text{ mm} \times 2 \text{ mm}$ base structure shown in Fig. 4.2.a) consists of alignment markers, large leads, bonding pads, and a $0.5 \text{ mm} \times 0.5 \text{ mm}$ square grid of fine reference markers spaced by $20 \mu\text{m}$.

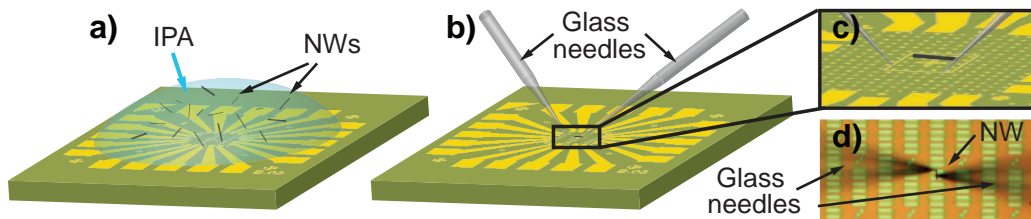


Figure 4.1.: Illustration of nanowire deposition techniques | a) Drop casting from NW/IPA suspension. b-c) Single nanowire placement using glass needles. d) Optical microscope image of a nanowire and two glass needles over a wafer.

Wafer preparation is followed by nanowire (NW) placement. Predominantly two deposition methods were employed in our lab. In most cases, NWs are deposited from a NW/IPA suspension (created by covering a wafer piece of as-grown NWs with minute amounts (< 0.1 ml) of IPA and sonicating it). A small droplet ($< 1 \mu\text{l}$) is cast over the base structure, and the IPA solvent almost instantaneously evaporates, leaving behind randomly distributed nanowires which remain on the substrate due to the van der Waals interaction (Fig. 4.1.b).

In contrast, some proposals require precise placement and orientation of the nanowires. This can be achieved by transferring single nanowires with the help of micromanipulator-controlled glass needles under a special far-field microscope (facilities provided by Prof. M. Poggio). This deposition technique is illustrated in Figs. 4.1.b-d) and discussed in depth in the thesis of Samuel d’Hollosy [54].

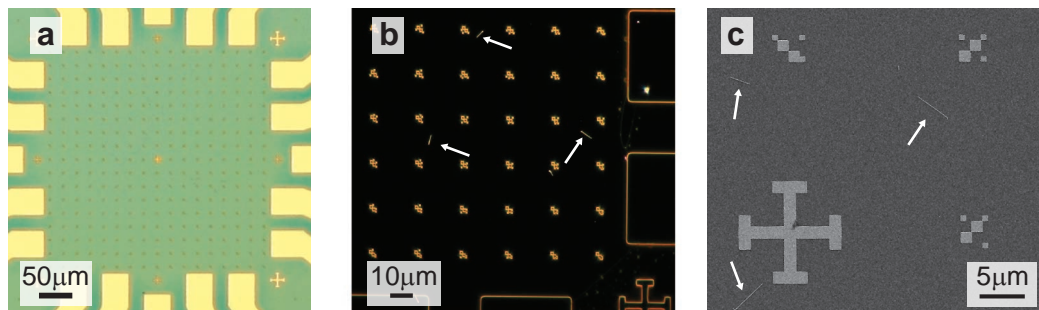


Figure 4.2.: Nanowire location | a) Marker grid used as a reference frame and for lithography alignment. b) Dark-field optical microscope image and c) scanning electron micrograph used for NW location. The arrows highlight individual nanowires.

In order to locate the deposited NWs, the marker grid is imaged by dark-field optical microscopy (Fig. 4.2.a) or by scanning electron microscopy (Fig. 4.2.b), if high precision is required. The relative coordinates of the NWs are determined with respect to the closest markers using image processing software¹. The coordinates on the base structure

¹In some cases, this was also necessary to correct for skewed images due to SEM imaging artefacts.

are then calculated, and used to design the circuits in the Elphy software suite provided with the RAITH electron-beam lithography system.

These designs are then used to create evaporation masks for InAs NW nanoelectric circuits by lithography and metallization (see Sec. 4.1.2). Depending on the materials used, this might be done in several steps, one for each material. The specific details of the devices are discussed in the individual experimental chapters.

4.1.2. Lift-off technique

Electron-beam lithography (EBL) is a fundamental technique used in semiconductor technology to define nanometer-scale structures. This is achieved by creating high-resolution evaporation masks from a layer of resist. For all samples discussed in this thesis, lateral patterning was performed using a Zeiss Supra 40 scanning electron microscope and an attached Raith lithography system, which allows precise control of the electron beam. The steps of the EBL and subsequent metallization process are illustrated in Fig. 4.3.

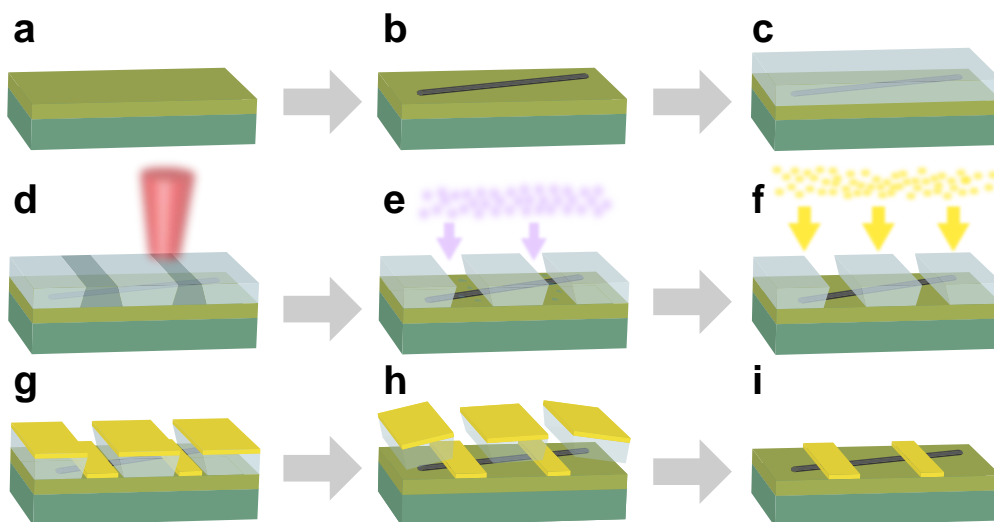


Figure 4.3.: Standard lift-off process using electron-beam lithography. | a) Cleaning of Si/SiO₂ substrate. b) Nanowire deposition. c) Spin coating with resist. d) Patterned irradiation using electron-beam lithography. e) Evaporation mask created after development, cleaned by O₂ plasma etching. f-g) Metallization by evaporation. h) Lift-off, removing unwanted metal in unexposed areas. i) Finished device with metal contacts.

Following the preparation of the wafer for the lithography process (Fig. 4.3.a-b), a film of resist is created by spin-coating the substrate with a polymer solution, by depositing a droplet of resist on the substrate which is then spun at 4000 rpm for 40 s. This results in a thin, homogeneous polymer layer by evenly spreading out the coating and removing the excess (Fig. 4.3.c). The wafer is then annealed at 180 °C on a hot plate in order to harden the resist solvent and remove any residual water. The thickness

of the film can be controlled by changing the spin speed and the concentration of the polymer solution. For most devices a standard recipe (see Appendix A) was used, which results in a ~ 350 nm thick films of 950K (molecular weight) polymethyl-methacrylate (PMMA) or ZEP520A (Zeon Chemicals) [17, 146].

Upon irradiation by a focused beam of electrons (Fig. 4.3.d), the polymer strands in the film are broken up into shorter segments. The exposed areas of the film can be removed by use of a developer solution in which only the irradiated polymers are dissolved, while the rest of the film remains, creating a patterned mask (Fig. 4.3.e). One has to choose the correct parameters for film thickness and electron beam dose to produce a slanted, so-called undercut profile (Fig. 4.3.d). This is preferred for the metallization of the sample as it ensures the discontinuity of the metal film around the exposed areas.

Due to the imperfect nature of the development process, polymer residues still cover the bottom of the trenches in the mask (Fig. 4.3.e). This contamination is removed by either an O_2 plasma process in a reactive-ion etcher (RIE) or in-situ Ar^+ ion milling. The former refers to a chemical dry etch process, in which carbohydrates are selectively oxidized using a plasma of highly reactive monatomic oxygen. In the latter method, the sample is bombarded with high-velocity Ar^+ ions, these physically sputter away the contaminants. Since this does not only affect the resist, it is usually used in case the removal of a thin oxide layer is also required (e.g. the native oxide of the nanowires).

Metallization of the structures is done in a vacuum chamber where a metal target is heated above its sublimation point by means of electron beam exposure or resistive heating (Fig. 4.3.e). This way, a metal vapor is created which produces a film of nanometer-scale thickness on a sample positioned at a large distance at a right incidence angle.

As sketched in Fig. 4.3.f), the metal film breaks at the edges of the exposed areas. By using the appropriate solvent, one can dissolve the mask and remove the metal from the unexposed areas of the sample (Fig. 4.3.g). This last step of the process is referred to as *lift-off*. Following this, we are left with a sample where the surface is metallized only in certain areas, as shown in Fig. 4.3.h).

Contact formation - Ar^+ milling, passivation

Nanowires form an amorphous native oxide cap under ambient conditions, as seen in Fig. 3.2.e). To create ohmic contacts to the NWs, this insulating layer needs to be removed prior to the evaporation of the source and drain electrodes. We used two methods for oxide removal, Ar^+ ion milling and sulphur passivation [147], both well-established in the field [148]. As discussed before, in case of Ar^+ sputtering, the oxide is physically removed by bombardment. This is also useful for the removal of oxide layers covering metal films to ensure ohmic contact. Wet etching with water-based NH_4S_x solution removes the oxide layer and creates a passivation layer on the surface. As this layer can disintegrate under ambient conditions, this has to be minimized by building the sample into a vacuum system as soon as possible.

4.1.3. Wire bonding

In the last step of fabrication, the wafer piece is glued into a commercially available non-magnetic chip carrier with conductive silver paste. This allows us to connect to the p -doped silicon substrate and use it as a global back gate. The metallized circuits on the wafer are connected to the contact pads of the chip carrier by wire bonding, as shown in Fig. 4.4. An ultrasonic wedge bonder creates contacts by wedging an aluminium or gold wire between the chip and the bonding tip of the machine. A small force is applied to the tool while also vibrating it at its ultrasonic resonance frequency, melting the wire, binding it to the bonding pad and creating ohmic contact to the chip carrier. Choosing the right parameters for the bonder is crucial as one has to ensure good adhesion while making sure that the applied force and ultrasonic power are not large enough to create conducting channels in the silicon oxide capping layer, shorting the contact to the back gate. This is commonly referred to as a gate leak. When working with nanoelectronic circuits, one has to ensure that both the sample and the machine are well grounded, as accumulation of static electric charge can lead to electrostatic discharges (ESD), resulting in a surge of current that can easily damage or destroy the devices.

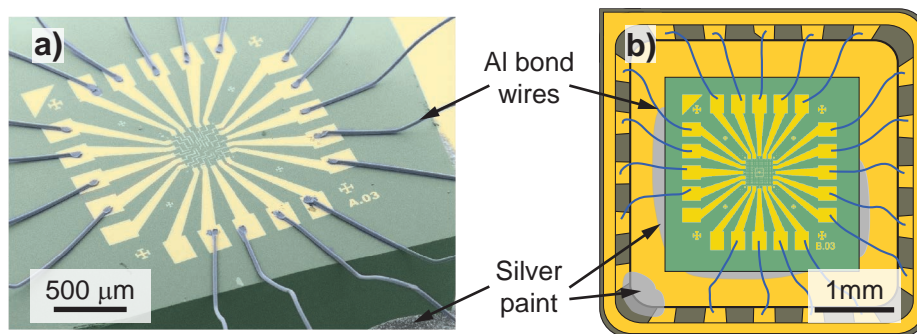


Figure 4.4.: a) False-colored scanning electron micrograph and b) schematic illustration depicting a bonded sample in a chip carrier.

4.2. Experimental setup

Resolving electronic quantum phenomena - where the energy scales involved are on the order of meVs - requires sub-Kelvin temperatures. Low-temperature transport experiments on nanoelectronic circuits also pose stringent requirements on applicable voltages, noise levels, stability and sensitivity of the measurement equipment.

The working principle of the commercially available cooling systems we employ in our lab to reach cryogenic temperatures is discussed in Sec. 4.2.1. The standard experimental setup used for the electrical measurement of our devices is presented in Fig. 4.2.2.

4.2.1. Cryogenic techniques

The low temperatures required in our experiments are attained using commercially available cryostats. Here, we discuss the working principle of the cooling systems we employ in our lab. A schematic illustration of the used systems is shown in Fig. 4.5.

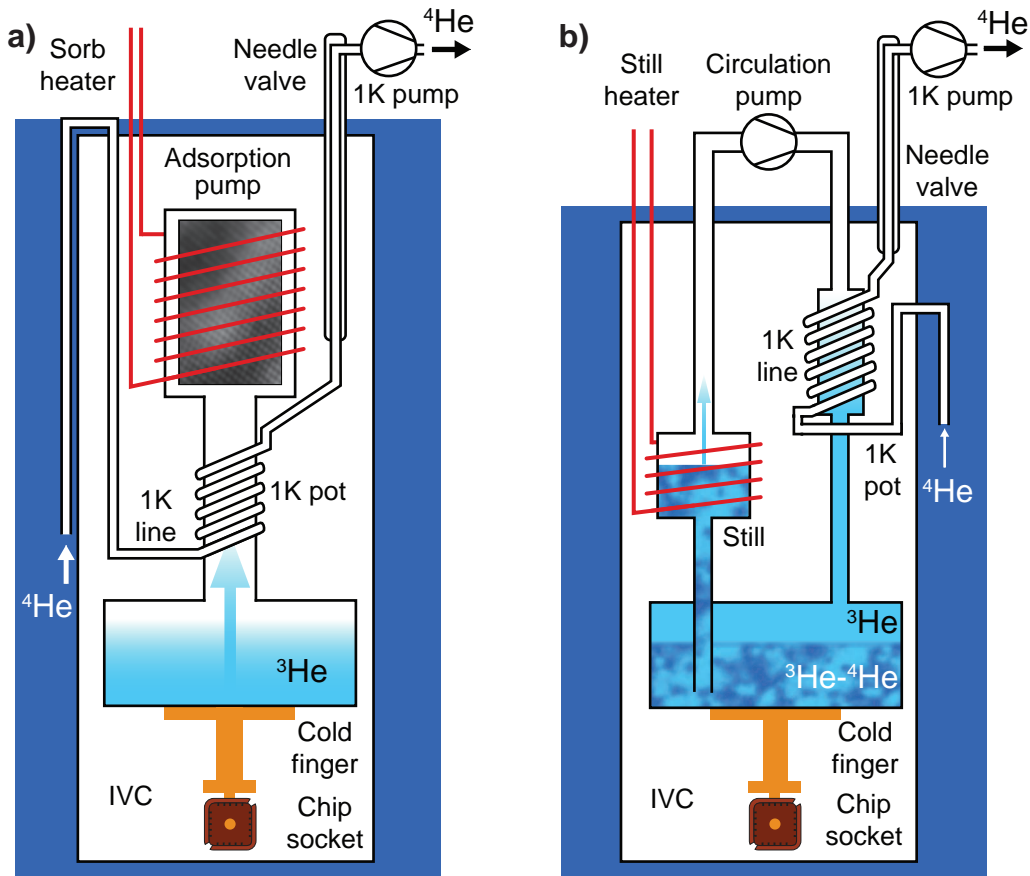


Figure 4.5.: Schematics of the employed cryogenic systems | a) ^3He cryostat setup. b) Dilution refrigerator setup.

In Fig. 4.5.a), we show a simplified diagram of a ^3He cryostat, where temperatures below 1 K can be obtained by pumping on a chamber filled with liquid ^3He . By removing the fast-moving atoms from the vapor, evaporative cooling is achieved. Since ^3He is rare and expensive, to avoid losses, this is done in a closed cycle. Gaseous ^3He is liquefied using a so-called 1-K pot, which relies on evaporative cooling of ^4He from the bath. The gas condenses in a small chamber called the ^3He pot, pumping on the created vapor is done with an adsorption pump (sorb). This is not a continuous cycle since at one point all ^3He is evaporated. To regenerate the system, the sorb is heated, leading to the desorption of ^3He which then recondenses in the ^3He chamber. The typical cycle time of one condensation in the used Oxford Heliox system is 3-4 days, however by fine tuning the ^4He flow, this could be prolonged to 6 days.

To obtain temperatures even one order of magnitude lower, so-called dilution refrigeration is used. A sketch of such a system is shown in Fig. 4.5.b). The basic idea behind this type of cooling is that below 870 mK, ^3He - ^4He mixtures separate into ^3He -poor and ^3He -rich² phases and form a phase boundary. An osmotic pressure difference between the two phases can be created by pumping on a so-called still. This allows us to cleverly transfer ^3He through the phase boundary, and this endothermic process cools the mixing chamber in turn. As it can be seen in Fig. 4.5.b), this is done in a continuous cycle using room-temperature pumping and 1-K pot recondensation. Utilizing this clever scheme, temperatures below 30 mK are easily attainable in commercial systems, and with improvements this number can go as low as 2 mK.

The cooling of the sample is achieved by bringing the cryostat wiring and the sample into good thermal contact with the cooling unit. The thermal anchoring of the cables is achieved via the so-called cold finger, a metallic sample stage with high thermal conductivity, usually made from copper. This is located in an inner vacuum chamber (IVC), isolating it from the surrounding ^4He bath of the vessel, which is cooled and shielded by the nitrogen jacket and the outer vacuum chamber (OVC). As all the schemes discussed above require a constant supply of ^4He for cooling/recondensation, these are known as wet systems. In next-generation systems, the role of the 1K pot is assumed by a heat exchanger, such as a pulse-tube cooler, eliminating the need for a constant need for refilling liquid ^4He .

4.2.2. Measurement setup

Samples bonded into chip carriers are built into the cryogenic systems using corresponding chip sockets mounted on the cold finger. We shield the chip socket from outside radiation using a Faraday cup. The inner sample space is then covered by the IVC cover and pumped down to pressures below 10^{-5} mbar. Usually this is done over night, as prolonged pumping could significantly improve the device conductances [149]. Lines with multiple filtering stages connect the chip socket to the outside world. Home-made "breakout boxes" are used as an interface between the cryostat leads and the BNC cabling of the room temperature instruments. This also allows us to address each lead individually and selectively ground them. A simplified diagram of electrical connections and used equipment is shown in Fig. 4.6.

As our devices exhibit typical resistances in the order of 10 k Ω and above, we measure the current through our system as a voltage bias is applied. We employ an SR830 (Stanford Research Systems) lock-in amplifier for homodyne detection. The low-frequency (typically 77 or 133 Hz) AC excitation signal is fed through a transformer with a 4:1 down-conversion factor and added to a DC bias voltage, supplied by a YK7651 (Yokogawa Electric Corp.) voltage source. This transformer also decouples the ground of the amplifier and the rest of the setup. The combined signal is then attenuated using a voltage divider (10^{-3} or 10^{-4}) to achieve $V_{\text{ac}} \sim 10\text{-}100 \mu\text{V}$ excitation on the source electrode. The resulting current is amplified using a SP983 current-to-voltage converter (Electronics Workshop, University of Basel), usually operated at a $10^7 \frac{\text{V}}{\text{A}}$

²Basically all ^3He .

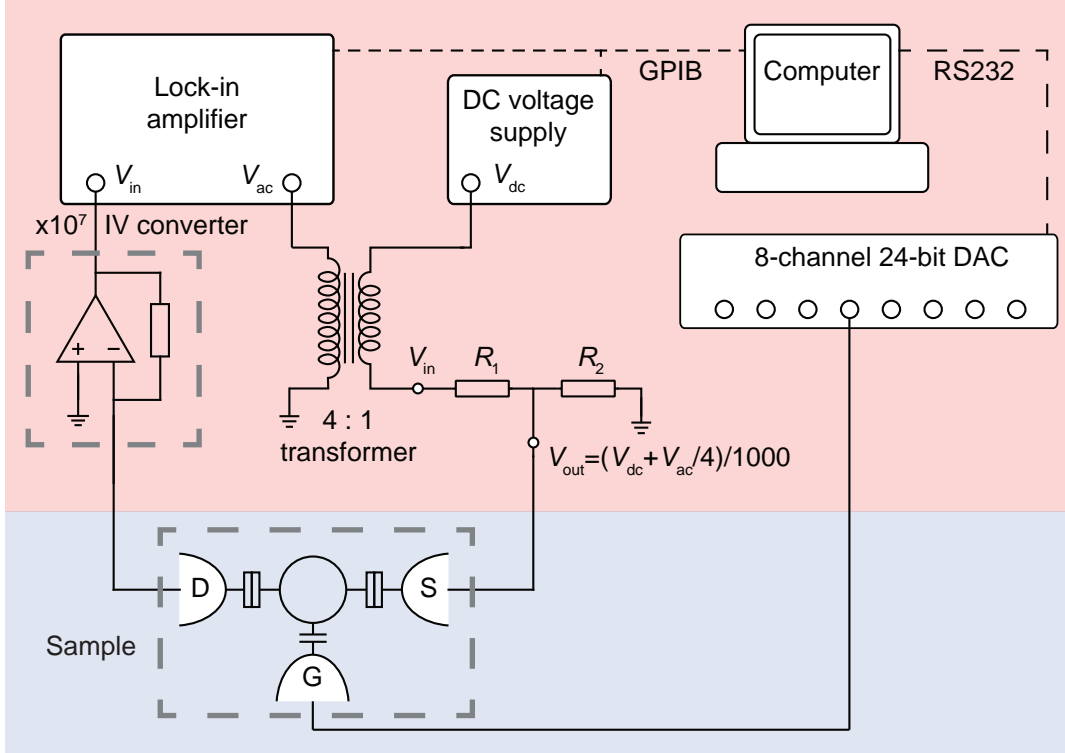


Figure 4.6.: Connection diagram of a standard measurement setup | Red (blue) shading indicates the room-temperature (low-temperature) portion of the setup

conversion factor. Feeding the output voltage of the amplifier to the lock-in, the phase sensitive response of the differential conductance ($G = \frac{dI}{dV} \approx \frac{I_{ac}}{V_{ac}}$) can be measured.

Gate electrodes can efficiently tune the potential landscape of the device, tuning electron densities, barrier heights, etc... Voltages are applied to gate electrodes using a SP927 8-channel 24-bit digital-to-analog dc source (Electronics Workshop, University of Basel). Since the operation range of this instrument is between ± 10 V, for higher voltages, a single-channel YK7651 source is used.

Experiments were conducted with a computer-controlled setup, using a LabVIEW program which communicated with all instruments and was responsible for data acquisition. Communication with the instruments was realized using *GPIB*³ or serial *RS232* connections.

One of the main issues of such setups is the formation of so-called *ground loops*, i.e. a voltage between different ground connections despite nominally having the same potential. This issue is hard to circumvent, however it can be minimized by operating most instruments with a floating ground and anchoring the ground of the cryostat housing with a single connection. As each ancillary connection for thermometers, heaters, etc. is grounded, these may lead to spurious ground loops. If possible, these are kept disconnected to reduce the noise.

³General Purpose Interface Bus

Setups such as this are very susceptible to the electromagnetic fields of the outside world which can induce significant noise. To counter this, several stages of filtering are employed. As the electron and phonon heat are decoupled below 1 K, the above mentioned temperatures refer to the T_{cryostat} of the cooling unit of the cryostat, while the electron temperature is not as low $T_{\text{el}} > T_{\text{cryostat}}$. However, with the appropriate filtering T_{el} can be significantly reduced. High frequency (10 MHz+) radiation load on the wiring of the cryostat is suppressed using tapeworm filters at the feedthrough of the Faraday cage. The wiring of the cryostat is done with twisted pair to cancel out electromagnetic interference from external sources or crosstalk between lines. A further filtering stage of room-temperature pi filters (cut-off above 1 MHz) may be applied to the individual lines if needed.

5

g-factor Anisotropy in InAs Nanowire Quantum Dots

The coupling strength of the electron spin and the magnetic field is formulated in the so-called g factor. The Zeeman energy splitting of the spin species is given by $E_Z = g\mu_B B$. Understanding how the electron spin and the magnetic field are connected, and how it is affected by external parameters is crucial for the assessment of any magnetotransport phenomenon. This knowledge is also required for creating structures with locally defined spin projection axes [29]. Furthermore, the ability to selectively address spin qubits - the basic building blocks of spin-based quantum computation [18, 19] - hinges on a tunable g factor [33]. Consequently, gaining better insight bears importance both within and beyond the scope of this thesis.

Free electrons possess a g factor of $g_e = +2.0023$, a value determined by relativistic quantum mechanics. In bulk semiconductors, the effective g factor (g^*) is given by the band structure, and is thus influenced by multiple factors such as the semiconducting energy gap or the spin-orbit energy of the split-off band [76]. As we move towards nanostructures of smaller dimensions, the confinement plays an increasingly important role, moving the g factor towards the vacuum free electron value of g_e [77–79, 150]. Thus by tuning the confinement, through modifying the geometry [77] or by influencing the potential landscape of the device [22, 144], one can adjust the Zeeman energy and selectively address quantum dots with microwaves [25, 32, 104, 151] to perform operations on certain spin qubits.

Multiple techniques exist for extracting the effective g factors of QDs from dc transport experiments. Mapping out the field evolution of the Coulomb oscillations via gate sweeps is probably the most common method of g -factor measurements, as it is not restricted to certain coupling regimes [22, 77, 152]. A more direct way of achieving this is excited state spectroscopy in a magnetic field [77, 152], however it is restrictive to QDs with weak coupling. In case of stronger coupling, the g factor can be attained from the splitting of the Kondo co-tunnelling feature [21, 75, 144]. Despite the differences in these techniques, comparative studies have shown no significant difference in the yielded results [152]. Electron dipole spin resonance (EDSR) [153] is a more recent technique which uses radio-frequency electric fields to probe spins in semiconducting quantum dots [25, 32, 104, 151]. In EDSR, the rf excitation induces a resonant breakdown of the spin blockade in a double quantum dot, and so by measuring leakage currents one can not only extract the magnitude of the Zeeman energy but also probe spin dynamics, making this a quite powerful tool.

The effect of geometry-induced confinement was meticulously examined in InAs nanowires of different lengths embedded between InP barriers by Björk *et al.* [77]. This study found that as the dimensions are reduced, the $g_{\text{bulk}}^* = -14.7$ factor converges to the free electron value of $g_e = +2.0023$ faster than what would be expected simply from the increase in the confinement energy. Theoretical work on the subject validated these findings and attributed the effect to the *quenching of the orbital moment* [78, 79, 154], i.e. excited states of higher orbital moments being squeezed out and the ground state rather mixing with the continuum of states outside the QD. Anisotropic confinement thus can manifest as an anisotropy in the g factor, the magnitude of which can significantly vary from state to state [155]. While most experimental values correspond to a reduction of $|g^*|$, multiple studies in semiconductor systems have also found a state-dependent enhancement, with values significantly exceeding the bulk material values [21, 32, 152], however no clear explanation is given for these discrepancies.

So far, we have only discussed the g factor as a singular value describing the system. However, anisotropies in the band structure and confinement considerably influence the values of g^* , depending on the direction of the applied magnetic field. This anisotropy can be described by a diagonal g^* tensor. The effective g factor at arbitrary field orientation is thus given by

$$g^*(\mathbf{B}) = \frac{1}{|\mathbf{B}|} \sqrt{g_1^* B_1 + g_2^* B_2 + g_3^* B_3}, \quad (5.1)$$

where $g_{1,2,3}^*$ are the diagonal elements of the g^* tensor and $B_{1,2,3}$ are the components of the applied \mathbf{B} magnetic field vector along the principal axes of the g^* tensor.

So far, experimental studies of the anisotropy have been undertaken on quantum dots defined in many bottom-up systems: carbon nanotubes [145], InAs [32, 34] and InSb nanowires [104], or self-assembled InAs nanostructures [144, 156]. Other, non-transport measurements were also used to map out the anisotropy of the g factor by means of magnetocapacitance [157] and optical [158] spectroscopy. The electronic tunability has also been explored in self-assembled InAs devices, as well as, bent carbon nanotube devices, finding slight but noticeable changes in the magnitude and orientation of the anisotropy [22, 144, 145].

In the present chapter, the g -factor anisotropy of an InAs nanowire quantum dot is explored with two different techniques for two different charge states. Both yield similar values ranging from 5 to bulk-like 15 and corresponding to diagonal g tensors. While the anisotropy follows the theoretical expectation, the principle axes of the tensor could not be correlated with the elongated dot geometry, seemingly pointing in arbitrary directions. The presented work is a result of a common project with colleague Samuel d'Hollosy, who conducted the experiments, while sample fabrication and data evaluation were performed in tandem. Some of these findings were published in Ref. [34].

5.1. Experimental results

A thorough investigation of the g -factor anisotropy is carried out on an InAs nanowire quantum dot formed between two Ti(5 nm)/Al(100 nm) contacts, 250 nm apart (Fig. 5.1.a). The experiments were carried out in a dilution refrigerator equipped with a two-axis vector magnet at a base temperature of ≈ 60 mK. The nanowire was oriented at a $43 \pm 5^\circ$ angle with respect to the z -axis magnet.

By virtue of the vector magnet, the g factor could be mapped out at multiple azimuthal field orientations (θ) in the x - z plane of the magnet. Such azimuthal scans were recorded in two planes at polar angles of $\varphi_{\text{green}} = -25^\circ$ and $\varphi_{\text{blue}} = 20^\circ$ with respect to the sample plane, as shown in Fig. 5.1.b). This was achieved by rotating the refrigerator insert with respect to the magnet plane, which ultimately also limited the maximum achievable rotation due to the restrictions imposed by the gas handling system of the setup.

The quantum dot exhibited strong coupling to the leads, which precluded the use of excited state spectroscopy, but in turn resulted in clear signs of Kondo correlations, allowing us to pursue the extraction of the g factor with both the gate sweep and Kondo splitting method for two different charge states. The details of the employed methods and the results are presented in the following sections.

5.1.1. Zeeman shift of resonance position

Tracking the field evolution of ground state transitions as a function of the back gate voltage is a very straightforward technique. One can easily identify the spin-split levels and extract the Zeeman energy by subtracting the charging energy from the addition energy:

$$E_Z(B) = E_{\text{add}}(B) - E_C = g\mu_B |B|. \quad (5.2)$$

In such a way, one can acquire the g values from the linear slope of magnetic field dependence of the addition energy, while tracing out other spurious effects, such as the diamagnetic shift of the whole spectrum.

The g factor can thus be attained from the shift in the position of a single resonance:

$$|e\alpha_{\text{BG}}\Delta V_{\text{BG}}^{\text{res}}(\mathbf{B})| = \frac{1}{2}g^*\mu_B |\mathbf{B}|, \quad (5.3)$$

where $\Delta V_{\text{BG}}^{\text{res}}$ is the voltage shift incurred by the resonance and α_{BG} is the lever arm of the back gate which is inferred from the slopes of the Coulomb diamonds measured in bias spectroscopy.

The magnetic field dependence of a resonance at an arbitrary orientation of the magnetic field is shown in 5.1.c), which reveals a clear linear shift, symmetric around zero field. Moreover, the conductance is strongly suppressed for fields below 150 mT. This is a signature of the aluminium contacts, as such fields are insufficient to quench the superconductivity in the leads. The resonance position is extracted from the conductance maxima of the gate traces of the map. Linear regression is performed on the resulting $V_{\text{BG}}^{\text{res}} - B$ data pairs and the g^* is calculated from the obtained slope, according to Eq. (5.3).

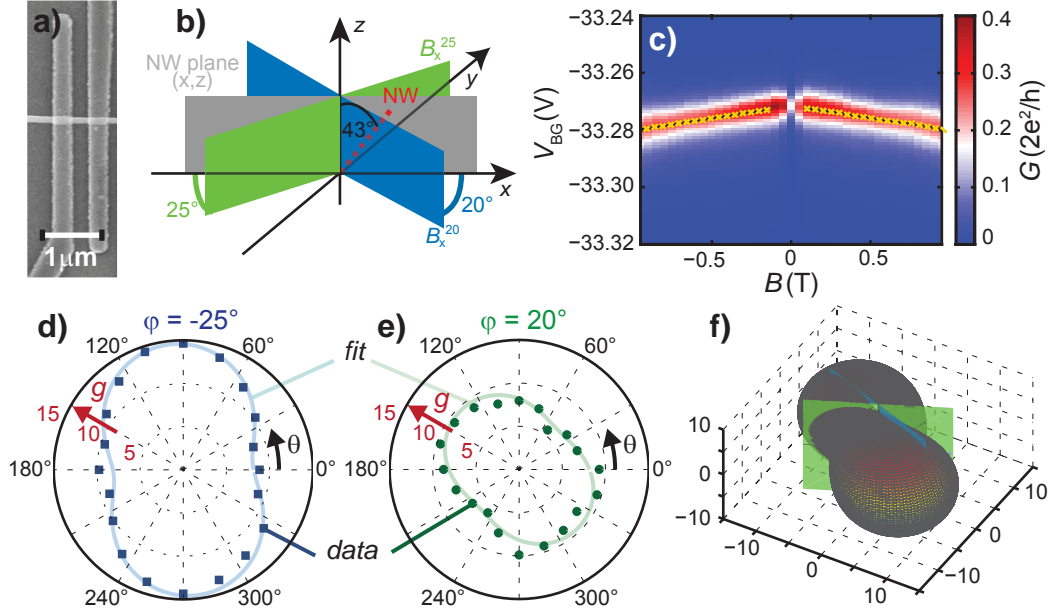


Figure 5.1.: Anisotropy of the QD g factor from Zeeman shift | a) Scanning electron micrograph of the studied device. b) Sketch of the measurement arrangement, anisotropy was probed for magnetic field orientations in two planes, at $\varphi_{\text{green}} = -25^\circ$ and $\varphi_{\text{blue}} = 20^\circ$. c) Typical magnetic field evolution of a single resonance at an arbitrary field orientation. d-e) Anisotropy of the g factor extracted at different orientations for planes at $\varphi_{\text{green}} = -25^\circ$ and $\varphi_{\text{blue}} = 20^\circ$, respectively. Data is fitted to a diagonal g tensor with rotated principle axes. f) 3D representation of g -factor anisotropy attained from the fitting.

Conductance maps, such as the one presented in 5.1.c) are acquired and subsequently evaluated for several field rotations (θ) in the two measurement planes. The polar plots of Fig. 5.1.c-d) show the azimuthal dependence of $|g^*(\theta)|$ at fixed polar angles φ_{blue} and φ_{green} . We find a strong anisotropy of the g factor where the extracted values range from bulk-like $|g_{\text{max}}^*| = 14.6$ at a field orientation of $\theta = 90^\circ$, $\varphi = -25^\circ$ down to a significantly reduced $|g_{\text{min}}^*| = 5.6$ for $\theta = 54^\circ$, $\varphi = 20^\circ$.

To better understand the variations, we fit the acquired values to a diagonal g tensor with a rotated frame of reference. The resulting fit (shown as solid curves in Fig. 5.1.c-d)) is in good agreement with the measurement and allows us to reconstruct the three-dimensional anisotropy, as shown in Fig. 5.1.f).

It is evident that while this technique is quite robust, it requires the stability of a device over larger gate ranges, especially when the same protocol has to be carried out several times over an extended period of time to map out the anisotropy. In our nanowire device, the stability demand could only be met for the tracking of a single resonance, as sweeping the gate voltage over multiple resonances can easily induce a rearrangement of trapped charges, since our work point was at negative back gate voltages in excess of -30 V. We assumed that additional, orbital effects could be neglected when studying the low-field behaviour of a quantum dot with high electron occupancy.

5.1.2. Kondo Splitting

To gain better insight into the asymmetry and further consolidate our findings, we turned to employ another method for a *different* charge state. We investigated the field evolution of Kondo correlations, the emergence of which is allowed by the strong coupling of the quantum dot.

In case of normal metal contacts, this is manifested as a zero-bias ridge of elastic co-tunnelling in the middle of Coulomb diamonds at odd occupancy. Superconducting contacts significantly modify this picture [159], hence the Coulomb diamonds exhibit quasiparticle co-tunnelling lines at even ("E") occupancy and a much more elaborate structure of sub-gap states for an odd ("O") number of electrons, as seen in Fig. 5.2.a). This is often referred to as Kondo-enhanced Andreev transport [160–163]. Later studies revealed this phenomenon to be a special case of so-called Yu-Shiba-Rusinov states, arising from the hybridization of a superconductor and a magnetic "impurity", i.e. a spinful quantum dot [164–166]. While this is an interesting phenomenon, the investigation of the superconducting features reach beyond the scope of this work and are not discussed in this thesis.

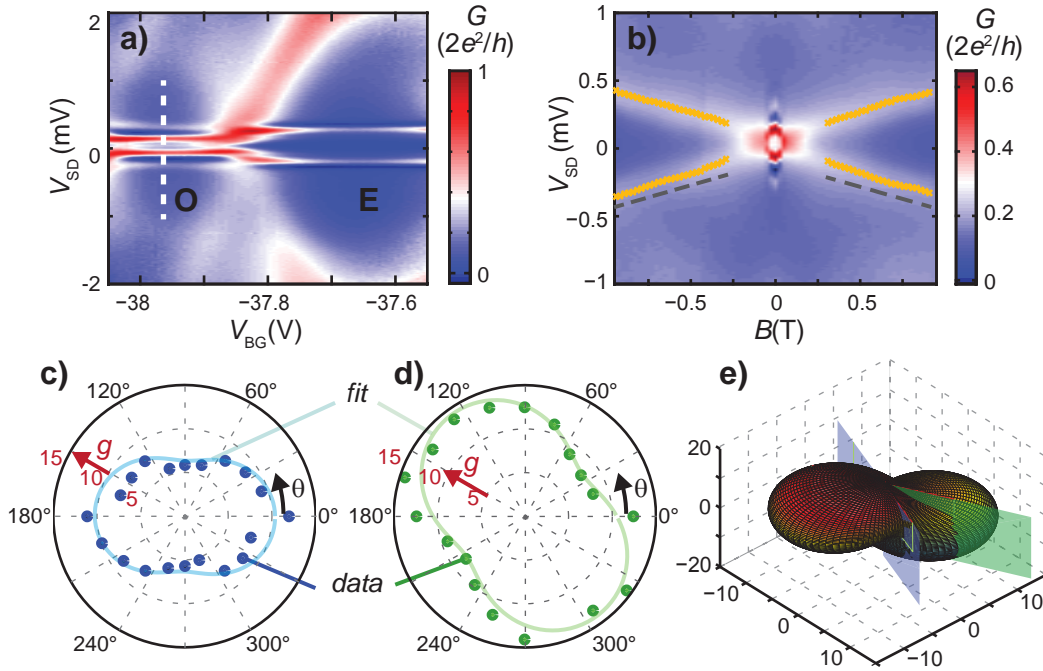


Figure 5.2.: Anisotropy of the QD g factor from Kondo splitting | a) Differential conductance as a function of V_{BG} and V_{SD} at $B = 0$, the dashed line indicates the gate position where the field dependences were recorded. Notice the Kondo-enhanced sub-gap features at odd filling. b) Typical magnetic field evolution of the split Kondo co-tunnelling feature at an arbitrary field orientation. c-d) Anisotropy of the g factor extracted at different orientations for planes at $\varphi_{\text{green}} = -25^\circ$ and $\varphi_{\text{blue}} = 20^\circ$, respectively. Data is fitted to a diagonal g tensor with rotated principle axes. e) 3D representation of g -factor anisotropy attained from the fitting.

For the purpose of the experiments, the gate voltage is parked in the middle of the odd ("O") diamond to record bias traces at different magnetic fields [21, 75]. Such a map is shown in Fig. 5.2.b) for an arbitrary orientation. As the applied magnetic field is increased, the Δ^* superconducting gap parameter is reduced and eventually superconducting features disappear as the field surpasses 200 mT and the contacts are driven to the normal state. Above T_C , a widened zero-bias conductance resonance develops as a result of the Kondo correlations. As the field is further increased, the Kondo ridge splits into two branches of inelastic spin-flip co-tunnelling lines occurring at

$$\Delta V_{\text{SD}}^{\text{res}}(\mathbf{B}) = \frac{E_Z}{e} = \pm \frac{1}{e} g^* \mu_B |\mathbf{B}|. \quad (5.4)$$

These conductance features are identified in each trace, and the g factor is attained from the slope of a linear fit to the peak maxima (yellow crosses). To improve the accuracy of the fit, its range was limited to the $250 \text{ mT} < B < 500 \text{ mT}$, thus excluding contributions from the superconducting regions and any inelastic co-tunnelling process that could arise at higher bias. This procedure is repeated at different angles of the magnetic field and the anisotropy of the g factor is mapped out at the two φ polar angles in the same manner as for the previous method.

The measured values shown in Fig. 5.2.c-d) lie between $|g_{\text{max}}^*| = 5.2$ and $|g_{\text{min}}^*| = 15.3$, slightly above the bulk value. The magnitude of this anisotropy – as well as the orientation dependence – are quite similar to that of the previously studied charge state, however the extremal values occur for quite different field orientations. Once again, the 3D anisotropy was reconstructed in Fig. 5.2.e) from the fitted curves in Fig. 5.2.c-d).

5.1.3. Discussion

The angular dependence study of the g factor anisotropy in different charge states revealed a similar variation of $|g_{\text{min}}^*|$, which was in harmony with a diagonal g tensor. Contrary to previous work [21, 32], we do not observe enhanced g factors with values significantly exceeding the values present in bulk InAs.

The experimental data on both states - investigated with different methods - corresponded to the diagonal values of $g_1 \approx 15$, $g_2 \approx 8$, $g_3 \approx 5$, however the directions of the principal axes, i.e. the axes of anisotropy, were quite different. In neither case do these axes conform to the orientation and elongated geometry of our nanowire device, with approximate dimensions of $200 \text{ nm} \times 80 \text{ nm} \times 80 \text{ nm}$. Furthermore, reduced values of $|g^*|$ have been previously found to arise only for sizes below 50 nm, in both experimental [77] and theoretical work [79]. These previous works would imply that the minimal values of $|g_{\text{min}}^*| \approx 5$ thus correspond to sub-20 nm sizes.

The g factor studies in Ref. [144] by Takahashi *et al.*, performed concurrently with our experiments, also found significant anisotropy on self-assembled quantum dots, which did not conform to the symmetries of the pyramidal structure [155]. This is attributed to the effect of the leads which significantly modify the confinement potential. Electrical tuning of the anisotropy further underlined the sensitivity of the anisotropy on the potential landscape.

Taking all these considerations into account, we conclude that the quantum dot embedded in the nanowire is significantly smaller than the dimensions of the device and is mainly defined by mesoscopic details. This also leads to a strong level dependence of the anisotropy.

Anomalous behaviour in Kondo splitting

The splitting of the Kondo resonance does not always follow the expected linear field evolution. For certain orientations, more complex behaviour is encountered, three examples of which are shown in Fig. 5.3. The linear splitting of the Kondo feature acquires an offset of $\Delta B \approx 150$ mT at a field orientation with angles $\theta = 0^\circ$ and φ_{blue} ($g^* \approx 12$), shown in Fig. 5.3.a). Fig. 5.3.b) shows non-linear field dependence, with the slope visibly tailing off above 500 mT, encountered at angles of $\theta = -72^\circ$ and φ_{blue} ($g^* \approx 5.5$). Even more complicated structure was observed at $\theta = 72^\circ$ and φ_{green} ($g^* \approx 5.5$), where the bias sweeps are significantly asymmetric and the Kondo resonance amplitude and width shows non-monotonous variations in B .

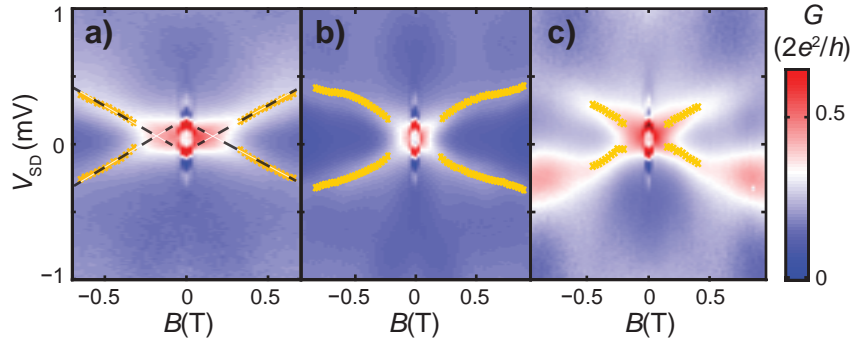


Figure 5.3.: Examples of anomalous field evolution of the split Kondo ridges | a) Onset of splitting occurs at finite field ($\theta = 0^\circ$, φ_{blue}). b) Non-linear field evolution of Kondo peak splitting ($\theta = -72^\circ$, φ_{blue}). c) Asymmetric bias dependence ($\theta = 72^\circ$, φ_{green})

Data on these irregularities is limited and only occurred at seemingly arbitrary positions, with no apparent correlation to the magnitude of the g factor. Thus we are only able to speculate regarding their origins. Theoretical accounts actually predicted a non-zero onset of the Zeeman splitting [167], in contrast to common experimental data [75] where this onset is absent. The direction dependence of this field offset could not be explained.

Anomalous slopes and amplitude variations in Fig. 5.3.b-c) are tentatively assigned to changes in the hybridized Kondo state which accounts for the spin-flip co-tunnelling channel in Coulomb blockade. Low-energy excited states of higher orbitals open inelastic co-tunnelling channels within the Coulomb diamonds, which arise at finite bias. As the Zeeman energy is increased, the conductance from the spin-flip channel would gradually merge with these channels and become indistinguishable from the common co-tunnelling lines.

Furthermore, InAs nanowires are systems where strong spin-orbit coupling plays a major role, and is also responsible for the large g factors. The spin of the Kondo state can also be significantly affected by this interaction. The high anisotropy of the spin-orbit interaction found in both nanowire-based [104] and self-assembled InAs quantum dots [24] might interfere with the spin-flip process, leading to discrepancies compared to our simple picture.

5.2. Summary

The anisotropy of the g factor was investigated in a quantum dot formed on an InAs nanowire. We analyzed the Zeeman splitting and the splitting of a Kondo resonance in an external magnetic field. Both methods reveal an orientation-dependent variation of the quantum dot g factor between 5 and 15. Well-defined principal axes are found for the g -factor tensor, which are not necessarily oriented along the nanowire axis.

6

Quasi-suspended Ferromagnetic Contacts for InAs Nanowire Spin-valve Devices

Nanospintronic devices, created by combining spin-polarized contacts and quantum dots, provide a versatile experimental test bed for the study of spin transport and many spin-related phenomena. Furthermore, the tunable, well-controlled nature of quantum dots could allow an electric means of spin manipulation and controlling spin currents. Thus, such systems show great potential for both applications in spin-based logic, as well as fundamental research of quantum phenomena. Such quantum dots have been created in bottom-up nanoscale systems like carbon nanotubes [15–17, 168, 169] or self-assembled InAs structures [170–172].

Unlike small self-assembled islands, nanowires allow the implementation of multi-terminal devices with complex gate structures [55, 173], making charge pumping [174–176] and spin resonance schemes feasible [25, 32, 153]. The latter - electron dipole spin resonance [153] - is made possible by the strong spin-orbit interaction and large effective g factors in InAs nanowire quantum dots.

Many different semiconducting nanowires have been implemented in conventional diffusive spin-valve structures, with tunnelling magnetoresistance signals found in Ge [177], Si [178–180], and InN [181] nanowire systems. Electrically tunable magnetoresistance features were also found in InP nanowires [182], however these were attributed to the magneto-Coulomb effect. To our knowledge, spin valves created from *InAs nanowire quantum dots* have not yet been reported.

This chapter presents our efforts in creating an InAs nanowire quantum dot spin valve to study the spin physics of the quantum dot with well-defined spin injection and detection, and to test the applicability of ferromagnetic detectors [58, 59] in nanowire-based Cooper pair splitters [30]. We present the details of a novel fabrication process specifically developed for coupling ferromagnets and nanowires. We also report on the characterization of the contacts produced in this new scheme and show some preliminary magneto-transport experiments on the devices.

6.1. Fabrication of quasi-suspended contacts

Permalloy, a $\text{Ni}_{80}\text{Fe}_{20}$ alloy, has been widely used in spintronic devices and has recently been the material of choice in studies of nanospintronic circuits [16, 17]. This is mainly due to the fact that – contrary to cobalt [181] – the magnetocrystalline anisotropy is negligible, hence the dominant shape anisotropy grants a handle on engineering single-domain structures with well-defined magnetic properties.

Controlling the geometry of magnetic thin films and strips is of utmost importance for ferromagnetic materials, especially for materials like Permalloy, where the shape anisotropy is dominant. The formation of helical magnetization becomes more prominent for films with thickness exceeding 50-60 nm. Moreover, any kink along a strip undermines the formation of a single-domain structure. Thus 25-40 nm thick magnetic films are considered ideal.

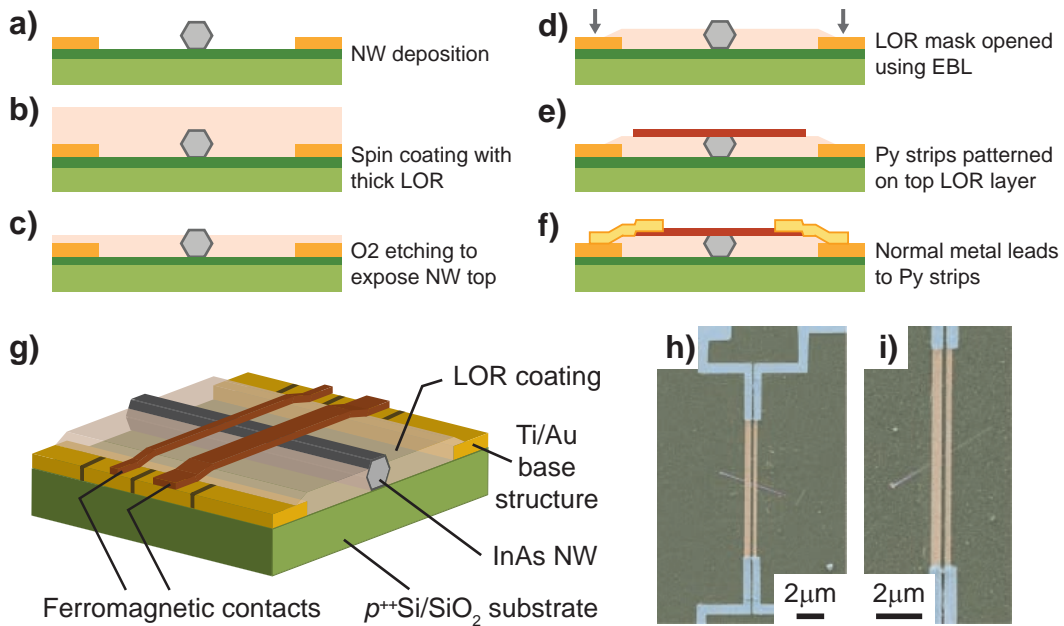


Figure 6.1.: Overview of quasi-suspended contact fabrication on LOR a-f) Step-by-step illustration of the process. g) Illustration of finished device. h-i) False-coloured scanning electron micrographs of finished devices. Note that the nanowire is partially covered by LOR in i).

The relatively large diameter of the nanowire often poses an obstacle when working with thin films. For large height mismatches between the film and nanowire, the shadowing effect or the brittleness of the evaporated material might lead to discontinuities in the film around the nanowire [179, 181]. Thus permalloy strips thinner than 60 nm caused significant problems in achieving contact to the nanowire, without even considering the domain structure.

We developed a new technique to ensure good electrical contact to the nanowire without compromising the magnetic properties of the Permalloy contacts. This is achieved by creating an elevated polymer film platform for ferromagnetic films. The

method was inspired by work on ultraclean graphene samples [183,184], which employed lift-off resist (LOR) [185], a patternable polymer resist as a sacrificial layer. LOR-A (MicroChem) is a polydimethylglutarimide-based organic resist that shows excellent resistance to a wide range of solvents and is stable up to temperatures of 190 °C. This allows us to use conventional electron beam lithography on a second layer of PMMA resist to pattern nanoelectronic circuits on top of the LOR layer.

The developed fabrication process is shown in Fig. 6.1. First, the standard cleaning of wafers with pre-defined base structures and marker grids, and the subsequent nanowire placement (Fig. 6.1.a) is performed. The wafers are then spin-coated with a 1 μm + thick layer of LOR10A (Fig. 6.1.b). Such high thickness was chosen in order to ensure the creation of a flat surface that is not affected by the nanowires. The height of the LOR layer is reduced to 70-80 nm through several iterative steps of slow-rate O₂ plasma etching. After each step, the thickness was measured using a profilometer (KLA Tencor Alpha Step). As a result, the top of the 80-100 nm diameter nanowire becomes exposed (Fig. 6.1.c). Electron beam lithography is used to open windows for the bonding pads and the inner parts of the base structure (Fig. 6.1.d). LOR is exposed using e-beam lithography at 20 keV with a dose of $1100 \frac{\mu\text{C}}{\text{cm}^2}$ and the mask is developed in ethyl-lactate. The dose is gradually decreased at the edges of the inner windows to be able to connect to the base structure without large steps in the LOR thickness.

The ferromagnetic permalloy electrodes and the non-magnetic palladium leads are created in subsequent steps of thermal evaporation on a PMMA mask created via electron beam lithography (Fig. 6.1.e-f). In order to clean the contact area and ensure electrical contact to the nanowire and to the ferromagnetic strips, Ar⁺ ion milling is employed before each evaporation step. Contrary to the usual process, the mask is developed in room temperature xylene and lift-off is performed in xylene at 80 °C, and the sample is rinsed with hexane. Fig. 6.1.g) depicts the design of the finished sample, while Figs. 6.1.h-i) show two examples of scanning electron micrographs of the finished devices.

Shortly following the development of this process, we became aware of analogous techniques devised to tackle similar nanowire-related issues, which achieved quasi-suspended contacts on layers of hydrogen silsesquioxane (HSQ) [181] and S1805 photoresist diluted in 2-methoxy-1-methylethyl acetate (PGMA) [186].

6.2. Magnetic properties

A long (10 μm), thin (25-35 nm) geometry with a small w width is chosen for the Permalloy strips, which serve as ferromagnetic contacts. This morphology forces the magnetization of the ferromagnets to lie along the strip axis. The B_c coercive field of the strips, required to invert the magnetization, is tunable by their width w [16,17]. By choosing the width of the contact electrodes as $w_1 \approx 400$ nm and $w_2 \approx 200$ nm, we ensure appreciable difference in B_c . Thus a field range $B_{c,1} < B < B_{c,2}$ is established where the electrodes support antiparallel alignment.

The magnetic properties and quality of the quasi-suspended permalloy strips were investigated by studying their anisotropic magnetoresistance. The magnetoresistance of single strips was recorded with a high sensitivity resistance bridge for both sweep

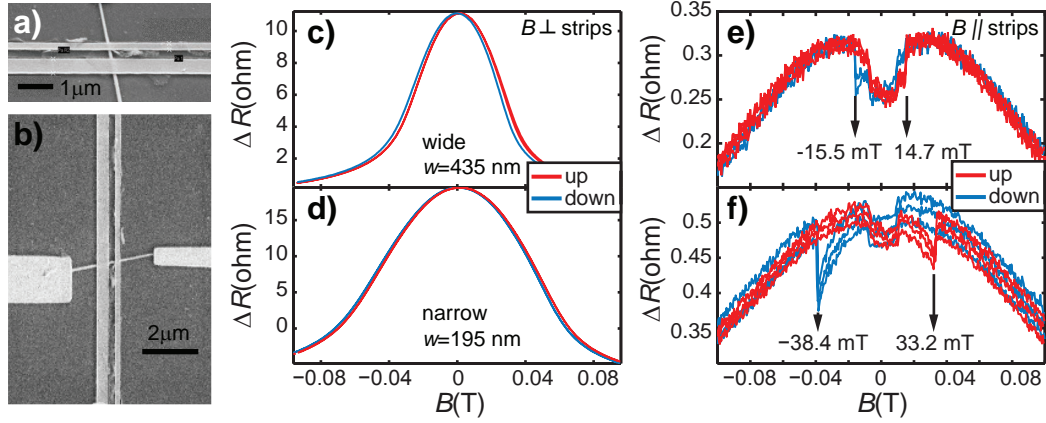


Figure 6.2.: Magnetoresistance of the permalloy strips | a-b) Scanning electron micrographs of the studied devices. c-d) Perpendicular-field magnetoresistance of wide and narrow permalloy strips, respectively. e-f) Parallel-field magnetoresistance of narrow and wide permalloy strips, respectively. Red (blue) curves denote upward (downward) sweep direction.

directions with the magnetic field parallel and perpendicular to their long axis, as depicted in Fig. 6.2.a-b), respectively.

Magnetoresistance in a perpendicular field is plotted in Fig. 6.2.c-d). It exhibits a textbook bell-curve-like field dependence, identical for both sweep directions. Such magnetic field dependence corresponds to a gradual rotation of the magnetization vector with respect to the current. For narrow strips, the resistance decrease takes place on a larger field scale. This is expected, since as the narrower the strips are, the larger the shape anisotropy is, making it more difficult to rotate the magnetization.

A similar background is observed for parallel field sweeps in Fig. 6.2.e-f), smoothly decreasing at higher fields. This is most probably due to an imperfect alignment of the strips and the applied magnetic field. However, unlike the perpendicular field data, a clear hysteresis is present. The resistance reveals a characteristic dip and sudden jump as the magnetic field approached the B_c coercive field. This is a sign of a small rotation in the magnetization, preceding its sign reversal. The coercive fields are extracted from the position of the dips in the MR, as shown in Fig. 6.2.e-f), and correlated to the widths inferred from scanning electron micrographs. The drop in resistance for $|\mathbf{B}| < 10$ mT is an artefact of the superconducting aluminium bond wires.

The observed behaviour fits the theoretical expectations in both field orientations and is highly comparable to previous experiments [16, 17] on strips patterned directly on substrates. The attained coercive field values and corresponding widths are in quantitative agreement with previously reported empirical curves [16, 17]. Furthermore, no further dips were observed in the near-parallel arrangement, signifying that the MR is dominated by a single domain. These findings show that the polymer supporting layer did not compromise the quality or noticeably alter the magnetic properties of the electrodes.

6.3. Electrical contact, quantum dot formation

Now we turn to the electrical characterization of our contacts fabricated with the novel method of quasi-suspension. We also address and investigate quantum dot formation between two contacts.

Several spin-valve devices with quasi-suspended ferromagnetic electrodes were fabricated on 80-100 nm diameter nanowires, with most exhibiting Coulomb blockade. Here, we present two-terminal electrical conductance measurements performed on a single device with a contact separation of 300 nm to assess the quality of our contacts.

The gate dependence of the zero-bias differential conductance is shown in Fig. 6.3.b). As the gate voltage and consequently the electron density in the sample is increased, the conductance also increases. Furthermore, conduction oscillations are found with gradually decreasing magnitude.

To gain better understanding of the underlying processes, the differential conductance of the device is mapped out as a function of both bias and gate voltages in Fig. 6.3.c). At higher gate voltages, a chequerboard pattern is recognizable in the variations of the conductance. Such a pattern is a characteristic feature of Fabry-Pérot oscillations [187, 188], which arise due to coherent reflections at the contacts, creating an electronic cavity. The size of the cavity can be estimated from the ΔE_{cavity} energy spacing of the cavity sub-bands which become available as sufficient bias is applied:

$$L_{cavity} = \frac{\hbar v_F \pi}{\Delta E_{cavity}}. \quad (6.1)$$

The experimentally extracted $\Delta E_{cavity} \approx 2 \text{ meV}$ and the usually assumed $v_F \approx 10^6 \frac{\text{m}}{\text{s}}$ yield a crude estimate of $L_{cavity} \approx 1 \mu\text{m}$. This is about a factor of 2 larger than the actual device length of $L_{device} \approx 450 \text{ nm}$, however the agreement is not satisfactory to comment on the cleanliness of the sample. We attribute this discrepancy to the irregular Fabry-Pérot structure, which is most probably a sum of several components. This is in accordance with the established assumption that 10+ non-ideal, low-transmission sub-bands contribute to the conductance for a nanowire of such diameters [125, 126, 129].

For $V_{BG} < 1.2 \text{ V}$, the conductance exhibits a sharp drop-off from $1.5 e^2/h$ to near-zero values, and a few Coulomb oscillations arise before the conductance is fully suppressed, as seen in Fig. 6.3.e-f). The Coulomb diamonds measured in this low-conductance regime are shown in Fig. 6.3.e) with the borders of the "0" diamond tracked to higher bias values shown in Fig. 6.3.d). As the conductance is suppressed, no further diamonds are visible in Fig. 6.3.d) up to 20 mV bias. We believe that this signifies that the quantum dot is indeed fully depleted and this is not a result of the pinch-off of the contact transparencies.

As the gate voltage is increased, the slopes of the "3" diamond are reduced and the conductance resonances are broadened and become less pronounced. The sudden broadening and subsequent increase in the conductance alludes to an enhancement of the coupling, which should also account for the large change in the device capacitance. Furthermore, this assumption is also corroborated by the emergence of a zero-bias resonance in the "3" diamond, seen in Fig. 6.3.d).

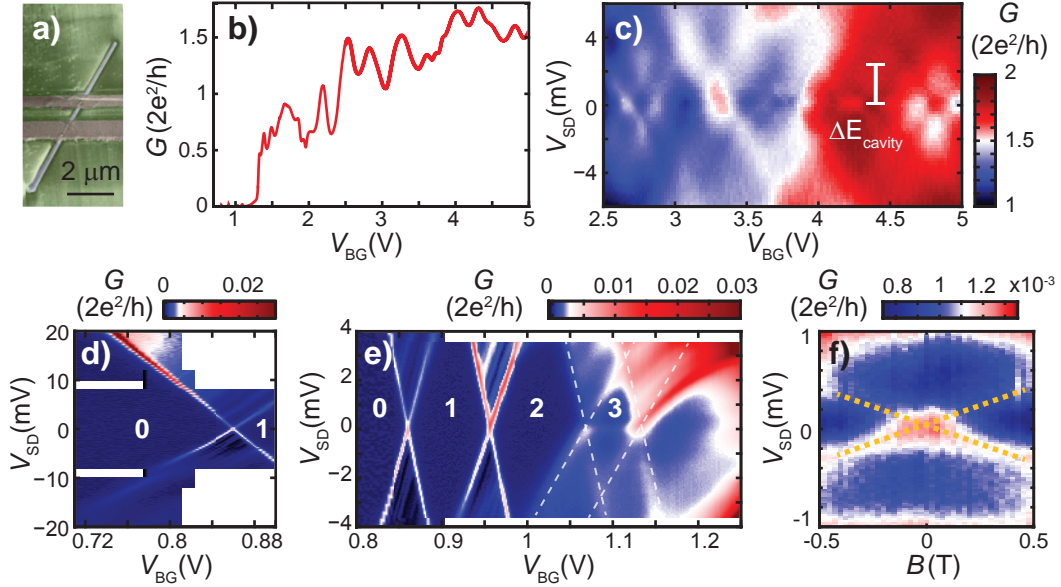


Figure 6.3.: Quantum dot formation between ferromagnetic strips | a) False-coloured scanning electron micrograph of the studied device. b) Zero-bias gate dependence of differential conductance. c) Differential conductance in the open regime as a function of gate and bias voltages. d-e) Differential conductance in the Coulomb blockade regime as a function of gate and bias voltages. f) Magnetic field dependence of the Kondo co-tunnelling lines.

To verify whether this is a Kondo co-tunnelling feature, its magnetic field dependence is measured in the middle of the diamond, shown in Fig. 6.3.f). The splitting of the approximately $400 \mu\text{eV}$ wide zero-bias feature can be observed for $B > 180 \text{ mT}$. The co-tunnelling lines show linear field evolution, symmetric in bias, however, their magnitudes show considerable bias asymmetry. The low conductance of the sample hints at a considerable $\Gamma_1/\Gamma_2 \approx 1500$ asymmetry in the coupling of the quantum dot to the source and drain electrodes, which might account for the asymmetry in the strength of the two co-tunnelling peaks. The effective g factor of 13.6 - extracted from the slopes of these features - amounts to a realistic value for the given device, which underpins our conclusion that the co-tunnelling lines are a result of Kondo correlations at odd occupancy.

Such strong coupling to ferromagnetic contacts will renormalize the spin levels of the quantum dot, which will be split by an exchange energy E_{ex} [189, 190], characterized by the so-called local magnetic exchange field (B_{ex}). We do not observe an exchange field offset with either sign [30]. Although $B_{ex} > 1 \text{ T}$ exchange fields have been observed in many other systems [189, 191–193], the exchange field values found for InAs nanowires were significantly lower, below 100 mT [30]. The large width of the Kondo feature precludes us from determining whether a small exchange is present, or identifying the characteristic gate dependence of the Kondo feature in proximity of ferromagnets [190, 192, 193]. Furthermore, no reproducible features were found in the magnetoconductance of the Coulomb oscillations which could be assigned to an effect

of the ferromagnetic electrodes in this sample. One possible reason for this is that for several samples (including the discussed one) the magnetic properties of the electrodes may have been compromised. It was only later revealed through energy-dispersive X-ray spectroscopy (EDX) that the Permalloy evaporation source used for these samples was likely contaminated.

The Fabry-Pérot features, the broadened resonances accompanied by Kondo tunnelling all point to a strongly coupled device, which attest to the good electrical contact between the nanowire and the quasi-suspended strip.

6.4. Magnetoconductance measurements

The magnetoresistance of several devices was studied in the quantum dot regime and no clear magnetic signal could be identified, even for samples where we were confident about the untarnished nature of the Permalloy films. In many cases, the instability of the device was the main issue prohibiting the observation of magnetic signals.

While spin-valve-like magnetotransport signals were absent in the quantum dot regime, a magnetoresistance signal of not yet understood origin was found in a device which did not exhibit any Coulomb oscillations. The observed magnetoresistances are presented in Fig. 6.4.

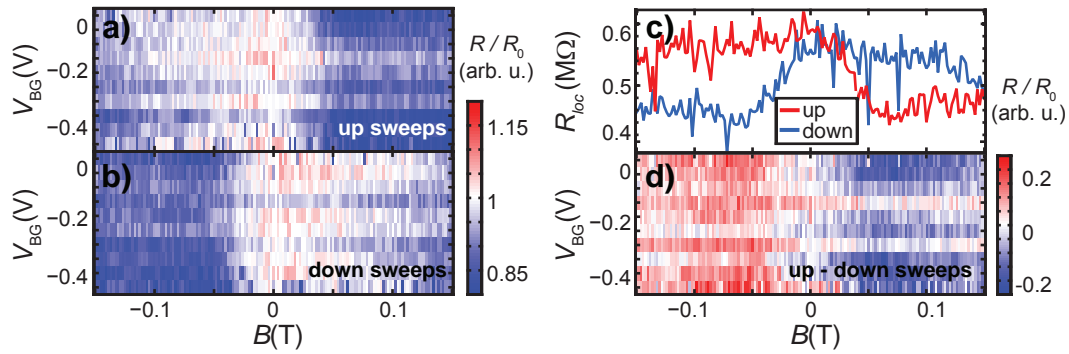


Figure 6.4.: Magnetoconductance of nanowire device | a-b) Gate dependence of magnetoconductance for up and down sweeps, respectively. c) Average magnetoconductance for up and down sweeps, shown in red and blue, respectively. d) Relative difference in magnetoconductance between up and down sweeps.

The magnetic field dependence of the resistance in Fig. 6.4.c) shows variations on a much larger field scale than the coercive fields of the Permalloy strips. The resistance shows weak gate dependence in Fig. 6.4.a-b) and a clear difference is found in the resistance for the two sweep directions, which is further highlighted in Fig. 6.4.d). However, the lack of stability in the given device considerably limited further, more detailed studies.

We regard this as a promising step towards a working device, however multiple issues were faced during the fabrication and measurement of these devices. These problems are summarized in Sec. 6.5.

6.5. Applicability and shortcomings

Our novel procedure successfully circumvented the technical challenge of height mismatch, demonstrating the applicability of the technique. However, it also brought about a new set of fabrication problems which hampered sample quality or simply reduced the number of measurable devices.

The double resist layer made the electron beam lithography process more difficult, with lift-off issues being slightly more common. This could potentially leave behind partial films of undesired ferromagnetic particles which could produce uncontrolled stray fields and magnetic switching, obscuring the magnetic signal. Since multiple resists are involved, reproducible adhesion thickness and etch rates are of paramount importance, hence material ageing and contamination posed great obstacles.

Inhomogeneous layer thickness and inadequate etching occasionally inhibited electrical contact to the nanowires, however this reduced the yield only marginally. The main drop in fabrication yield is attributed to an increased prevalence of electrostatic discharges which destroyed the nanowire or even complete Permalloy strips. The accumulation of static charge is aided by the LOR dielectric, making discharges severe. Furthermore, the presence of the dielectric layer often introduced excess noise or instability, stemming from trapped charges in the polymer layer or residues from the poor lift-off.

6.6. Summary

A novel approach was employed to combine ferromagnets and nanowires. Our approach created quasi-suspended contacts on a thin layer of LOR. We have shown that strong coupling could be achieved to a quantum dot formed between the leads, and that the magnetic properties of the leads were not compromised. Despite these positive signs, we could not yet observe clear spin-valve signals in our devices.

We achieved partial success in implementing our new fabrication method, however its flaws, along with the complicated nature of combining quasi-suspended contacts with the several steps of the Cooper pair splitter fabrication protocol, caused us to change our approach and focus on the implementation of a different scheme [29]. Our ventures into the application of this second scheme are discussed in the following chapters.

7

InAs Nanowire Device with Normal Metal Side Gates

Electric fields generated by side gates have been used recently in InAs nanowire quantum dots defined between as-grown InP barriers to modify orbital energies [194] or to even invert the spin-filling sequence of the structure [195, 196]. Furthermore, side gates could also be used in an ingenious way to tune a double quantum dot system into spin blockade. In this design, two global side gates are used instead of local gates which would require nm-precision lithography [197]. These experiments have shown how such a basic structure could induce significant changes in a quantum dot system and be put to use for a variety of different ways.

The entanglement detection scheme proposed by Braunecker *et al.* [29] is based on locally different spin projection axes as a result of different \mathbf{B}_{SO} spin-orbit fields. We believe that local electric fields, created via side gates in close proximity to the nanowire, could induce an appreciable spin-orbit field, or at least considerably affect the strong Rashba field [138, 139] of semiconducting nanowires to modify the direction of spin-orbit field.

A naïve estimate of spin-orbit energy can be given by calculating the Zeeman splitting induced by the spin-orbit field created by the voltage between the two side gates:

$$E_{\text{SO}} = g^* \mu_{\text{B}} B_{\text{SO}} = g^* \mu_{\text{B}} \frac{v_{\text{F}} |\mathbf{E}_{\text{SG}}|}{c^2}, \quad \text{where} \quad |\mathbf{E}_{\text{SG}}| = \frac{\Delta V_{\text{SG}}}{d_{\text{gap}}}, \quad (7.1)$$

where g^* is the g factor of the electrons in the quantum dot, v_{F} is the Fermi velocity, \mathbf{E}_{SG} is the electric field created by applying V_{SG} voltage between the side gates separated by d_{gap} . This energy amounts to only $E_{\text{SO}} = 0.2 \mu\text{eV}$ for realistic numbers of $\Delta V_{\text{SG}} = 5 \text{ V}$, $d_{\text{gap}} = 160 \text{ nm}$ and the usual InAs parameters of $g^* = 10$, $v_{\text{F}} = 10^6 \frac{\text{m}}{\text{s}}$.

The energy scale of this estimate is orders of magnitude below the values of 0.25 meV measured directly from the excitation spectrum of a single InAs nanowire quantum dot [23], and is also much lower than the 5 μeV energies found for the spin-orbit interaction induced mixing of double quantum dot states [104]. Thus this leads us to believe that the confinement potential and the potential variations in the nanowire have a much stronger effect [139]. These internal fields are probably responsible for the sizeable Rashba-type [143] spin-orbit coupling and is likely behind the anisotropy [24] of the spin-orbit splitting energy and why electric gating can significantly affect it [141].

The crystal fields in the nanowire lead to a Dresselhaus-type spin-orbit interaction [65]. It is usually considered to be negligible in nanowires, as it vanishes in zinc blende structures for electrons with $\mathbf{k} \parallel [111]$ [198], which is the axial growth direction.

Recent calculations have suggested that the Dresselhaus term might have a significant effect on the electron dispersion in wurtzite structures [199, 200]. However, anisotropy measurements [24, 104, 141] yielded an in-plane B_{SO} field and orientation dependence which was in agreement with a Rashba term.

Investigation of the spin-orbit coupling could not be carried out as individual states with well-defined spin-up or spin-down character could not be resolved. Furthermore, the high electron occupancy also hindered examining spin-related phenomena. The strong coupling of the dot to the leads did not allow excited state spectroscopy [23, 24], and neither could orbital Kondo effect [141] be exploited for the determination of the spin-orbit energies. Therefore, the device was used to investigate the effect of side gate electrodes on the Coulomb resonances and the possible tuning of the quantum dot wave function, in a non-magnetic side-gate device.

Here, we present an investigation of the electrostatic tuning of an InAs nanowire quantum dot using side gate electrode. We also examine the effect of the electrostatic environment of the quantum dot on the magnetic field dependence of multiple quantum dot states at different gate configurations.

7.1. Device specifics

Our devices are based on InAs nanowires with 80 nm nominal diameter, which were drop-cast from a NW/IPA suspension on a standard Si/SiO₂ wafer with a pre-defined base structure and marker grid. Locating the nanowires via SEM allowed us to create structures like in Fig. 7.1.b), with a gap of 160 nm between side gates defined within the 350 nm spacing of the source and drain electrodes. The SEM-based location of the nanowires was necessitated by the precision needed to pattern side gates in close proximity to the nanowire, which could not be achieved by locating nanowires through optical means.

Palladium side gates and contact electrodes are created on multiple nanowires using the standard fabrication process with ZEP resist, described in Chapter 4, which ensures high-quality undercut and lift-off. The most promising devices are then selected using SEM imaging. Leads between the base structure and the electrodes of the selected devices are defined in a second lithography and evaporation step to create the complete quantum dot circuit. Evaporation steps are preceded by in-situ Ar⁺ milling in order to remove polymer residues and oxide layers from the nanowire or the metal to ensure good electrical contact.

7.2. Electrical tuning via side gates

The electrical tunability of the device was investigated by mapping the conductance of the device shown in Fig. 7.1.b) as a function of SG1 and the back gate voltage while SG2 was kept at a constant potential¹. We show such a map recorded over an extended range of back and side gate voltages in Fig. 7.1.a). It is evident that a few reversible

¹This was required due to instabilities in the device induced by sweeping the voltage on SG2.

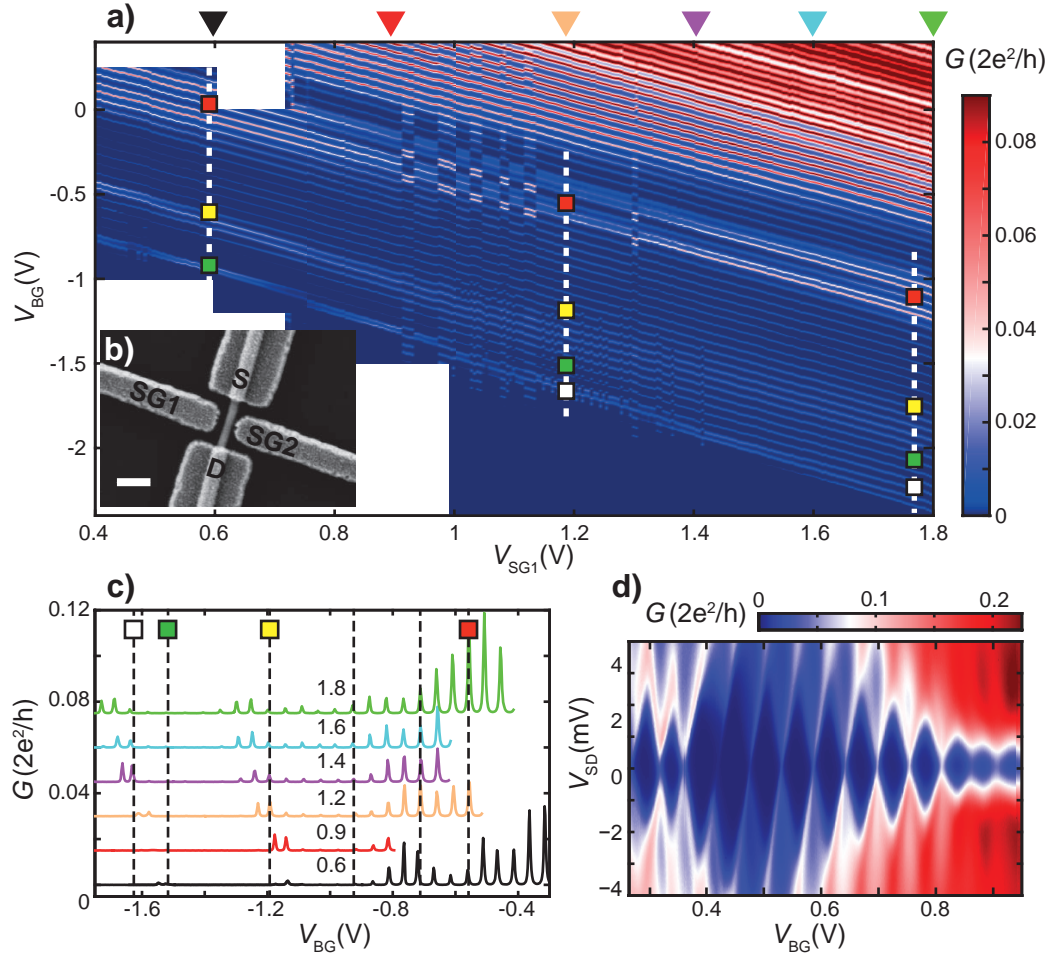


Figure 7.1.: Charge stability of QD device with normal metal side gates a) Conductance as a function of the back gate and SG1 (SG2 is kept at a constant voltage) b) Scanning electron micrograph of side-gate device, scale bar is 250 nm. c) Back gate voltage trace at different side gate voltages. Positions of the plotted curves are marked with triangles of corresponding colors in a). Curves are shifted along the V_{BG} axis to identify the corresponding charge states and offset in conductance for clarity. Selected conductance resonances are marked to aid their identification at different back gate voltages. d) Conductance measured as a function of back gate voltage and bias voltage, showing Coulomb diamonds.

charge rearrangements occur during the extended period of the experiment, we assign these to a bistable trapped charge in close proximity to the quantum dot. While these unfortunately blemish the measurements slightly, they do not cause any irreversible changes.

In order to identify the same charge states as we move along the map, we track the shift of the resonances, induced by the change in the side gate voltage. We extract several back gate traces at different side gate voltages, highlighted by arrows in Fig. 7.1.a). These curves are plotted in Fig. 7.1.c), and shifted along the horizontal axis according to the average slope of the resonances in Fig. 7.1.a), so that the corresponding resonances occur at the same voltages. Some resonances are labelled with squares to aid the identification of charge states and allow the comparison of back gate sweeps at different side gate voltages.

In Fig. 7.1, we observe Coulomb resonances with close to uniform spacing, most of which are shifted equally as V_{SG1} is tuned. This parallel movement is typical behaviour for single quantum dots. We observe some deviations from this in the form of some avoided crossings, visible around the yellow and green labels at $V_{\text{SG1}} = 0.6$ V and white label at $V_{\text{SG1}} = 1.2$ V in Fig. 7.1.a). In Fig. 7.1.c) we can see that the modulation of the resonance amplitudes produces a somewhat periodic envelope, the shape and maximum of which is modified as the side gate voltage and thus the electric field is tuned. For example, the pronounced features labelled with yellow and green squares at $V_{\text{SG1}} = 0.6$ V, are smeared out and shifted to other lower resonances as the voltage is increased to $V_{\text{SG1}} = 1.8$ V.

The resonances show similar widths, which do not show much variation as a function of the side gate voltage and in most cases these variations are smaller than the margin of error. The encountered $|e|\alpha\Delta V \approx 400 \mu\text{eV}$ resonance widths, are significant compared to the $E_C = 3.2$ meV charging energy, inferred from the size of the Coulomb diamonds in Fig. 7.1.d). This indicates strong coupling to the leads.

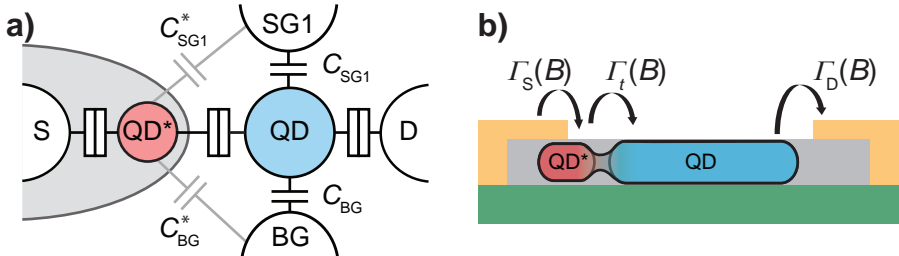


Figure 7.2.: Illustration of possible serial quantum dot, responsible for conductance modulations | a) Equivalent capacitive picture. b) Sketch of device and possible arrangement of QD dots. Transport through QD is modulated by the QD* structure, connected in series.

No underlying structure is observed in the map that would indicate typical double dot system (discussed in Sec. 2.2.6). We assign the avoided crossings to the hybridization of the quantum dot states and the states of a secondary structure, most probably a smaller quantum dot (QD*), which is connected in series. As the size of the Coulomb diamonds in Fig. 7.1.d), and the seemingly negligible δE level spacing points to a large

dot, most probably extending over most of the nanowire between the contacts. We therefore believe that this ancillary structure might form close to the contact area, and is probably somewhat screened by the contact. We illustrate this picture of the system in Fig. 7.2.

This small structure can thus be responsible for modulating the coupling of the main quantum dot to one of the leads and the periodic modulation observed in the resonance amplitudes. The width of the modulation amplitude also points to the strong coupling of the QD* structure to one of the leads. The tuning of the gate voltages could significantly change the envelope function and change resonances which were suppressed at $V_{SG1} = 0.6$ V were made visible at $V_{SG1} = 1.8$ V, which points to the side gates having an effect on the Γ_t coupling of QD and QD*.

7.3. Magnetic field dependence

The magnetic field dependence of the Coulomb resonances was investigated for the same charge states at different side gate voltage configurations, which correspond to electric fields of different magnitudes. In Fig. 7.3, we present the out-of-plane magnetic field evolution of the addition spectrum as a function of the back gate voltage. The three maps correspond to different positions in Fig. 7.1.a), highlighted by dashed lines at side gate voltages of $V_{SG1} = 0.6$ V, $V_{SG1} = 1.2$ V, and $V_{SG1} = 1.8$ V. The examined back gate voltage intervals are shifted so that the potential change induced by the side gate is corrected for and we are able to examine the changes to the same charge states. Squares label the resonances that correspond to the labels used in Fig. 7.1. While it is difficult to identify systematic changes, a multitude of changes are visible which are discussed in the following in a non-exhaustive fashion.

We have seen from the zero-field data that the amplitude modulation of the resonances is clearly modified as the side gate voltage is changed. These pronounced features are also clearly affected by the magnetic field. Most strikingly, in Fig. 7.3, the resonances amplitudes are enhanced around avoided crossings (labelled by yellow and green squares in Fig. 7.3.a), and also exhibit avoided crossings in a magnetic field which affect several resonances on different field scales. As we increase the side gate voltage, these anticrossings occur for other resonances at lower voltages, e.g. the avoided crossing around the green label in Fig. 7.3.a) is shifted to the white label in Fig. 7.3.b), eventually smearing out as the side gate voltage is further increased in Fig. 7.3.b).

Similar characteristics are found for the avoided crossings around the yellow label in Fig. 7.3.a). The features are shifted to resonances at lower back gate voltages and the modulation gradually becomes less pronounced and is spread over more resonances. For the resonances adjacent to the red label, unlike modulation features brought about by the observed avoided crossings, the conductance of several resonances is amplified and leads to more complex behaviour. Here, we find that the spread of the conductance increase reaches over more resonances, as the magnetic field is increased. While difficult to isolate a singular characteristic change, it is evident that the side gate voltage clearly modifies the field evolution characteristics.

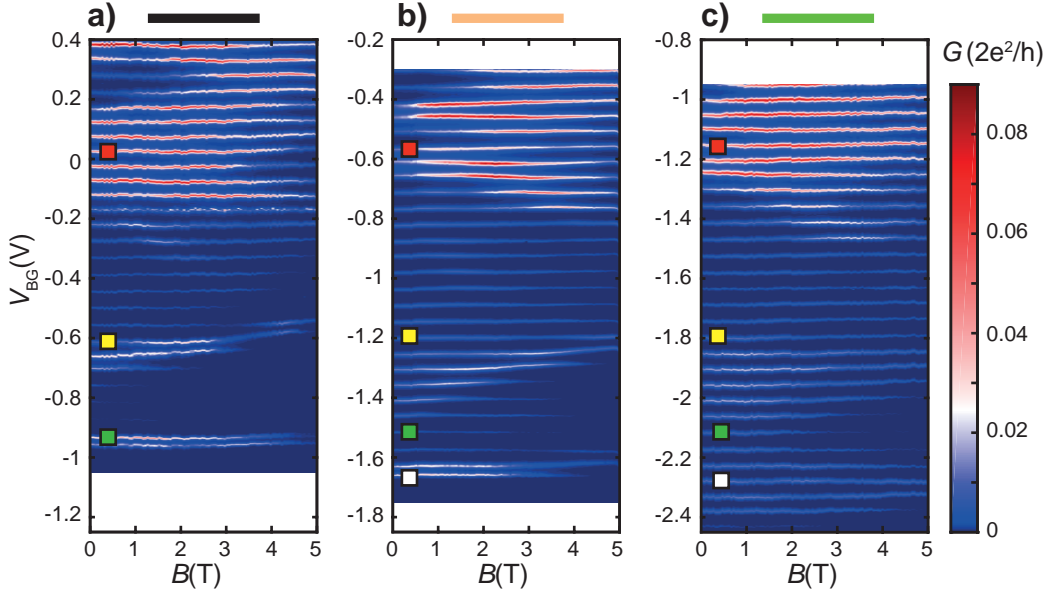


Figure 7.3.: Magnetic field behaviour of QD device with normal metal side gates | a-c) Field evolution of addition spectrum for the same charge states at different gate configurations, highlighted by dashed lines in Fig. 7.1, corresponding to black, orange and green cross sections. Squares serve as a guide for identifying the same resonances.

Interestingly, the resonance positions rarely exhibit any considerable shifts in their magnetic field dependence, except for the series of avoided crossings as a magnetic field is applied. The lack of significant changes in resonance position is contrary to our expectation, based on the large g factors observed in Chapter 5. Based on the near-equidistant peaks, we believe that the level spacing is too small to observe the slopes of the Zeeman shifts, as the charging energy is dominant.

The magnetic field dependence of two further sets of resonances is presented in Fig. 7.4 at two different gate voltages, where we find similar characteristics.

Figs. 7.4.a) and b) illustrate that suppressed resonances at lower V_{BG} voltages can be made visible by changing the side gate voltages. Furthermore, we can observe a change in the occurrence of avoided crossings from ~ 1.8 T to ~ 1 T, marked by yellow triangles.

In Figs. 7.4.c) and d), we once again find avoided crossings when we apply a magnetic field. These features occur for resonances at lower back gate voltages as the voltage between the side gates is increased. In this case, we can also see a change in the slopes of the resonances, possibly due to a change in the relative values of the charging energy and level spacing, allowing the observation of the Zeeman shifts in the spectrum. Due to the apparent change in the level spacing, we cannot determine whether the values of the g factor are tuned. Moreover, the resonances in Figs. 7.4.d) seem to go through avoided crossings at low fields, obscuring the slopes and g factor.

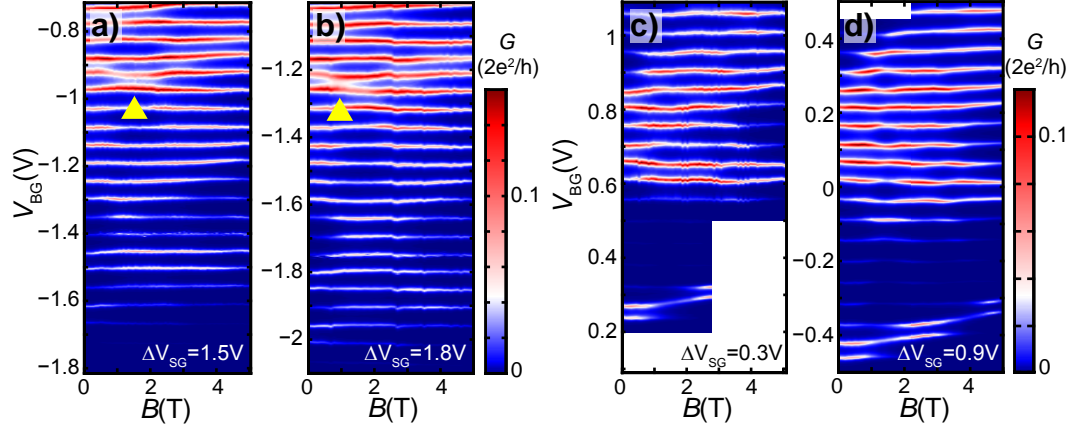


Figure 7.4.: Magnetic field behaviour for two further sets of resonances a-b) & c-d) Field evolution of addition spectrum for two sets of charge states at different gate configurations.

Based on the findings from the magnetic field dependences, we believe that the significant changes in the magnetic field are related to the field evolution of the states which we believe to be hybridized with the states of the quantum dot. This manifests most clearly in the avoided crossings occurring in magnetic field which go hand in hand with the avoided crossings observed in Fig. 7.1 as the side gate is tuned. Thus we attribute the significant variation in the conductance and its variations to the effect of the gate and magnetic field on an ancillary structure.

7.4. Summary

We have investigated the electrical gating of an InAs nanowire quantum dot device. We showed that the gates not only tune the chemical potential quantum dot but also modify the variations encountered in the resonance amplitudes. The electric gating also affects the magnetic field dependence of the quantum dot spectrum.

We attribute the encountered features in the conductance to a smaller unintended quantum dot, connected in series, with which the quantum dot states can hybridize. We find that the side gate voltage and magnetic field dependence of the resonance amplitudes most probably reflect the tuning of the secondary dot and changes in its coupling to the main dot.

8

Magnetic Side Gating of InAs Nanowire

The implementation of many proposed new experiments, for nanowire devices require the application of localized or spatially varying, switchable magnetic fields. Notable examples include:

- fractional fermion generation via synthetic spin-orbit coupling generated by a fast oscillating magnetic field [26–28, 46–48]
- Majorana fermion detection by selective equal spin Andreev reflections [201], implemented by creating a nanowire section with non-zero Zeeman splitting to achieve spin filtering,
- generation of different local spin projection axes for quantum dots along the nanowire to implement an adapted version of recently proposed DC entanglement scheme [29] for Cooper pair splitters [30, 49], as the conventional approach of spin read-out using ferromagnetic contacts is problematic [58, 59]. Furthermore, a locally generated Zeeman splitting could – in principle – be exploited for tunable spin filtering, replacing ferromagnetic contacts, the experimental implementation of which can pose problems in nanostructures (e.g. interface oxidation).

On the ~ 100 -nm length scales of our devices and as required in Ref. [46], this can only be implemented using the stray field of specifically tailored ferromagnetic structures, given that the generated stray field is strong enough to generate an appreciable Zeeman splitting. In this respect, III-V semiconductor nanowires make ideal candidates for the implementation of such schemes due to their large g factors in bulk ($g_{\text{InAs}}^* = -14.7$, $g_{\text{InSb}}^* = -51$ [202]) and similarly large values on quantum dots [21, 34, 152].

In this chapter, a novel approach to control electron spins on single and multiple quantum dots (QDs) is introduced. Our scheme aims to harness local stray fields on nanowire quantum dots created by ferromagnetic side gate (FSG) pairs. Our devices use Permalloy as a ferromagnetic material, owing to the combination of its easily engineerable properties and relatively strong spontaneous magnetization.

Proof-of-principle magnetoresistance (MR) experiments are presented in which we find state-dependent magnetoconductance, where the amplitude, energy and broadening of a quantum dot conductance resonance depend on the magnetic field applied to the device.

8.1. Device specifics

Our devices aim to exploit the locally strong magnetic stray fields created between two nanomagnets. In order to achieve this, we fabricate ferromagnetic side gate strip pairs in close proximity to an InAs nanowire, in which a quantum dot is formed between the non-magnetic contact electrodes. The proposed device geometry is shown in Fig. 8.1.a) and a scanning electron micrograph of the actual studied device is presented in Fig. 8.1.b). This new approach uses ferromagnets in a considerably different manner than spin valves for example. Here, no ferromagnetic contacts are used, which makes the device considerably more robust as possible issues affecting the ferromagnetic contact interfaces are avoided. Also in contrast to spin valves, the tips of the magnetic structures are relevant for our experiments, which are more susceptible to the formation of closure domains [203], which we aim to avoid. As seen in Fig. 8.1.a), the dot is created in the small gap between the magnet pair. This is important as the two magnetizations of the nanomagnets are expected to be coupled due to their close proximity. This creates a close to homogeneous local stray field in the gap separating the strips [40], which is expected to be negligible outside of it. By sweeping the magnetic field through the coercive field, the magnetization of the strips could be reversed in-situ, simultaneously.

Here, we discuss the details of the fabrication process developed to implement this novel design. The devices were prepared using the standard fabrication procedure discussed in Chapter 4. InAs nanowires with an average diameter of 60 nm were dispersed over Si/SiO₂ wafer with a pre-defined Ti/Au base structure and marker grid via drop-casting from a NW/IPA suspension. Nanowire positions were determined through SEM imaging of the chips. Optical dark-field microscopy is generally preferred for locating nanowires, due to its non-invasive nature, however, the accuracy desired for our devices could not be reached. Thus, we turned to scanning electron microscopy for higher resolution. While SEM imaging of devices is usually avoided to minimize the possibility of contaminating the nanowire or inducing defects by electron irradiation, we do not observe any adverse effect of imaging at 1 kV acceleration voltages.

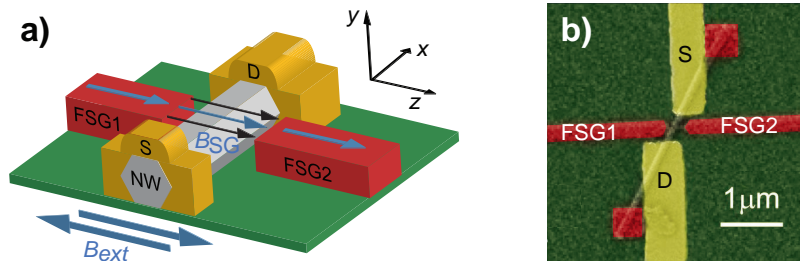


Figure 8.1.: a) Schematic illustration of the studied device, the magnetic field is swept along the long axis of the side gate strips. b) False-coloured scanning electron micrograph of the actual device, where the nanowire is tilted with respect to the axis of the side gates.

First, thin (35-40 nm), narrow Permalloy side gates are patterned in close proximity to the NW. This is achieved with EBL on a 300 nm ZEP resist. Since the nanowires tend to stick to the resist and are thus easily removed during the lift-off process, small patches of Permalloy are deposited at the ends of the nanowires in order to “clamp” them to the substrate. As the native oxide of the nanowires is not removed, these do not form ohmic contact to the device.

The most promising devices are then selected to be contacted by Pd in a subsequent EBL and evaporation step. Prior to the evaporation of the normal metal, in-situ Ar⁺ milling removes the native oxide layer of the nanowires and any oxidation layer that might have formed on the surface of the ferromagnetic clamps. This procedure allowed us to increase the yield of devices with narrow, 150-200 nm wide Permalloy strips within 50-100 nm proximity to the nanowire. Our designs envisage rectangular tips for the strips, however, the electron beam process led to a slight rounding-off of the features seen in Fig. 8.1.b).

In the now presented device, shown in Fig. 8.1.b), the gap between the two gates was around 300 nm, in contrast to the usual values of approx. 150-200 nm, while the approximate $L_{\text{SEM}} = 450$ nm length of the nanowire segment between the contacts was also larger than the ~ 350 nm contact separation. This non-perpendicular alignment also meant that the two gates were slightly offset along the nanowire axis, with SG1 (SG2) lying closer to the drain (source) electrode. Furthermore, SG1 was slightly closer to the nanowire.

Experiments were performed in a ³He cryostat (with a base temperature of $T = 225$ mK), with the externally applicable magnetic field parallel to the ferromagnetic strips.

8.2. Magnetic properties of Permalloy side gate pairs

Permalloy has been extensively studied and employed as the ferromagnetic material of choice for nanostructures due to its dominant shape anisotropy [16, 17, 203]. Signatures of magnetization reversal are easily identified as characteristic dips in the near-parallel AMR measurements. These coercive fields are related to the strip geometry [16, 17], allowing us to define magnetic structures with magnetization reversal fields that suit the experiment by the device design.

The ferromagnetic side gate strips created in the previously introduced fabrication protocol resulted in 150-200 nm wide strips, corresponding to $B_c \approx 30-40$ mT, as determined in previous AMR experiments. As stated before, contrary to ferromagnetic electrodes, the domain structure at the tip of the strips is pivotal in the realization of the desired stray fields. The magnetic properties of ferromagnetic Permalloy strips were examined on test structures produced with the same fabrication recipe (Fig. 8.2.a)). The following studies were undertaken at external institutions. I am immensely grateful to Simon Zihlmann and Péter Makk for including test samples relevant for my studies in their experiments.

Magnetic force microscopy (MFM) – performed in the Hug lab at EMPA – was used to image the stray field created by a single side gate and a side gate pair as well. This instrument allows to probe the spatial distribution of the out-of-plane component of small magnetic fields by measuring the force acting on the magnetic tip of an AFM sensor. Such magnetometry of a side gate pair test sample, shown in Fig. 8.2.a), revealed an out-of-plane magnetic stray field, strongly confined to the gap between the magnets (Fig. 8.2.b). The magnetic field has components with opposite sign at the apexes of the strips, pointing to magnetic field lines which originate at one magnet and terminate on the other magnet with the same magnetization direction. The out-of-plane stray field pattern, measured above the nanomagnet pair, fits our expectation. This leads us to assume that the stray field is localized in the side gate gap and is parallel to the magnetization of the strips.

For comparison, the ends of single magnetic strips, shown in Fig. 8.2.c) exhibit magnetic signals with only one sign, which is consistent with field lines originating at the apex but terminating elsewhere. The bulk of the strips exhibit negligible stray field, indicating a lack of domain walls and single-domain magnetization, typically found for Permalloy [16, 17, 203].

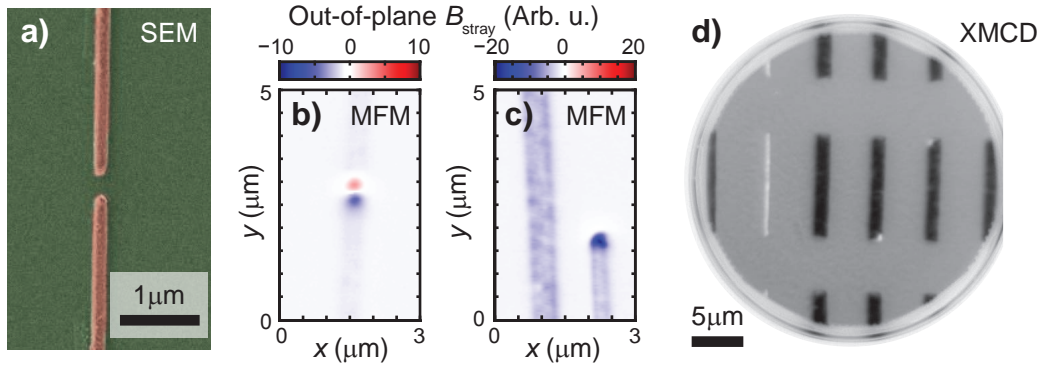


Figure 8.2.: Imaging the stray fields of magnetic side gate strips. | a) Scanning electron micrograph of a ferromagnetic side gate pair. b-c) Magnetic force microscopy of stray fields created by a pair of Py strips and a single Py strip, respectively. d) Domain structure of Py structures measured by X-ray magnetic dichroism imaging of magnetization along the strip axis.

The domain structure of Py strips of varying widths was also characterised via X-ray magnetic circular dichroism (XMCD) studies using the photoemission electron microscope (PEEM) at the SIM beamline at the Paul Scherrer Institut. The detector was configured to be sensitive to the magnetization along the long axis of the strips from the contrast of the reflected X-rays. The homogeneous response in the XMCD data shown in Fig. 8.2.d) also confirms the single-domain structure of the Py strips. Discrepancies are only observed for the two extreme cases: for some strips of $\sim 1 \mu\text{m}$, small imperfections were present in the corners, indicating possible closure domains; similarly for the narrowest strips ($w \approx 120 \text{ nm}$), where multiple domains are visible. Since the strips were not magnetized prior to the measurement, this is not surprising,

especially since with decreasing width, these magnets become magnetically “harder”. Surface corrugation, imperfect edges and contaminants can also lead to the pinning of domain walls.

No such issues arise for strips around 200 nm wide, which is the characteristic dimension for the magnets of actual devices. This allows us to assume that no closure domains form at the ends of the employed nanomagnets.

8.3. Zero-field conductance characteristics

We begin our investigation of the device by examining the electronic transport features in zero external magnetic field. The differential conductance of the device is mapped out as a function of the voltages applied to the two side gates, as seen in Fig. 8.3.a). We observe Coulomb blockade resonances tuned by both side gates. The map reveals more structure than the parallel lines of constant intensity expected from a simple single-dot picture within the constant interaction model. Furthermore, the resonance amplitudes and widths show periodic modulation, indicating a more elaborate structure than an ideal single quantum dot.

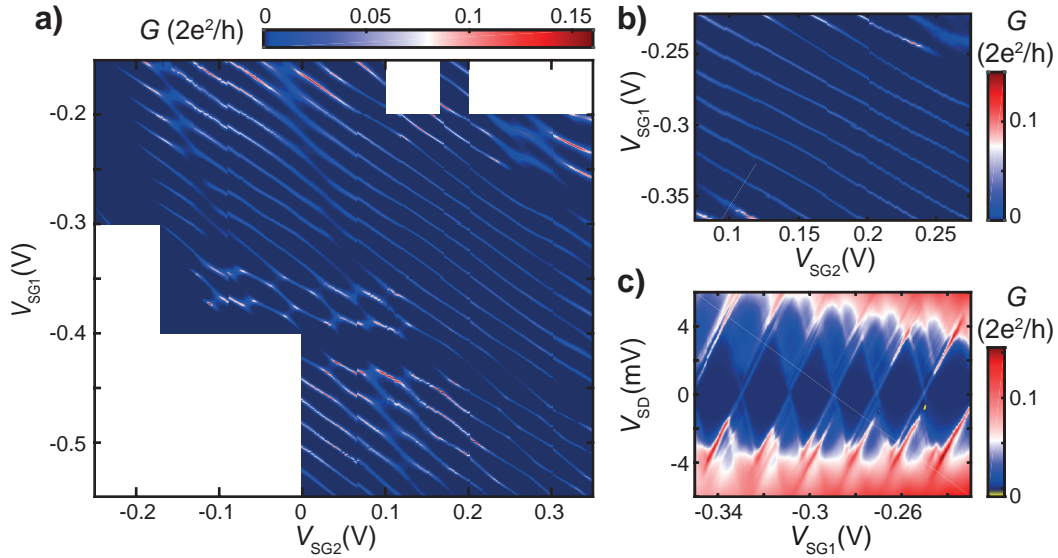


Figure 8.3.: Electrical gating of NW device | a) Conductance maps as a function of the two side gate voltages at $V_{BG} = -0.9$ V. b) Region of map at $V_{BG} = -0.9$ V with single-dot-like behaviour. c) Coulomb diamonds measured in the single-dot regime.

We are able to access gate regions with different conductance features. We investigate the three different regimes, exhibiting unique features in their corresponding conductance maps. We extract capacitances for all electrodes in order to gain a qualitative picture of the device.

Single-dot regime

Firstly, regions of parallel lines with only slight variations in conductance are found at certain gate configurations, as seen in Fig. 8.3.b). We believe that these features stem from a single quantum dot with its wave function extended over most of the device length. Thus we will refer to it as the *single-dot regime*.

The charging energy $E_C = \frac{e^2}{C_\Sigma} \approx 3.5$ meV measured from the size of the Coulomb diamonds in Fig. 8.3.c) yields a total capacitance of $C_\Sigma \approx 46$ aF. Minimal variations are found in the spacing of the resonances, from which we conclude that the δE level spacing is much smaller than the E_C which is expected from a system with relatively large dimensions and high electron occupancy. Due to the increased number of gates, and the fact that the device capacitance is dominated by the source and drain electrodes, the usual methods of estimating the device length from the C_Σ total capacitance are not applicable. Numerical simulations of the electrostatic environment of the exact design would be required to extract the quantum dot size, however this was not important enough to warrant such calculations. In Fig. 8.3.c), the lines of the excited state spectrum of the dot are very tightly spaced as zero-conductance valleys are difficult to find, indicating a small excited energy scale, in accordance with the large size of the dot.

We proceed by examining the capacitive coupling of each gate to gain some qualitative insight into the spatial distribution of the electrons and quantum dot geometry in the studied device. The capacitances of all gates are extracted from the e/C_i peak spacings, while the Coulomb diamonds allow us to find the lever arms of the leads. All capacitances and lever arms can thus be determined. For the single-dot regime, these values are summarized in Table 8.1, where the directly measured values are marked in bold.

Table 8.1.: Capacitances (C) and lever arms (α) in the single-dot regime.

	SG1	SG2	BG	S	Residual	Σ
C (aF)	8.13	4.12	3.80	14.84	15.3	46.2
α	0.178	0.090	0.083	0.320	0.330	1

From the spacing of the peaks in Fig. 8.3.b), we find $C_{\text{SG1}} \approx 2C_{\text{SG2}}$ for the two side gates. This asymmetry in capacitances is in accordance with SG1 being closer to the nanowire, as seen in the SEM image in Fig. 8.1.b). The back gate capacitance of $C_{\text{BG}} = 3.8$ aF is extracted in a similar manner from back gate sweeps. The lever arm of SG1 is obtained from the slopes of the Coulomb diamonds using Eq. (2.18), while the other lever arms are calculated using the extracted capacitances. The slopes of the Coulomb diamonds also allow us to determine the lever arm of the source electrode as $\alpha_S = 0.325$. The residual capacitance of $C_{\text{res}} = C_\Sigma - C_S - C_{\text{BG}} - C_{\text{SG1}} - C_{\text{SG2}}$ thus amounts to $\alpha_{\text{res}} = C_{\text{res}}/C_\Sigma = 0.33$ of the total capacitances and is probably dominated by the drain electrode.

Strongly coupled double-dot regime

By only slight changes to the gate configuration of the device and thus its potential landscape, our measurements revealed a honeycomb-like pattern of resonances (Fig. 8.3.a). This structure is the characteristic fingerprint of double quantum dots. A detailed map of such a region is shown in Fig. 8.4.a) in detail. Here, the conductance is maximal around the triple points, where both dots are near-resonant. For two tunnel-coupled quantum dots, electron transport through the system would only be allowed on the triple points, since if only one of the QDs has a level aligned with its corresponding lead, electrons may tunnel on and off this dot on one side but there is no net current through the system. In our case, the conductance is significantly suppressed as we move away from the triple point, however it does not vanish. This leads us to conclude that these two dots are strongly coupled, allowing current even when one dot is off-resonance, hence we refer to this region as the *strongly coupled double-dot regime*. Since the gate configuration is changed only slightly, a significant spatial separation of the electron density and thus weakly coupled dots would not be expected.

For simplicity, we shall address these molecular states of the strongly coupled double dot in the usual double-dot formalism, as seen in Fig. 8.4.c) with the notations of QD^L and QD^R for the molecular state wave functions with a larger weight on the left and right side of the device, respectively.

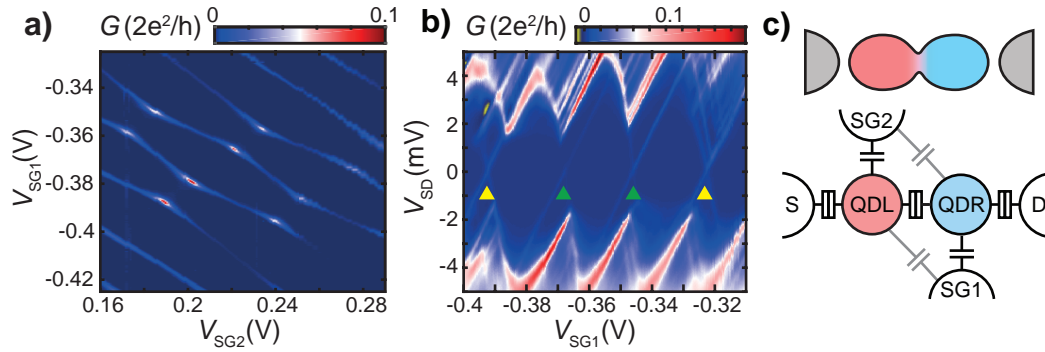


Figure 8.4.: Strongly coupled double-dot regime | a) Charge stability diagram as a function of the two side gate voltages at $V_{BG} = -0.9$ V. b) Coulomb diamonds as a function of V_{SG1} and V_{SD} bias voltage. c) Simplified picture of the system in the framework of a double quantum dot illustrating capacitive couplings.

The maps of the honeycomb regions like in Fig. 8.4.a) are evaluated to gain a qualitative description of the system. The resonances of different slopes are assigned to different QDs. This assumption is also supported by the fact that resonances of different slopes possess slightly ($\sim 15\%$) different widths, indicating a difference in the gate lever arms.

Lines with smaller slopes ($m_1 = -C_{SG2}/C_{SG1} = -0.4$) are more strongly tuned by SG1, which is slightly closer to the drain electrode. While the steeper resonance with $m_2 = -0.75$ are also mainly tuned by SG1, the effect of SG2 is considerably stronger than for the former lines. Thus we believe that the lines with m_1 belong to QD^R and the latter belong to QD^L , as shown in Fig. 8.4.c).

The capacitances and lever arms of both sets of resonances are given in Table 8.2 in order to characterize our system. Once again, directly obtained values are given in bold typeface.

Table 8.2.: Capacitances and lever arms to strongly coupled double-dot system.

	SG1	SG2	BG	S	Residual
C^L (aF)	5.42	4.04	3.59	8.02	7.11
C^R (aF)	7.09	2.87	3.45	7.09	12.30
α^L (aF)	0.192	0.143	0.127	0.286	0.252
α^R (aF)	0.215	0.087	0.105	0.220	0.373

By analysing Fig. 8.4.a) as described in Sec. 2.2.6, the capacitances of both side gates are determined for each QD. The lever arms of SG1 to both QDs were inferred from the slopes of the Coulomb diamonds in Fig. 8.4.b), where the two outer (yellow triangles) and two inner (green triangles) resonances belong to the lines which we attribute to QD^L and QD^R , respectively. The lever arms are slightly higher than in the single dot case, namely $\alpha_{SG1}^L = 0.192$ and $\alpha_{SG1}^R = 0.215$. This $\sim 10\%$ difference is in accordance with the $\sim 10\text{-}15\%$ wider resonances, assigned to QD^L . The slopes of the Coulomb diamonds also reveal that the capacitance of the source electrode is reduced compared to the single-dot regime. Furthermore, we find $C^L > C^R$, which fits our assumptions regarding the geometry of the double-dot molecule, with QD^L (QD^R) being closer to the source (drain) electrode.

Although it is more difficult to evaluate in the double-dot regime, no significant changes are observed in the charging energies of the coulomb diamonds in Fig. 8.4.b), possibly a small increase to $E_C \approx 3.8$ meV, however this cannot be confirmed without a shadow of a doubt. As the charging energy is only minimally affected, C_Σ does not change either, i.e. the whole quantum dot molecule is charged, not just its smaller constituents.

Weakly coupled double-dot regime

Tuning the back gate voltage from $V_{BG} = -0.9$ V to a more negative value of $V_{BG} = -1.6$ V modifies the intensity modulation of the peaks, shown in Fig. 8.5. Close to the pinch-off of the device conductance, the conductance was significantly suppressed with the exception of certain lines of amplification which was enough to produce very low conductance Coulomb resonances ($G_{\max} < 10^{-3} \times \frac{2e^2}{h}$). This pattern is believed to arise from a more weakly coupled double-dot system, where transport is only possible along the avoided crossings around the triple point. This is possible if the charging of the system follows a strongly skewed honeycomb pattern, like the one illustrated in the sketch in Fig. 8.4.b). As a result we are only able to observe conductances along certain lines in Fig. 8.4.c), which are, in fact, a series of avoided crossings. We refer to this region as the *weakly coupled double-dot regime*.

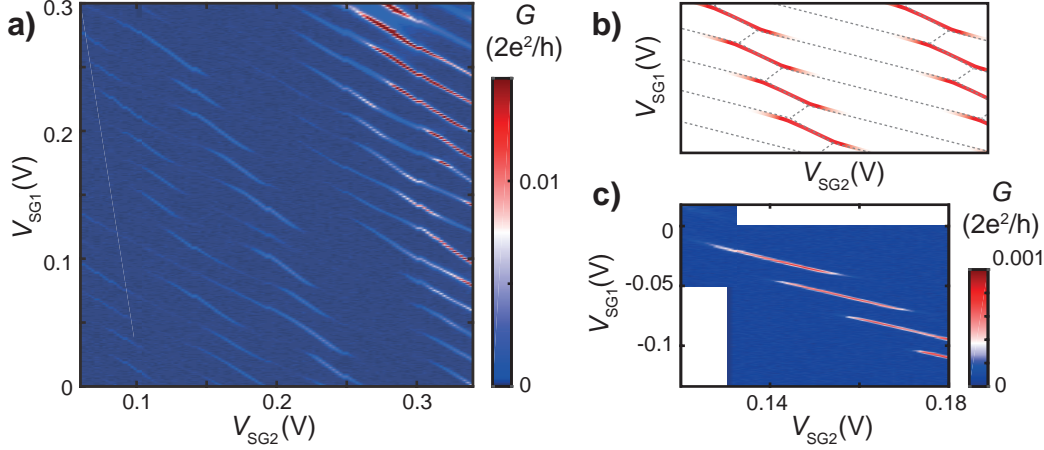


Figure 8.5.: Electrical gating of NW device in the weakly coupled double-dot regime | a) Charge stability diagram as a function of the two side gate voltages at $V_{BG} = -1.6$ V, close to pinch-off. b) Sketch of skewed honeycomb pattern, with conductance present near triple points. c) Series of resonances close to pinch-off at $V_{BG} = -1.6$ V, where conductance suppression is prominent.

The capacitances of all gates are extracted in a similar fashion as previously and the values are collected in Table 8.3. As the conductance is quenched away from the triple point, no full Coulomb diamonds could be recorded, we only observe highly irregular Coulomb diamond fragments, probably belonging to different quantum dots. Consequently, the charging energies and lever arms of the system could not be inferred in a reliable manner.

Table 8.3.: Capacitances to the weakly coupled double-dot system in low-density region.

	SG1	SG2	BG
C^L (aF)	9.22	3.76	3.23
C^R (aF)	8.00	3.62	4.07

The suppressed conductance and the large difference in the spacing of the peaks increase the error of our evaluation, however these numbers still allow us to qualitatively determine the relative position of the quantum dots along the wire. Compared to the previously discussed regions, we observe a much larger asymmetry in capacitances, which is consistent with electrons being confined in the region of the nanowire close to SG1, as it has a much stronger effect on these resonances.

At the lower back gate voltages, the average charge carrier density along the nanowire is reduced, mesoscopic variations of the potential within the nanowire are more likely to induce charge puddles and spurious barriers. Such variations can be a result of charges trapped in the native oxide layer of the nanowire or capping oxide of the wafer. Stacking faults along the nanowire have long been believed to be responsible for the formation of unwanted quantum dots [119], however a recent study found surface

potential fluctuations to be a more probable cause [204,205], especially since it is argued that electronic transport takes place mainly near the surface.

8.4. Overview of magnetotransport features

We now investigate the conductance of the device as a function of an external magnetic field, applied along the side gate axis. For this, we record gate voltage sweeps of the resonances, while sweeping the magnetic field parallel to the magnetic side gates. This is also the expected orientation of the stray field present on the nanowire. In the simplest picture of our experiments, we expect to observe the intrinsic $G(B)$ magnetoconductance of the nanowire quantum dot, where the stray field is expected to enter as a constant offset in $G(B \pm B_{\text{stray}})$, the sign of which is determined by the magnetization of the nanomagnet. The hysteresis of the magnetization is thus expected to be reflected in the magnetoconductance as abrupt changes at the coercive field.

Here, we will give a general overview of the most commonly encountered, typical magnetoresistance characteristics, irrespective of the transport regime. Regime-specific magnetoconductance features and gate-tunability are discussed in Sec. 8.5.

We acquire conductance maps as a function of one gate voltage (while other voltages are kept constant) and the magnetic field for both sweep directions. A typical pair of up/down sweeps is shown in Figs. 8.6.a-b). Individual gate traces, measured at different fields, are evaluated by extracting the resonance parameters from each gate trace: maximum conductance (G_{max}), width (ΔV_{SG1}), and peak position in gate voltage ($V_{\text{SG1}}^{\text{res}}$) (Fig. 8.6.c). The field dependence of the three characteristic parameters is plotted in Figs. 8.6.d-f).

As the external magnetic field is swept through the coercive field of the strips, their magnetization is reversed. Accordingly, the sign of the stray field on the device is also inverted, leading to a discontinuity in the magnetic field dependence of the QD transport properties. In our experiments, abrupt changes in the magnetoconductance were only visible at $B_c = \pm 35$ mT, in good agreement with the expected coercive field of a 200 nm wide Py strip [16, 17].

Since no further switching features are encountered, magnetization reversal is believed to occur simultaneously for both sides of the ferromagnet side gate pair. Based on this single switch, we assume that the magnetization forms a single domain in each gate, or at least in the region which affects the nanowire. However, smooth changes can still occur as a result of stray fields created by minuscule closure domains in close proximity of the QD device.

The curves presented in Fig. 8.6 represent a typical example of the encountered magnetoconductance behaviour. The magnetic field dependence of the amplitude – corresponding to the maximum conductance (Fig. 8.6.d) – is well approximated by a quadratic function. The $G_{\text{max}}(G) \propto B^2$ dependence is clearly present up to fields of ~ 500 mT (not shown). Taking this into account, the hysteretic low-field B dependence can be interpreted as a result of a constant stray field offset along the B axis, i.e. the encountered field dependence is either $G(B + B_{\text{stray}})$ or $G(B - B_{\text{stray}})$, depending on the magnetization direction of the gates. The strips reverse their magnetization as the applied magnetic field is swept through B_c , which is seen as a jump between the two

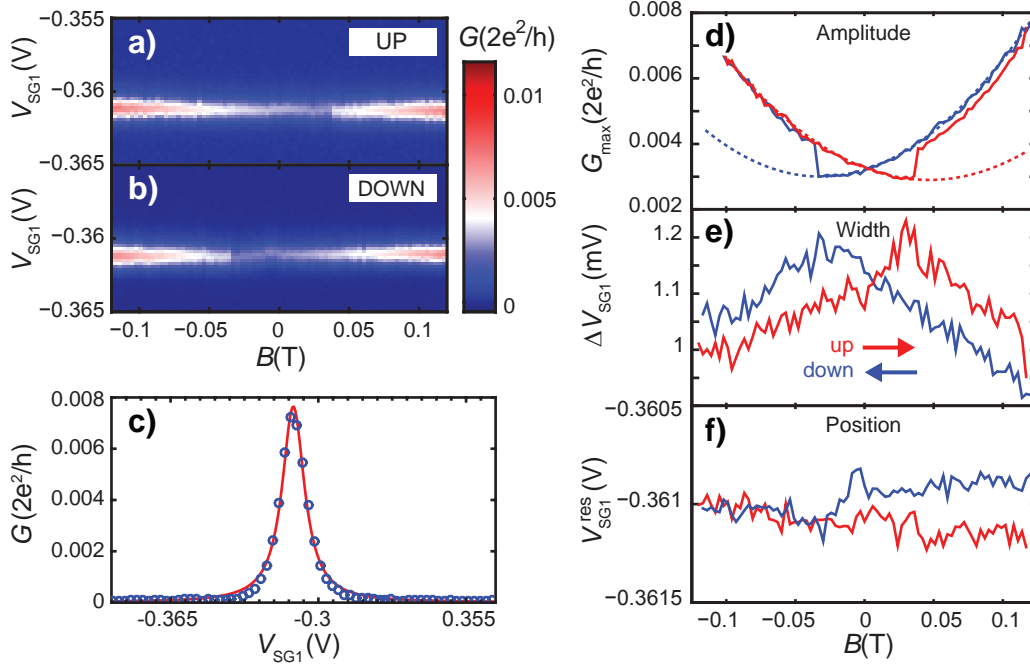


Figure 8.6.: Typical magnetoconductance of a Coulomb resonance | a-b) Conductance maps of a Coulomb resonance as a function of one side gate voltage and the magnetic field for both sweep directions. c) A typical resonance trace at a constant magnetic field with a Lorentzian fit. d-f) Magnetic field dependence of resonance amplitude, width and position, respectively. Parameters extracted by fitting Lorentzian curves to gate traces of the map.

shifted parabolas. Thus by fitting the low-field data with parabolic curves, an estimate of $B_{\text{stray}} = 45\text{-}50\text{ mT}$ can be given for the stray field from the offset in the apexes of the fitted parabolas. The fitted curves are plotted as dashed lines in Fig. 8.6.d), the apexes of which correspond to the external field compensating the stray field.

A clearly hysteretic magnetic field dependence is found for the resonance width, exhibiting maximal values around the coercive field. However, no abrupt changes are observed like in the amplitude, the width shows differences for the two sweeps on field scales much higher than the coercive field. While some shifts are observed in the resonance position, no abrupt changes can be observed. This is in accordance with Zeeman energies smaller than the resonance broadening.

We carry out this measurement and evaluation protocol on a large range of resonances, exploring the magnetoconductance features in all significantly different regimes, found in Sec. 8.3.

In the following, we discuss the field dependence of the resonance parameters for four resonances exhibiting typical magnetoconductances found in Fig. 8.7.

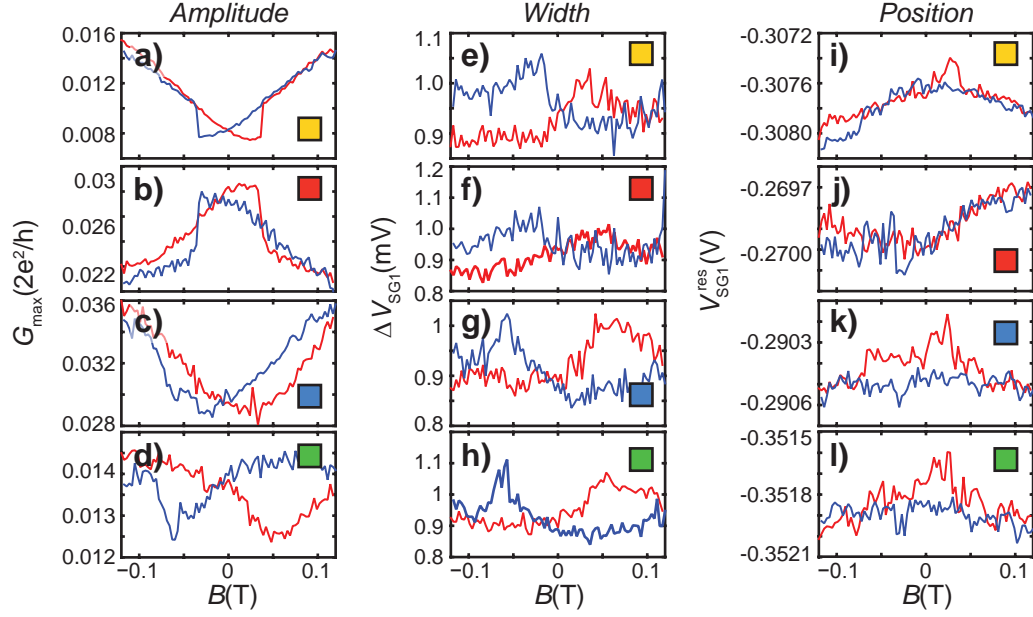


Figure 8.7.: Overview of magnetoconductance features | a-d) Amplitude, e-h) width and i-l) resonance position of four different resonances, illustrating typical magnetic field dependences. Coloured squares serve as labels for the identification of the resonances.

Amplitude

Of the three parameters, the conductance maximum exhibits the most prominent changes in magnetic field, in which a signature of magnetization reversal can be observed. While the quadratic field dependence presented in Figs. 8.6 and 8.7.a) is quite common, many other types of field dependence are also observed, as shown in Figs. 8.7.b-d). We see a similar field offset and sharp switching for the bell-curve-like dependence in Fig. 8.7.b). Figs. 8.7.a-b) give a representative picture of the most typical magnetic field dependences, observed in $\sim 60\%$ of all cases. In this simple picture, the field evolution of the conductance should follow the same curve above the coercive fields, irrespective of the sweep direction.

For many resonances, however, the observed behaviour could not be explained by an offset in the magnetic field, that is reversed at the coercive field of the magnet. Such examples are shown in Figs. 8.7.c-d), where no sharp changes are observed at the coercive field, instead we observe a hysteretic dip in the conductance on a slightly larger field scale. These smooth variations are visible up to a field of > 100 mT, much higher than the coercive field. At these high fields, the conductance curves for the two sweep directions converge to a common curve, as we would have expected.

Width

The resonance width, contrary to the amplitude, shows qualitatively similar behaviour for all resonances, regardless of the absolute values of the conductance or the nature of its magnetic field dependence.

The widths encountered for most resonances correspond to an energy broadening of 150-200 μeV , which is not much larger than the $3.53 k_{\text{B}}T \approx 67 \mu\text{eV}$ energy scale of thermal broadening, calculated for the base temperature of $T_{\text{base}} = 225 \text{ mK}$. This means that we are in an intermediate regime where the width is determined by both the lifetime broadening and the temperature.

The widths of the four resonances examined in Fig. 8.7 show qualitatively the same hysteretic variations in their magnetic field dependence, as plotted in Figs. 8.7.e-h). In all cases, the resonances exhibit an onset of broadening as the magnetic field is swept through zero field. The widths exhibit maximal values between 30-70 mT, close to the coercive field of the strips. The widths are eventually narrowed to the initial values on much larger field scales as B_c . The relative changes in width amount to $\sim 10\%$. This broadening of the resonances seems to be related to the dips encountered in the magnetoconductance, as amplitude changes occur on the same field scales.

We speculate that the stray field generated by the nanomagnets along the nanowire might be inhomogeneous in both its magnitude and direction, especially in the regions outside of the side . As the magnetic field is swept, the distribution of the local magnetic field can thus go through considerable changes, which would happen on similar field scales as the coercive and the created stray field. We will return to the discussion of field inhomogeneities in Sec. 8.6.2.

Closure domains might switch their magnetization at different fields as the rest of the strip, or just exhibit a smooth rotation of their magnetization. Such changes might also affect the width in a hysteretic manner on field scales larger than B_c . However, such broadening was also observed in other devices, both with Permalloy and cobalt side gates (see Sec. 8.7), seemingly a trademark of such ferromagnetic side gates.

One can also argue that the broadening is of thermal origins, as sweeping the magnetic field creates eddy currents which creates heat load on the system. While this is a typical issue which might arise at large sweep rates, in the case of the presented experiments, the employed sweep rates were very low, below $100 \frac{\text{mT}}{\text{min}}$. Furthermore, such eddy currents would mainly affect the thermally more conductive metallic structures, which are in good thermal contact with the cold finger, thus the heat would not be dissipated on the quantum dot, and could not amount to a 20-25 mK change in temperature corresponding to the broadening of 10%. Nevertheless, in measurements where the smaller resolution in the applied magnetic field does slightly increase the effective sweep rate, the changes in the width were around 20%, in contrast to the 10% variations found in the higher resolution experiments shown so far. We believe that this has more to do with the dynamics of the magnetic structures than a possible heating of the quantum dot.

Position

The final parameter of interest is the resonance position. In fact, for a single quantum dot with \mathbf{B} -independent wave functions, this is the only property that is directly affected by the Zeeman term in the energy spectrum of the dot.

The measurements rarely show significant shifts or jumps around the coercive field, in most cases these could easily be masked by the noise, as it can be seen in Figs. 8.7.i-l). The energy scale of the Zeeman splitting (with a $|g_{\text{InAs}}^*| = 14.7$) on these low field scales is below $60 \mu\text{eV}$, i.e. considerably smaller than the extracted resonance widths. Hence the difficulty in the observation of such sudden changes or shifts fits our considerations of the energy scales.

For the cases where any sudden change in the resonance position is observed around B_c , it affects all resonances in a uniform manner. Figs. 8.7.k) and l) present the magnetic field dependence of the position of two resonances measured simultaneously. Despite the noise, the correlations in the positions are clearly visible, showing that the position of all resonances was affected. These jumps are often not reproducible in consecutive sweeps. The origin of this may lie in the magneto-Coulomb effect, which is a result of an effective gating action of the ferromagnet as the magnetic field is swept, as discussed in Sec. 2.2.5. Using Eq. (2.29), we estimate that the two side gates can maximally induce an abrupt change of

$$\Delta V_c^{\text{MC}} = \frac{1}{e} \frac{C_{\text{SG1}} + C_{\text{SG2}}}{C_{\text{SG1}}} P g_{\text{Py}} \mu_{\text{B}} B_c \approx 40 \mu\text{V}, \quad (8.1)$$

in the gate voltage of the resonance at the coercive field, where we assumed extreme values of $P = 0.8$, $g_{\text{Py}} = 2.1$, and the capacitances in Table 8.1. Such small values seem minute but observable on the field scales presented in Figs. 8.7.i-l). Distant charge traps may also weakly affect the QD and shift the resonances slightly, without systematic re-occurrences.

We have shown the typical magnetoconductance behaviour encountered in Coulomb blockade resonances. We find major differences in the magnetic field dependence of the amplitude between the four typical resonances. In contrast, the resonance width and position show qualitatively identical behaviour for all resonances. From here on, we therefore restrict our discussion to the examination of the changes in the resonance amplitude, unless otherwise noted. We now turn our attention to how the magnetoconductance is affected by changes in the electrostatic potential landscape, which also modify the transport properties of the device.

8.5. Magnetoconductance in different regimes

The magnetoconductance of several different characteristic resonances has been studied and compared so far, without considering the specifics of transport regimes. In the following, we investigate the systematics in the magnetoconductances found in the different transport regimes, and also examine the effect of electrostatic gating on the magnetoconductance. As stated previously, we focus exclusively on the conductance maxima from here on, and only discuss the other two parameters if anomalous behaviour is observed.

8.5.1. Single-dot regime

We first focus on resonances in the single-dot regime to evaluate the magnetoconductance at different gate voltages. In this regime, the spacing of the resonances remains nearly unmodified as the voltage on SG2 is tuned, i.e. a series of parallel lines can be seen in Fig. 8.8.a). The behaviour of five resonances is studied at three values of V_{SG2} , marked by dashed lines and triangular labels in Fig. 8.8.a), while individual resonances are identified by circles for straightforward identification.

We observe only slight changes in the zero-field conductance as the voltage on the second side gate is altered. The Coulomb diamonds in the charge stability diagrams in Figs. 8.8.b-c) are also quite similar, and both show a rich excited state structure with many conductance channels available at finite bias. However, some of the more prominent features in the excited state spectrum, indicated by yellow arrows, are noticeably shifted.

The magnetic field dependence of the amplitudes for the studied five resonances at the three gate configurations is summarized in Figs. 8.8.d-f). The three columns correspond to SG2 voltages of $V_{SG2} = 130$ mV, $V_{SG2} = 150$ mV, and $V_{SG2} = 170$ mV, respectively. These resonances show a large variety of magnetoresistive behaviour, as distinctively different types of magnetoconductance signatures (as seen previously in Figs. 8.7.a-d) can be observed by examining single resonances at different gate voltage configurations. Despite no large variation in the conductance at zero magnetic field, the magnetoconductance of these resonances is profoundly modified by these small changes to V_{SG2} . Probably the most remarkable observation in Figs. 8.8.d-f) is that a voltage difference of $\Delta V_{SG2} = 20$ mV – corresponding to a $\sim \frac{1}{2} E_C$ shift in the chemical potential of the dot – leads to the magnetoconductance signature changing from a peak to a dip.

The small excited state energies in Fig. 8.8.b-c) point to a single large quantum dot, extending over most of the device. Since the wave function of this extended system is less confined along the wire, we believe it is also affected by the inhomogeneities of the stray field outside of the side gate gap, which is addressed in more detail in Sec. 8.6.2. Consequently, our single-value offset picture might not apply any longer but would rather require a more rigorous quantum mechanical treatment of the wave function. Furthermore, slight changes in the potential landscape of the device can modify the weight of the wave function enough to probe the stray field in different positions, i.e. different field strengths and directions are probed with different weights. Despite the simple nature of a single quantum dot, the identification of systematic changes in the magnetoconductance proved cumbersome.

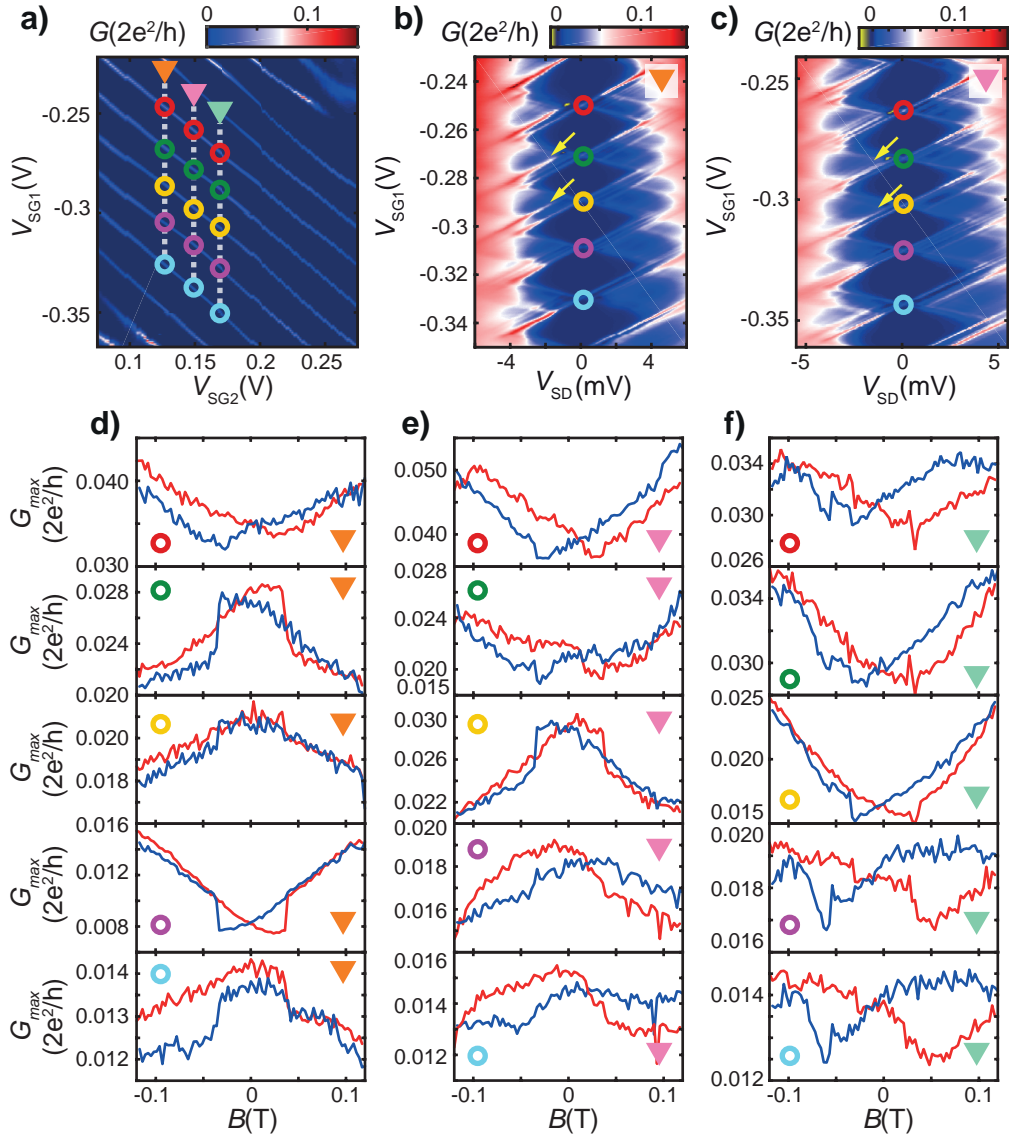


Figure 8.8.: Low-field magnetoconductance in the single-QD regime | a) Conductance map of the studied gate region, with examined cross sections highlighted by dashed lines and marked with triangles. b-c) Charge stability diagram at $V_{SG2} = 130$ mV and $V_{SG2} = 150$ mV, respectively. d-f) Magnetoconductance of the five studied resonances, at $V_{SG2} = 130$ mV, $V_{SG2} = 150$ mV and $V_{SG2} = 170$ mV, respectively.

8.5.2. Strongly coupled double-dot regime

Now, we turn to the magnetoconductance behaviour of resonances in the strongly coupled double-dot regime, which we are able to identify from the hexagonal pattern in Figs. 8.9.b) and 8.10.a). The difference in gate lever arms allows us to identify states of the double-dot molecule with different weights along the nanowire, illustrated in Fig. 8.9.a).

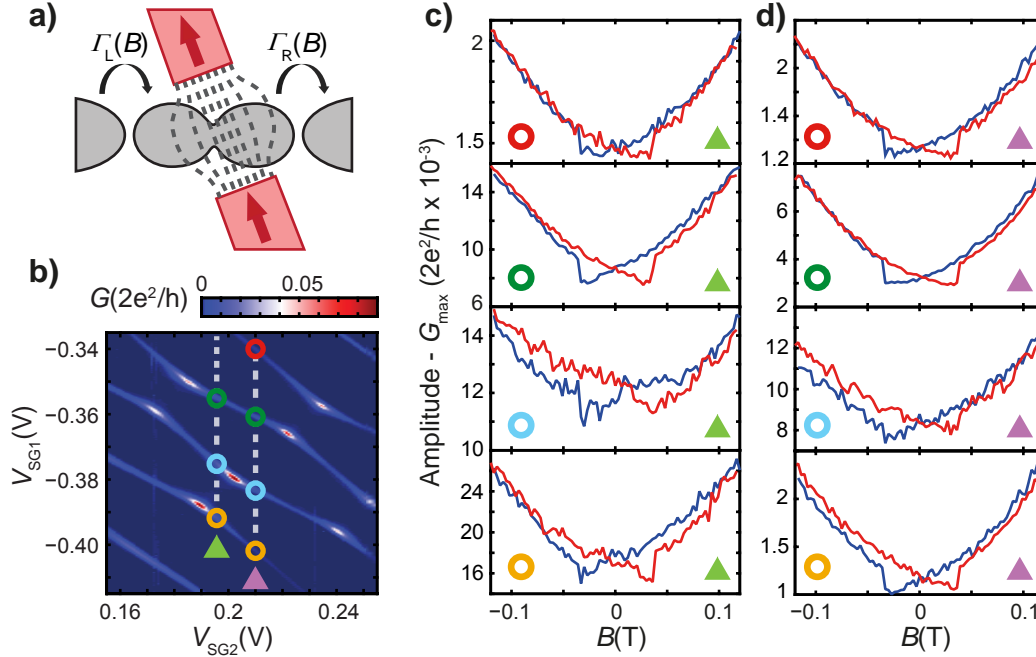


Figure 8.9.: Low-field magnetoconductance in the strongly coupled double-dot regime | a) Sketch of the possible device layout: a double quantum dot with the two islands experiencing different stray fields b) Conductance map of the studied gate region, with examined cross sections highlighted. c-d) Magnetoconductance of the four studied resonances, at $V_{SG2} = 195$ mV and $V_{SG2} = 210$ mV, respectively. Circles identify which curves belong to which resonance, while pointers identify the studied cross section of the conductance map.

In Figs. 8.9 and 8.10, the magnetic field dependence of the maximum conductance of several resonances is investigated at different positions of the honeycomb pattern. On the apexes of the hexagons in Fig. 8.9.b) – the so-called *triple points* – the conductance is significantly higher than elsewhere in the diagram. This refers to the condition of the levels of both QDs being aligned with the leads, allowing resonant tunnelling of electrons through both quantum dots. As we move away from the triple points, the resonances are suppressed by an order of magnitude. However, owing to the strong interdot coupling [85], they are not fully quenched.

In Fig. 8.9.c-d), we investigate the magnetoconductance of resonances which are not on a triple point. Here, we find that parabolic magnetoconductance is characteristic for all off-triple-point resonances measured in this regime. In fact, this type of magnetic field dependence persists up to fields of 500 mT to 1 T, as shown for in the high-field measurements¹ presented in Figs. 8.10.b-c). Interestingly, the low-field magnetoconductance presented in Figs. 8.9.c-d) is remarkably similar for all resonances with comparable relative changes at the coercive field, regardless of the absolute value of the conductance and whether they stem from QD^L or QD^R states.

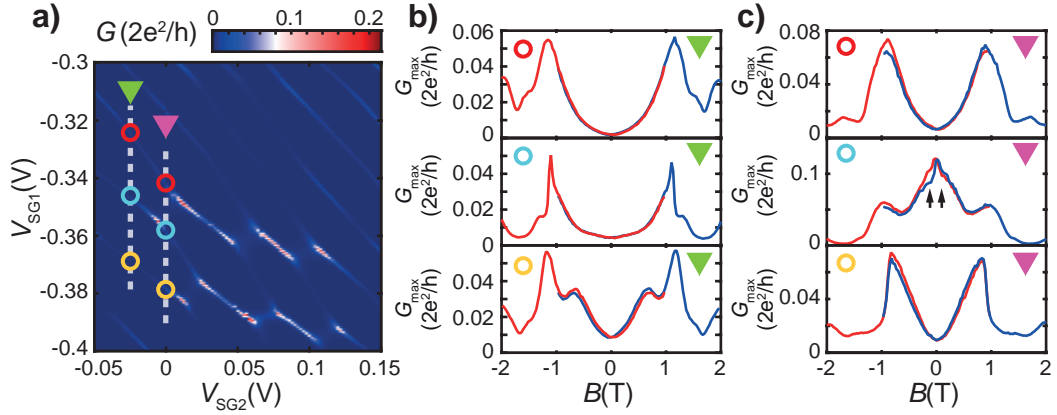


Figure 8.10.: High-field magnetoconductance off and on the triple point | a) Conductance map in the studied side gate voltage region exhibiting double dot features. b-c) Magnetoconductance of the four studied resonances, at $V_{SG2} = -25$ mV and $V_{SG2} = 0$ mV, respectively. Circles identify which curves belong to which resonance, while pointers identify the studied cross section of the conductance map.

In Fig. 8.10, the high-field magnetoconductance is evaluated for two traces of the conductance map in Fig. 8.10.a). In one case, all resonances are far from the triple point (green triangle), while for the other, the middle resonance lies right on the triple point (magenta triangle). The observed magnetoconductance is plotted in Figs. 8.10.b-c) for the two traces respectively. For all off-triple-point resonances, the typical parabolic curves are observed up to different field scales. However, a qualitative deviation occurs when the gate configuration is adjusted so that we probe the magnetic field dependence on the triple points, as shown in the middle panel of Fig. 8.10.c). Instead of the so far typical quadratic increase in magnetoconductance, a peak emerges at zero field. Thus, as the magnetic field is increased, the conditions for serial resonant tunnelling are eventually destroyed. The emergence of this zero-field conductance peak comes as no surprise, since as soon as any parameters are modified, the system can only move away from the resonance condition of the triple point at zero field. Unfortunately, comparison of higher resolution low-field dependence measurements was precluded by a sudden charge rearrangement after the acquisition of the high-field data. Despite

¹Although the presented data is for another set of resonances, the shown dependence is typical for the resonances in Fig. 8.9.

the lower resolution of the field sweeps in Fig. 8.10.c), one can still faintly recognize a hysteretic sawtooth-like shape for the peak, as highlighted by arrows in the middle panel.

The magnetoconductance signature is clearly correlated to the gate configuration, namely whether we are close to the triple points. The observed variations of the resonance parameters are discussed in Sec. 8.6, and we also construct a simple model of the strongly coupled double dot in order to qualitatively reproduce the measured magnetoconductances and switching features. This model is introduced in Sec. 8.6.3

8.5.3. Weakly coupled double-dot regime

The conductance of the device shows strong intensity modulation close to the conductance pinch-off of the device at more negative back gate voltages. In Sec. 8.3, we attributed this to a weakly coupled double quantum dot, where electron transport is only allowed along the avoided crossings near the triple points. Certain resonances in this regime give rise to considerably more complex magnetoconductance features. In the following, we focus mainly on the more exotic features observed in this regime.

In Fig. 8.11.a-b) and c-d), we present the magnetic field evolution of two different resonances exhibiting unique features. The large relative changes in the resonance amplitude are already evident from the conductance maps. The extracted maximum conductances (Figs. 8.11.e) and h)) show strong resemblance to those found in spin-valve devices, based on the tunnelling magnetoresistance between two spin-polarized electrodes [15–17]. The most striking observation regarding these signals is that the changes in conductance can be both positive and negative and the observed relative changes in conductance are up to $\frac{\Delta G}{G} \approx \pm 50\%$, significantly above the usual $< 10\%$ TMR values observed in spin valves based on bottom-up structures [15–17]. Furthermore, the observed change is not an artefact of a shift in the resonance position.

Unlike the resonances discussed up to this point, the resonance width also exhibits considerable changes, which follow the abrupt changes in the resonance amplitudes, as seen in Fig. 8.11.f) and i). However, these changes are of the opposite sign as the variations in the amplitude. While we observe some small jump-like abrupt changes in the resonance positions in Figs. 8.11.g) and j), these changes can also be observed in the position of other resonances, measured simultaneously. Hence, we believe these to be a result of distant trapped charges, affected by the stray field.

Several resonances in the investigated regime are examined at different SG2 voltages along a series of avoided crossings where conductance is measurable, as shown in Fig. 8.12.a). Four cross sections of the map, marked with dashed lines and labelled by triangles, are investigated to determine how the magnetoconductance is affected by the gate voltages.

In Figs. 8.12.b-c), we plot the stability diagrams at two V_{SG2} values. These reveal complicated structures of multiple conductance resonances with markedly distinct slopes, implying that they originate from separate objects.

In Figs. 8.12.d-g), the magnetoconductance is examined at the four configurations highlighted in Fig. 8.12.a), where circles identify the corresponding resonances. Of the resonances studied in Fig. 8.12, only the one labelled with the red circle exhibits magnetotransport features reminiscent of spin-valve behaviour. The other resonances

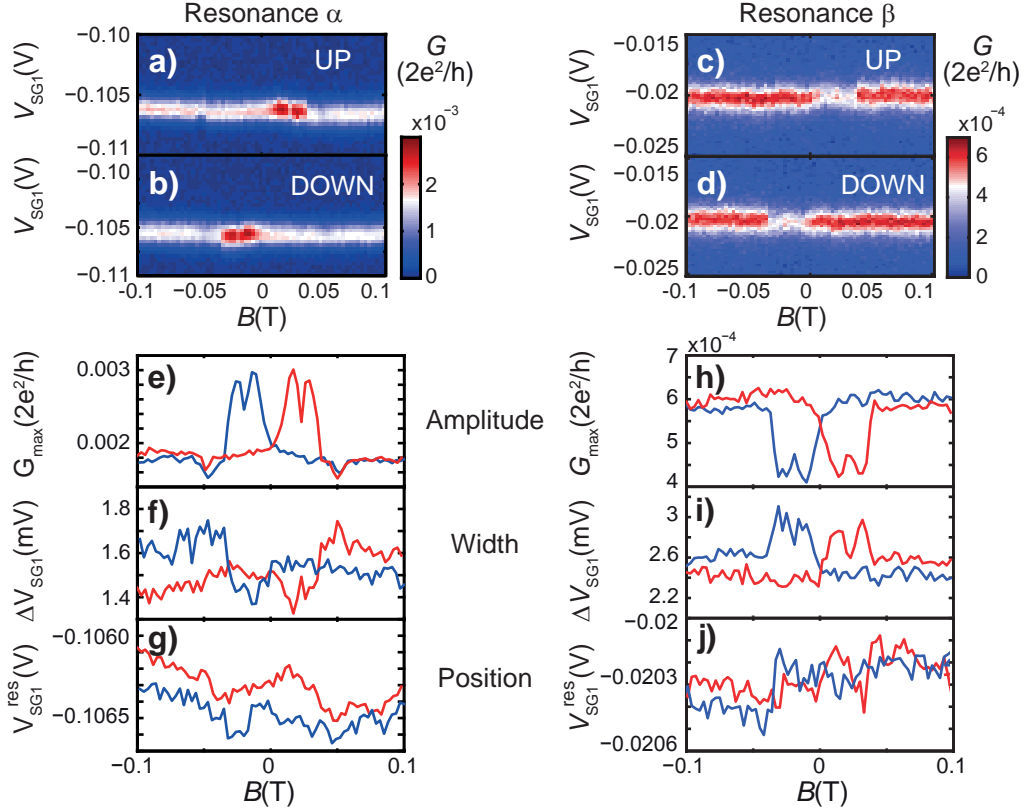


Figure 8.11.: Exotic magnetoconductance of two resonances at different gate configurations, close to pinch-off | a-b) & c-d) Conductance maps as a function of one side gate voltage and the magnetic field for both sweep directions at $V_{BG} = -1.6$ V and at $V_{BG} = -1.7$ V, respectively. These resonances exhibit TMR-like features of positive and negative sign, respectively. e-g) & h-j) Magnetic field dependence of the extracted resonance amplitude, width, and position, respectively.

show magnetoconductances which vary on larger field scales as the coercive field, with hysteretic dips around 50 mT. This is accompanied by changes in the width on similar field scales. These types of magnetoconductances are very similar to the ones discussed in Figs. 8.7.c-d).

As the electrostatic environment is altered by tuning V_{SG2} , the TMR-like magnetoconductance is slightly modified, while the other resonances do not develop any exotic features. This highlights the fact that the exotic magnetoconductance is strongly state-dependent and tunable by changing the gate voltages. We encountered such magnetoconductances for only three resonances. This small sample size was not sufficient to identify systematics for conditions where resonances exhibit such features.

We also examine the bias dependence of the exotic magnetotransport features in Fig. 8.13. We record the device conductance as a function of the magnetic field and the bias voltage, while the gate voltages are constant. The gate position of the scans is highlighted by the dashed line in Fig. 8.13.a).

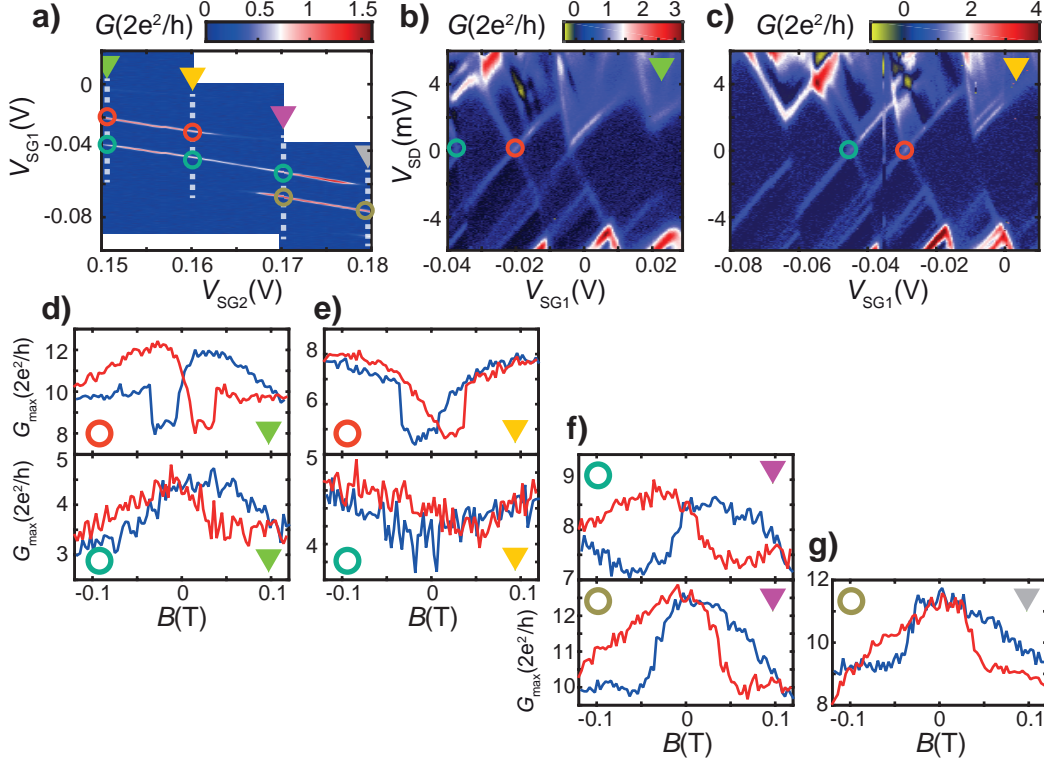


Figure 8.12.: Magnetoconductance of strongly suppressed resonances, close to pinch-off | a) Conductance map of the studied gate region, with examined cross sections highlighted. b-c) Charge stability diagram at $V_{SG2} = 150$ mV and $V_{SG2} = 160$ mV, respectively. d-g) Magnetoconductance of the five studied resonances, at $V_{SG2} = 150$ mV, $V_{SG2} = 160$ mV, $V_{SG2} = 170$ mV, and $V_{SG2} = 180$ mV, respectively. Circles identify which curves belong to which resonance, while triangles identify the studied cross section of the conductance map.

In the bias-dependent magnetoconductance maps shown in Fig. 8.13.b-c), we observe three main features, labelled by squares for identification. We find a wide (yellow square) and a narrow (green square) resonance around zero bias, producing an asymmetric peak with a shoulder, and a broad feature around $V_{SD} = 3.5$ V bias, most probably an excited state (orange square). The dual structure at zero bias can be identified as resulting from the sum of the two ground-state transition lines corresponding to the alignment of the level with the source and drain electrode. These lines have considerably different widths and maximum conductances. While the narrow line at zero bias is seemingly unaffected by the magnetic field, both broad features with negative slopes in the charge stability diagram exhibit significant variations: a continuous suppression is observed as the magnetic field is swept through zero, until the field reaches the coercive field, where the intensity of the broad features is restored. The features around zero bias were evaluated by extracting the parameters of two superimposed Lorentzian curves, used to fit the experimental data. The magnetic field dependence of these parameters is shown in Figs. 8.13.d-i). We see no major changes in

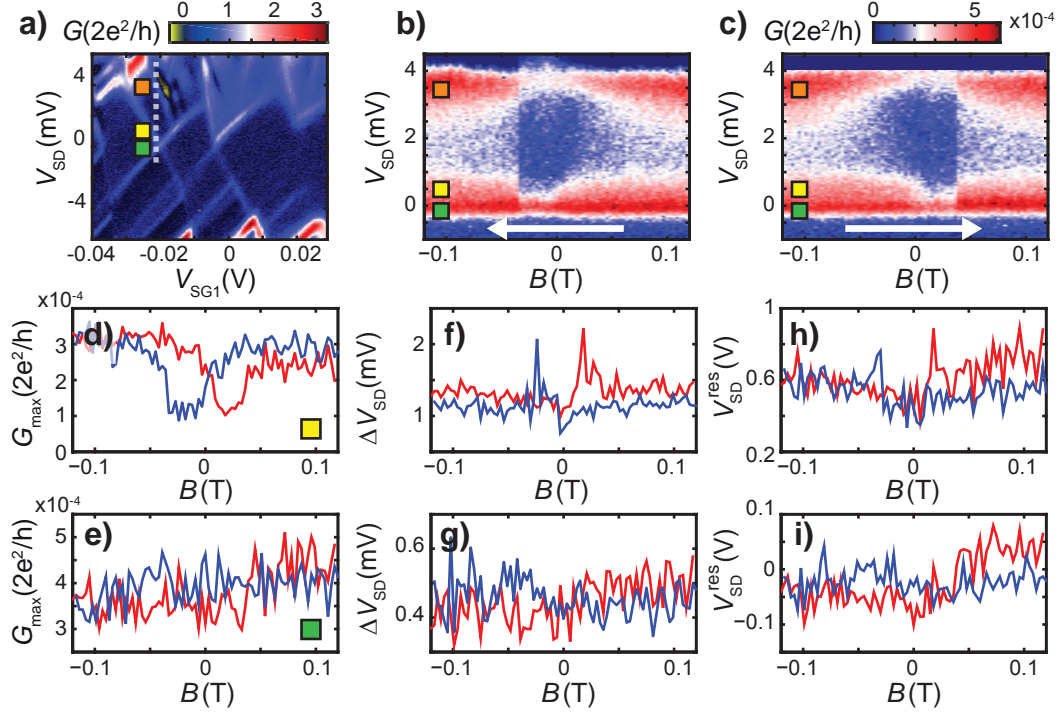


Figure 8.13.: Bias dependence of magnetoconductance at a resonance exhibiting TMR-like behaviour | a) Charge stability diagram as a function of V_{SG1} and the applied bias. The examined cross section is marked by a dashed line, notable features are labelled with squares. b-c) Conductance maps as a function of the magnetic field and applied bias at the gate position marked in a), for both sweep directions. Parameters extracted for the two low-bias features: d-e) amplitude, f-g) width, and h-i) position.

the width (Figs. 8.13.f-g) and position (Figs. 8.13.h-i) of the features. The amplitudes (Figs. 8.13.d-e) confirm our initial judgement, that only the broad feature is modified.

In a simple picture of a quantum dot system, we would not expect such differences in these two lines as the conductance is given by the coupling to both electrodes [70, 71], regardless of the bias applied. Although we are not sure about the origin of these discrepancies, we see a clear difference in their magnetic field dependence, which seems to account for the exotic features of the resonance. In Sec. 8.6, we further speculate on the origin of observed magnetoconductances. Furthermore, we construct a simple model to qualitatively describe the spin-valve-like behaviour by considering ground-state transitions in Sec. 8.6.4.

8.6. Discussion

In this section, we assess the experimental observations of the chapter and discuss the possible underlying physics of these phenomena.

Firstly, we formulate the results of our experiments in terms of coupling strengths to aid our analysis in Sec. 8.6.1. Although the sample geometry is quite simple, the conductance of the sample and its variations in magnetic field can be a result of multiple factors. In Sec. 8.6.2, we review these possible effects, which could affect the magnetoconductance of the sample. Furthermore, we propose simple models to capture the magnetoconductance features of the strongly and weakly coupled double-dot regime, in Sec. 8.6.3 and Sec. 8.6.4, respectively. The simulations provide qualitative agreement with the measurements, supporting our assumptions.

8.6.1. From amplitudes and widths to tunnel couplings

We evaluate the observed amplitude and width variations by calculating the $\Gamma_{1,2}$ coupling strengths used in a double barrier picture. In case the temperature broadening is negligible ($(\Gamma_1 + \Gamma_2) \gg k_B T$), these measurable parameters can be formulated as a function of the coupling strengths as

$$G_{\max} = \frac{2e^2}{h} \frac{4\Gamma_1\Gamma_2}{(\Gamma_1 + \Gamma_2)^2}, \quad \text{and} \quad \Delta V_{\text{res}} = \frac{\Gamma_1 + \Gamma_2}{|e|\alpha_{\text{SG1}}}. \quad (8.2)$$

Using the expressions in (8.2), one can deduce the values of Γ_1 and Γ_2 , however, the calculated values cannot be assigned to individual leads. Accordingly, we use the $\Gamma_1 > \Gamma_2$ definition from here on. The maximum conductance is governed by the ratio of the couplings while the width is determined by their sum.

It should be noted that the studied resonances are on the brink of the temperature-broadened regime ($(\Gamma_1 + \Gamma_2) \sim k_B T$), i.e. the Lorentzian line shape and Eq. (8.2) are only an approximation. Hence, the extracted Γ values only serve to provide qualitative understanding as the maximum conductance is suppressed by the temperature, and the extracted coupling asymmetries only provide an upper bound.

We first examine the four resonances presented previously in Fig. 8.7. These four examples exhibit typical magnetoconductance signatures most common in our measurement data. The calculated coupling strengths are plotted in Fig. 8.14. Here, the magnetic field dependence of the examined resonances is presented again in Fig. 8.14.a-d) for easy identification.

A considerable asymmetry of ~ 100 - 300 is found for all resonances, which is rather an upper bound for the asymmetry, due to the non-negligible effect of the temperature. Most magnetoconductance curves exhibit a similar variation in resonance width and thus these changes are determined by $\Gamma_1(B)$. This coupling term is responsible for the characteristic magnetic field dependence of the width which occurs on larger field scales than the coercive field. The peculiarities of the magnetoconductance, like the sharp switches in the resonance amplitude, are seemingly encoded in the smaller Γ_2 values. As the width does not show significant qualitative changes, the differences

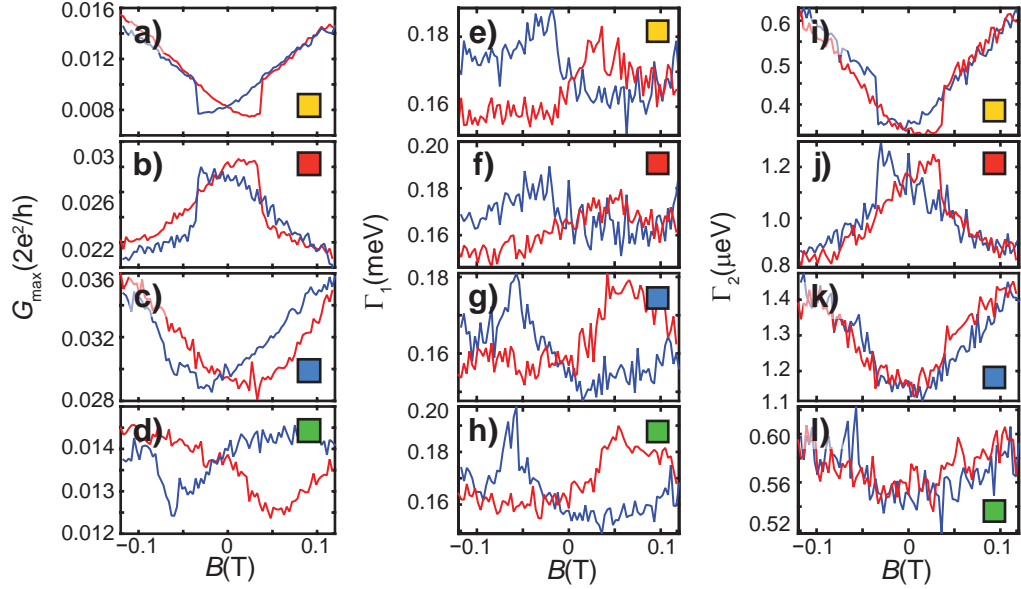


Figure 8.14.: Magnetic field dependence of couplings | The coupling strengths are extracted from the maximum conductances and resonance widths in Fig. 8.7. using Eq. (8.2). For easy recognition, the magnetic field dependences are plotted again in a-d). Square labels correspond to the ones used in Fig. 8.7. to identify the studied resonances.

between the conductances stem from a change in smaller coupling. Although similar abrupt variations might occur in $\Gamma_1(B)$, their absolute value is negligible compared to the variations otherwise encountered. In this sense, small coupling might be a necessity for the observation of magnetoresistive phenomena in our samples.

In the cases where no magnetoconductance switching occurs, such as in Fig. 8.14.c-d), the large field scale variations in the amplitude are a result of changes in the larger Γ_1 , as no hysteresis is found in the smaller Γ_2 values. This means that the dip in the conductance is a result of the resonance broadening. These observations hold true for most resonances, as the encountered coupling asymmetries are generally quite large and all these resonances exhibit the qualitatively identical width dependence.

For exotic magnetoconductances discussed in Sec. 8.5.3, in contrast to the usual findings, we observe visible variations in both couplings. The coupling strengths extracted in Figs. 8.11.k-l) and m-n) reveal significantly larger asymmetries than previously $\Gamma_1/\Gamma_2 > 2000$, which account for the low conductances of the resonances. As with the amplitude and width, the two couplings also exhibit step-like changes, with opposite sign around 0 and 35 mT. Thus, unlike previously, we find abrupt changes in both Γ_1 and Γ_2 . This could signify that both wave function overlaps are considerably modified. We speculate that the discussed exotic features only arise close to the depletion of the nanowire as the reduced electron density increases the prominence of charge puddles, which might significantly affect the wave function of the system. However, one would only expect significant changes around the coercive field and not around zero, thus the origin of the TMR-like curves seems to lie in other phenomena.

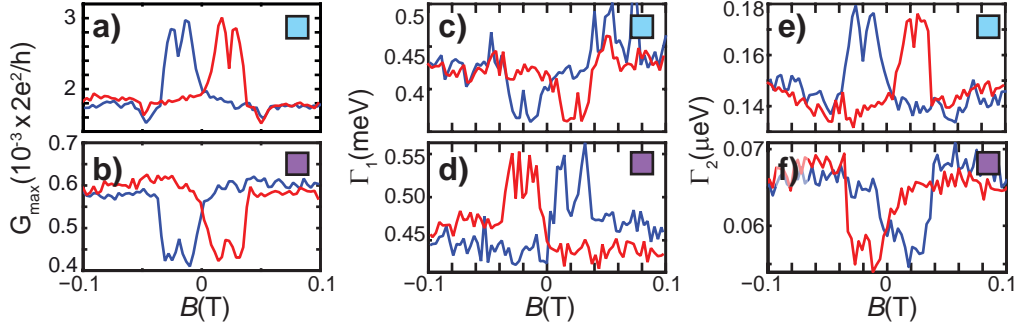


Figure 8.15.: Magnetic field dependence of couplings for resonances exhibiting exotic magnetoconductance | The coupling strengths are extracted from the conductances and widths in Fig. 2.4 using Eq. (8.2). Square labels identify the studied resonances.

In TMR experiments, the two ferromagnetic contacts serve as the spin polarizer and analyzer ferromagnets of a spin-valve device. In our devices, only the stray field of the nanomagnets is present, however, if only fully spin-polarized levels are available on the QDs for electron transport, the two quantum dots of a double-dot system can be thought of as analogues of the magnetic contacts. In this case, with coercive fields of $B_{c,1} \approx 0$ mT and $B_{c,2} \approx 35$ mT. While this tentative explanation sounds feasible, the energy scale of the Zeeman splitting ($E_Z < 60 \mu\text{eV}$) is significantly lower than the encountered resonance broadenings ($\Delta E > 150 \mu\text{eV}$). However, inhomogeneities of the field might also play a role, as we will discuss in Sec. 8.6.2.

In Sec. 8.6.4, we consider the effect of transitions between ground states with different spatial symmetries, leading to characteristic changes in the magnetoconductance. We construct a simple model, with which we can create a qualitative recreation of our measurements, corroborating this theory.

8.6.2. Effects behind changes in the coupling

Multiple factors can lead to field-dependent couplings. Here, we review three main factors, the effect of the magnetic field of tunnelling electrons and electrons confined to the dot, and the spatial variations in the magnetic stray field.

Magnetic field dependence of wave functions

The most straightforward approach is the direct effect of the magnetic field on the electron wave function in our device. We have seen how the electrostatic potential could modify the wave function of the device, and – by extracting the capacitances of the gates – we could also give a qualitative picture of the device as a strongly coupled double quantum dot, the equivalent circuit of which is shown in Fig. 8.16.a). The magnetic field might also change how wave functions overlap by changing the size of the dots or their relative position to the leads and each other.

A typical example of the direct influence of the magnetic field on the wave function can be given for quantum dots in a magnetic field described in the Fock–Darwin approximation [14]. In this simple picture, the quantum dot is expected to extend over the length scale: [206]:

$$l_{\text{QD}}(B) = \sqrt{\frac{\hbar}{\omega_C m^*}} \sqrt[4]{1 - \frac{\Omega^2}{\omega_C^2}}, \quad (8.3)$$

where Ω characterizes the parabolic confinement and $\omega_C = eB/m^*$ is the cyclotron angular frequency. In this case, the transport properties and thus the coupling strengths will be defined by the overlap of the quantum dot wave functions and the leads, as illustrated in Fig. 8.16.b). This might explain why the small Γ_2 values show abrupt changes, as even small changes in overlap lead to noticeable relative changes. For Γ_1 , the overlap might be considerably larger, small changes will not be observable. Furthermore, the confinement also plays a significant role since it determines the field scale over which the dot size shows significant changes.

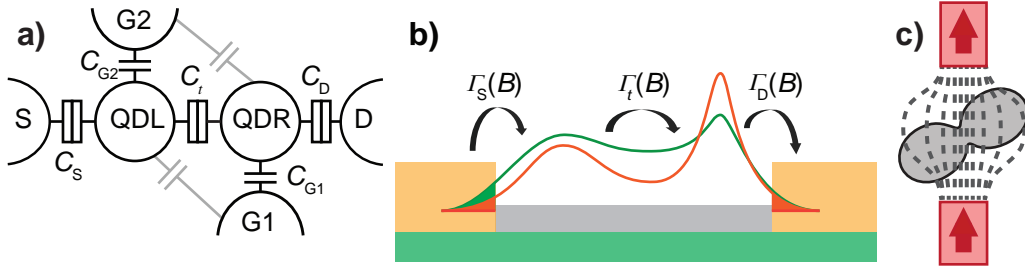


Figure 8.16.: Illustration of factors affecting the magnetoconductance | a) Capacitance model of the device. b) Schematic illustration of device wave functions and wave function overlaps with the leads. c) Schematic illustration of possible stray field inhomogeneities along the device.

This phenomenon can also be approached in another manner. One can assume that by modifying the wave function, the local density of states for electrons tunnelling on and off the quantum dot is modified. The conductance is affected as the transmission and thus the coupling is determined by the local density of states at the Fermi energy. We have used this approach to construct a toy model of the strongly coupled double-dot system, with which we could qualitatively reproduce the quadratically increasing magnetoresistance and the zero-field conductance peak for resonances away and on the triple point, respectively. We discuss the model and present simulated data in Sec. 8.6.3.

Inhomogeneities in the magnetic stray field

We have many times alluded to the influence and non-trivial nature of the possible variations in the magnitude and direction of the stray field over the length of the device, which could play a crucial role. We illustrate the different stray field patterns in a hand-waving fashion in Figs. 8.17.a-d). A few examples of different inhomogeneities are shown in Figs. 8.17.e-h), which we discuss in the following.

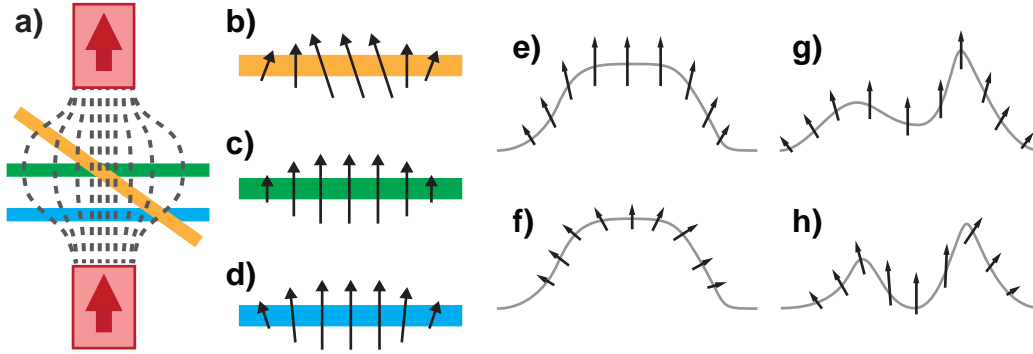


Figure 8.17.: Stray fields along a nanowire | a) Three different nanowire geometries in the stray field of a nanomagnet pair. b-d) $\mathbf{B}_{\text{stray}}$ patterns along nanowires with different relative orientations to the nanomagnets. The orange line is a good approximation of the situation for the studied device. e-h) Illustration of stray field inhomogeneities being probed by different wave functions: symmetric wave function probing symmetric stray (e) and asymmetric stray field distribution (f), modification of the wave function also modifies the weight of the probed inhomogeneities (g-h).

Firstly, we turn to Fig. 8.17.e) and f), which illustrates the extended wave functions envisaged for a single quantum dot with the arrows referring to the variations in the stray field over the length of the wire. In the case of Fig. 8.17.e), most of the wave function is affected by the near-homogeneous field in the middle of the device, however, the tunnelling electrons will be affected by significantly different fields. The large extent of the wave function means that the quantum dot might also average over more prominent inhomogeneities, like in Fig. 8.17.f), which could lead to a complicated magnetic field dependence for the wave function.

The wave function will show much more variation over the device for strongly coupled double dots, as shown in Fig. 8.17.g). This means that the electrons on the quantum dot will probe the stray field with different weights, i.e. averaging over a much smaller portion of the inhomogeneous field. We believe that this could result in a more well-defined stray field for the two smaller quantum dots, as opposed to the single dot, which could also explain why our measurements in the strongly coupled double-dot region showed more systematic changes, which we could assign to whether the resonance was away or on the triple point.

For the weakly coupled quantum dots, where exotic TMR-like magnetoresistances were observed, a situation such as in Fig. 8.17.h) might be present. Here, the interdot tunnelling is lower and the two dots are more decoupled from each other. In such a case, the local field might define locally different spin quantization axes for the two

dots. As a result, matrix elements for electrons tunnelling between the two dots will be determined by their spin projection and will thus depend on the sum of the external and locally present stray fields. Such a situation would be conceptually similar to the idea of the entanglement detection scheme in Ref. [29], however, the Zeeman splitting of the levels discussed here is below the broadening of the level. We speculate that these TMR-like signals stem from changes in the ground state of the system.

Magneto-tunnelling

The magnetic field can also affect the tunnelling electrons through the Lorentz force, leading to a gain in the \mathbf{k}_t transverse momentum of the tunnelling electrons proportional to \mathbf{B} . The affected electrons thus probe the wave function in \mathbf{k} -space, perpendicular to the axis of the nanowire. Their tunnelling probabilities and the resulting conductance are influenced by the magnetic field. This phenomenon is referred to as magneto-tunnelling [80, 81], and is discussed in more detail in Sec. 2.2.4. A sudden change in the magnetic field can also change the \mathbf{k}_t wave vector and the tunnelling probabilities and magnetoconductance.

In the case of magneto-tunnelling, the electron is affected by the local magnetic field over the tunnelling length. This is a well-defined distance in the case of sharp barriers in a heterostructure, however in the case of quantum dots defined between metallic contacts, barriers are often shallow, the effective tunnelling distance of the electron might change depending on their momentum. As the length of the barrier is not well-defined, the variation in the magnitude and stray field will be averaged out, and inhomogeneities of the stray field might play a significant role in determining the magnetoconductance features, especially for the seemingly non-systematic behaviour in the single-dot regime.

8.6.3. Model of local DOS for strongly coupled double dots

A simple model system is constructed in order to provide a tentative explanation for some encountered magnetoconductance features.

We assume the strongly coupled quantum dot system tunnel-coupled to two electrodes at zero temperature. The wave functions in this extended structure have different weights along the nanowire, thus the coupling to the leads and the gates may vary from state to state. We model this by considering a local density of states (DOS) at the source and drain electrodes, which determines the tunnelling probabilities to the two electrodes.

We consider a two-fold spin-degenerate level at both ends of the device with a lifetime-broadened Lorentzian density of states:

$$\rho(x, \gamma, \delta) = L(x, \gamma, \delta) = \frac{(\gamma/2)^2}{(\gamma/2)^2 + (x - \delta)^2}, \quad (8.4)$$

where ρ is the density of states, L is normalized to 1 for simplicity, γ is the full width at half maximum, δ corresponds to the detuning of the peak position with respect to E_F , and $x = E - E_F$ is the energy relative to the Fermi energy.

The two spin levels are split in a magnetic field and have linear field evolution according to the Zeeman terms of $\pm\frac{1}{2}g\mu_B B$. The δ detuning of the spin levels with respect to the Fermi energy is then

$$\delta_{\uparrow}^{L/R}(V_g) = \delta_0^{L/R}(V_g) + \frac{1}{2}g_{L/R}\mu_B B^{L/R}, \quad \text{and} \quad \delta_{\downarrow}^{L/R}(V_g) = \delta_0^{L/R}(V_g) - \frac{1}{2}g_{L/R}\mu_B B^{L/R}, \quad (8.5)$$

where $\delta_0 = E_0 - E_F$ is the detuning of the degenerate level at $B = 0$. By plugging in these δ parameters into Eq. (8.4), we obtain a DOS with two peaks for the two spin channels, as shown in Fig. 8.18.a).

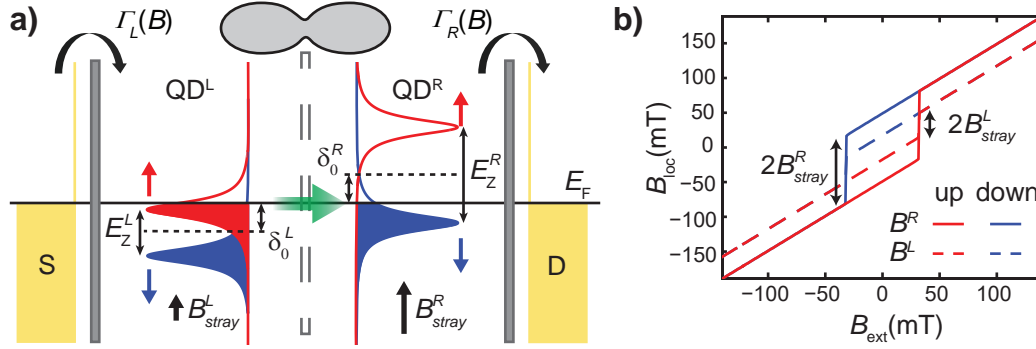


Figure 8.18.: Illustration of model system for the DQD transport features | a) DOS for spin-split levels near the contact electrodes. b) External field dependence of local magnetic fields from FSG magnetization calculated from Stoner–Wohlfahrt model, red (blue) curves refer to upward (downward) sweep direction.

As the potential on the QD is changed via the gate electrodes, the chemical potential of the QD is also modified. Accordingly, the electrostatic gating of the device is accounted for in the $\delta_0^{L/R}$ detuning parameters. Furthermore, the electrostatic gating of the double quantum dot structure is not ideal, as both dots are detuned by both gates. This capacitive crosstalk is considered via the following symmetric matrix:

$$\begin{bmatrix} \delta_0^L \\ \delta_0^R \end{bmatrix} = \begin{bmatrix} 1 & cc \\ cc & 1 \end{bmatrix} \begin{bmatrix} e\alpha_L V_L \\ e\alpha_R V_R \end{bmatrix}, \quad (8.6)$$

where $V^{L/R}$ and $\alpha_{L/R}$ are the gate voltages and corresponding lever arms for the two quantum dots, and cc is the capacitive crosstalk from one gate to the other dot.

The local magnetic field is given by the scalar sum of the external magnetic field and the stray field created by the magnetization of the ferromagnetic side gate:

$$B_{loc}^{L/R} = B_{ext} + B_{stray}^{L/R} = B_{ext} + \beta^{L/R}\mu_0 M(B_{ext}). \quad (8.7)$$

For simplicity, we assume $\mathbf{B}_{ext} \parallel \mathbf{B}_{stray}^{L/R}$. The switching behaviour of the ferromagnetic side gate is simulated in the Stoner–Wohlfahrt model [63] where we set the parameters, such that the magnetization reversal occurs at the experimentally observed B_c and the resulting magnetization is $\mu_0 M_S = B_c$. The strength of the stray field on the individual quantum dots is given by the dimensionless β parameter:

$$\beta^{L/R} = \frac{B_{stray}^{L/R}}{\mu_0 M}. \quad (8.8)$$

In our model, electron spin is assumed to be preserved during the transport process, while spin relaxation, decoherence and dephasing are neglected for simplicity. It should be noted that this is a considerable simplification of our material system, as the strong spin–orbit interaction in InAs will lead to a mixing of the spin-up and spin-down states and thus creating new Kramers doublet eigenstates.

For the calculation of the transport properties, the structure is assumed to be tunnel-coupled to the leads. Accordingly, the $\Gamma_{L/R}$ tunnel rates on both sides are given by the local density of states at the Fermi energy and the effective transmission is then given by the product of the two. In this case, we have chosen perfect interdot transmission. The conductance is then, to the lowest order, the sum of the conductance contributions of the two spin channels:

$$G \propto \Gamma_R \Gamma_L = \rho_L(E_F) \rho_R(E_F) = \rho_L^\uparrow(E_F) \rho_R^\uparrow(E_F) + \rho_L^\downarrow(E_F) \rho_R^\downarrow(E_F). \quad (8.9)$$

The resulting $G(B, \delta_0^R)$ conductance maps and the extracted conductance maxima for both sweep directions are summarized in Fig. 8.19 for different values of δ_0^L . For the calculations, realistic parameters of $g_L = 10$, $g_R = 7$, $\gamma_L = 0.15$ meV, $\gamma_R = 0.1$ meV, $\beta_L = 1.4$, $\beta_R = 0.5$, $cc = 0.2$ were used.

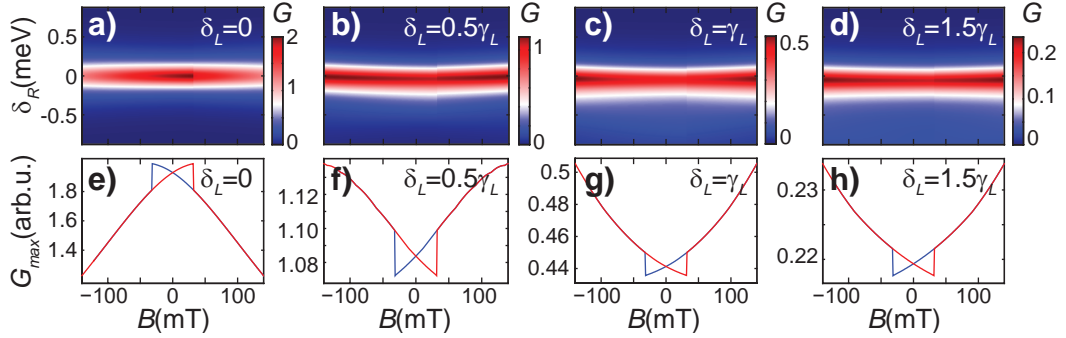


Figure 8.19.: Magnetoconductance calculated from toy model | a-d) Calculated $G(B, \delta_0^R)$ conductance maps and e-h) extracted peak maxima for δ_0^L detuning values of $0, \frac{1}{2}\gamma^L, \gamma^L$, and $\frac{3}{2}\gamma^L$, respectively.

The model qualitatively reproduces the bell-curve-like magnetoconductance with a peak near zero magnetic field for the case of both levels being aligned with leads ($\delta^L = \delta^R \approx 0$). As one QD is detuned from the triple point, the MR changes considerably, exhibiting the typical parabolic-like curves, offset by the stray field, once

again emulating the experimental data. Similarly to the experiments, no significant shifts are visible in the resonance position. However, the model predicts a broadening increasing with the applied field due to the separation of the peaks in the DOS, which does not conform to our experimental findings. In short, the model accounts for the observed relative changes in conductance but not the width with the same parameters.

8.6.4. Toy model for magnetoconductance changes from ground-state transitions

The exotic TMR-like features in the weakly coupled double-dot regime could not be accounted for by the above introduced model. The model successfully reproduced characteristic magnetoconductance signatures by tuning the spin-split local DOS at the two interfaces. The effect of the FSG stray field resulted in a field offset in the magnetic field dependence, which instantaneously changes sign when the side gate magnetization is inverted at the coercive field (B_c). In this case, however, no ground-state transitions could be considered.

The eigenstates of the system are not simply the single-electron spin states as assumed previously. The simplest two-electron case of a weakly coupled double quantum dot with single filling of the two dots – i.e. the (1,1) configuration – already leads to the formation of spin-triplet states. For simplicity, we neglect multiple charging of the system and restrict our model to the subset of these S – T states. The four corresponding eigenstates are thus the $|T_+\rangle$, $|T_0\rangle$, and $|T_-\rangle$ triplet states and the $|S_{11}\rangle$ singlet state:

$$T_+ = |\uparrow\uparrow\rangle, \quad T_0 = \frac{1}{\sqrt{2}}(|\uparrow\downarrow\rangle + |\downarrow\uparrow\rangle), \quad T_- = |\downarrow\downarrow\rangle, \quad S_{11} = \frac{1}{\sqrt{2}}(|\uparrow\downarrow\rangle - |\downarrow\uparrow\rangle). \quad (8.10)$$

The energies of these states depend on the magnetic field at the positions of the two QDs, \mathbf{B}_{loc}^L and \mathbf{B}_{loc}^R . The eigenenergies of this system can be found by diagonalizing the Hamiltonian H in the $|T_+, T_0, T_-, S_{11}\rangle$ basis, following Refs. [207, 208]:

$$H = g^* \mu_B \begin{pmatrix} \bar{B}_z & \frac{1}{\sqrt{2}}\bar{B}_- & 0 & -\frac{1}{\sqrt{2}}\Delta B_- \\ \frac{1}{\sqrt{2}}\bar{B}_+ & 0 & \frac{1}{\sqrt{2}}\bar{B}_- & \Delta B_z \\ 0 & \frac{1}{\sqrt{2}}\bar{B}_+ & -\bar{B}_z & \Delta B_+ \\ -\frac{1}{\sqrt{2}}\Delta B_+ & \Delta B_z & \Delta B_- & \frac{E_X}{g^* \mu_B} \end{pmatrix}, \quad (8.11)$$

where E_X is the exchange splitting energy, and the B operators are:

$$\bar{\mathbf{B}} = \frac{1}{2}(\mathbf{B}_{loc}^L + \mathbf{B}_{loc}^R), \quad \Delta\mathbf{B} = \frac{1}{2}(\mathbf{B}_{loc}^L - \mathbf{B}_{loc}^R), \quad \bar{B}_\pm = \bar{B}_x \pm \bar{B}_y, \quad \text{and} \quad \Delta B_\pm = \Delta B_x \pm \Delta B_y. \quad (8.12)$$

For this model, we neglect spin-orbit interactions and spin-active scattering, as well as assume a negative exchange term $E_x < 0$, i.e. an energetically more favourable singlet state for $B = 0$. The magnetic field on the two dots is given as the sum of the externally applied field and the stray field at the given position:

$$\mathbf{B}_{loc}^{L/R} = \mathbf{B}_{ext} + \mathbf{B}_{stray}^{L/R}. \quad (8.13)$$

It should be noted that contrary to the previously discussed model, here we use field vectors. The stray field vectors are considered to be constant with their orientation inverted at B_c , following the magnetization reversal of the ferromagnetic strips.

The external magnetic field is chosen to lie along the Py strip, i.e. $\mathbf{B}_{ext} \parallel \mathbf{M}$, just as in the performed experiments. For simplicity, we examine the simple case of $|\mathbf{B}_{stray}^L| = |\mathbf{B}_{stray}^R| = B_{stray}$. Furthermore, we restrict the stray field vector to the $y-z$ substrate plane, where both vectors are tilted away from the $z \parallel \mathbf{M}$ axis by $\frac{1}{2}\theta$ in opposite directions, i.e. θ is the angle between \mathbf{B}_{stray}^L and \mathbf{B}_{stray}^R .

We investigated two simple cases, where the stray field is homogeneous at $\theta = 0^\circ$ (Fig. 8.20.a) and where \mathbf{B}_{stray}^L and \mathbf{B}_{stray}^R are slightly askew by $\theta = 30^\circ$ (Fig. 8.20.b).

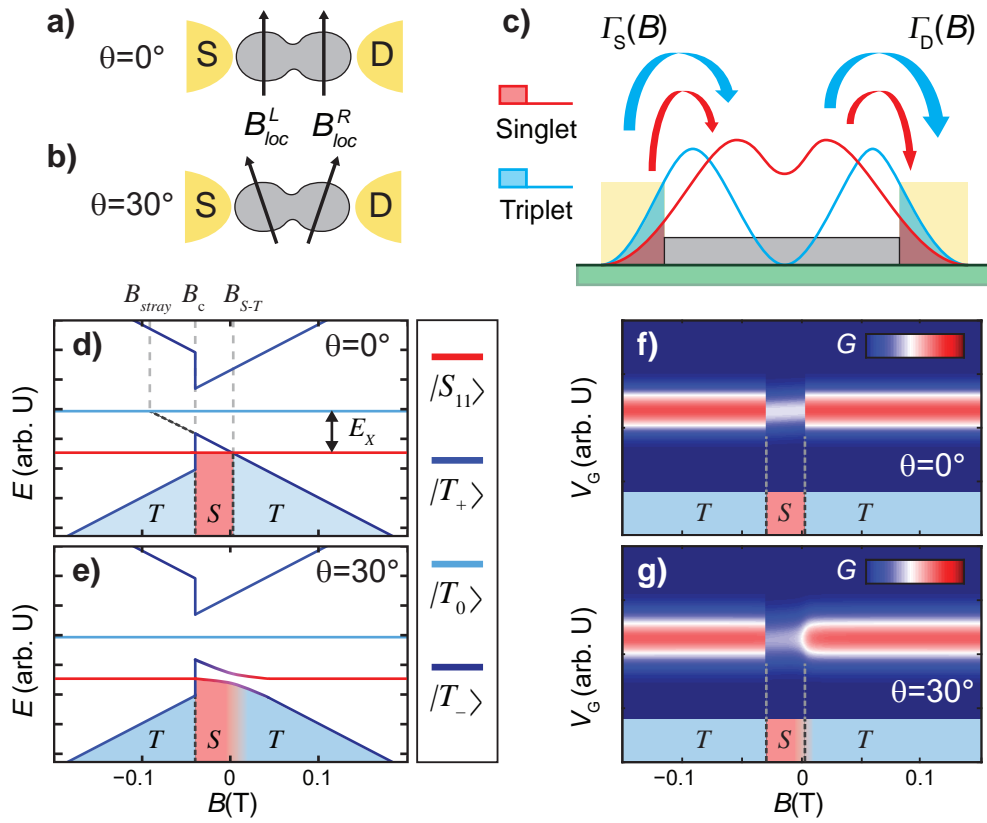


Figure 8.20.: Ground-state transition leading to TMR-like magnetoconductance | a-b) Schematic illustration of the two studied cases of $B_{loc}^{L/R}$ local field configurations for $\theta = 0^\circ$ and $\theta = 30^\circ$, respectively. c) Hand-waving picture of wave functions and overlap integrals for S and T states with different symmetries. d-e) Magnetic field dependence of the energy spectrum of the four eigenstates in a downwards field sweep for $\theta = 0^\circ$ and $\theta = 30^\circ$, respectively. f-g) The corresponding simulated conductance maps for the lowest-energy state for $\theta = 0^\circ$ and $\theta = 30^\circ$, respectively. The $S - T$ ground-state transitions are highlighted for clarity.

The energies of the four eigenstates are calculated by diagonalizing the H matrix for each magnetic field value. The resulting magnetic field dependent energy diagrams are plotted for a downwards field sweep in Figs. 8.20.d-e) for $\theta = 0^\circ$ and $\theta = 30^\circ$, respectively. In both cases, the $|T_+\rangle$ and $|T_-\rangle$ states are shifted as the external magnetic field is applied, while $|T_0\rangle$ and $|S_{11}\rangle$ remain unaffected. For the large positive fields the lowest-energy state is the $|T_+\rangle$ triplet. By decreasing the field, its energy increases and becomes degenerate with the singlet state $|T_{11}\rangle$. For a homogeneous stray field ($\theta = 0^\circ$), a direct crossing of the $S - T$ states occurs, shown in Fig. 8.20.d). This is expected since for homogeneous magnetic field all off-diagonal elements of H vanish, leading to a diagonal Hamiltonian and orthogonal eigenstates. As a result, a sudden transition from a triplet to the singlet ground state occurs at B_{S-T} field, determined by the magnitude of the exchange interaction and the stray field, and is given by:

$$B_{S-T} = B_{stray} - \frac{E_X}{g\mu_B}. \quad (8.14)$$

A clear difference is found in the energy diagram for $\theta = 30^\circ$, shown in Fig. 8.20.e). The Hamiltonian for non-parallel stray fields at the QD positions is no longer diagonal, allow a mixing between S_{11} and $T_{+/-}$ states in this case. The eigenstates become coherent superpositions of both original states, resulting in an avoided crossing around B_{S-T} . The weight of the singlet increases as B is swept further through zero field. As the magnetic field is swept even further to negative values, the magnetization of the ferromagnetic side gate is reversed at the B_c coercive field. This results in a sharp discontinuity in the magnetic field dependence of the $T_{+/-}$ states. A second ground-state transition occurs, as the lowest-energy state is reverted to the pure $|T_+\rangle$ triplet.

Changes in the ground state, such as the modelled singlet/triplet transition would only be observable in conductance measurements if the intrinsic conductances of the two states are different. Due to the Pauli exclusion principle, the orbital wave functions of the singlet and triplet states exhibit different spatial symmetry. The change in spatial distribution is also expected to affect the overlap integrals and corresponding tunnel couplings, altering electrical conductance for these states. This is illustrated for an extreme situation in Fig. 8.20.c). A change from a triplet ground state to a singlet (and back) can thus modify the device resistance. For simplicity, we calculated the conductances in this model as

$$G_{\max} = |\eta_S|^2 G_S + |\eta_T|^2 G_T, \quad (8.15)$$

where the $\eta_{S/T}$ superposition amplitudes are the spectral weights of the $S - T$ states, obtained by considering the eigenstates of H , and the characteristic conductances in the singlet and triplet ground state, G_S and G_T , respectively.

Conductance maps shown in Fig. 8.20.f-g) are modelled by assuming Lorentzian gate sweep profiles. The magnetic field dependence of the G_{\max} amplitudes is calculated using Eq. (8.15) with $G_S < G_T$. The $\eta_{S/T}$ values are determined by following the lowest-energy eigenstates of the corresponding energy diagrams in Fig. 8.20.d-e).

The singlet-triplet ground-state transitions are manifested as large changes in G around zero at B_{S-T} and at the B_c coercive field of the FSG. For $\theta = 0^\circ$, both these changes are abrupt and sharp, however, the transition around B_{S-T} is smoothed out for tilted stray fields, with its width determined by the θ angle. The simulated conductance map for $\theta = 30^\circ$ in Fig. 8.20.g) is in very good qualitative agreement with the negative TMR-like magnetoconductance encountered in the weakly-coupled double-dot regime.

In addition, considering the next charge state, the inverse of the ground-state transitions occur, leading to opposite, positive TMR-like behaviour. However, this is not a real ground-state transition, rather in the excited states. Furthermore, in our model, we restricted ourselves to the simplest two-electron picture with a 4-state singlet-triplet basis which provided a very good qualitative description. In reality, we might observe transitions between much more complicated ground states with non-trivial spatial symmetries, explaining the inverse TMR-like signal. Since only two resonances were found to exhibit exotic, TMR-like magnetoconductance features, data was insufficient to identify systematic behaviour which would help us better understand the underlying physics and improve our simulations.

It is clear from our model that the TMR-like signal can only arise for a special set of conditions, namely that B_{S-T} is reached before the coercive field of the FSG is reached, i.e $B_{S-T} > B_c$ for the downwards sweep. Accordingly, a special set of the multiple parameters is required, most importantly: the magnitude of the stray field B_{stray} , the coercive field B_c , and the magnitude of the exchange splitting E_X .

We restricted the discussion of the result from the model to the downwards sweep, however, the upwards sweep is identical to the presented case, with the abscissa axis mirrored, resulting in a hysteresis.

In summary, by evaluating the maximum conductance and the width of the resonances, we extracted the magnetic field dependence of the coupling energies to give a qualitative description of the physics behind the change in conductance. Large asymmetry is found in the coupling strengths, where the large $\Gamma_1(B)$ accounts for the large field scale variations in the width, while sharp switching features in the amplitude are found to arise in the much smaller $\Gamma_2(B)$. For exotic magnetoconductances discussed in Sec. 8.5.3, in contrast to the usual findings, we observed visible variations in both couplings.

We discussed multiple factors which may affect the conductance: the direct effect of the magnetic field on tunnelling electrons, the effect of the magnetic field modifying wave functions and their overlap integrals, and inhomogeneities of the magnetic stray field. Furthermore, we constructed a toy model of a perfectly coupled double-dot system, where the changes in wave function overlaps were formulated as changes in the local DOS. This model reproduced the magnetoconductance features of the amplitude in the strongly coupled regime, however could not account for the variations in the width. We also considered the possible ground-state transitions in a weakly coupled double quantum dot, which could lead to unusual magnetoconductance features, in very good agreement with the TMR-like signal of the experiments in Sec. 8.5.3.

8.7. Outlook: cobalt side gates

The stray field estimates of $B_{stray} \approx 40\text{-}50\text{ mT}$ were below our expectations for the studied Permalloy side gates. Since the geometry of this device was not optimal, we viewed this as a promising step which could be much improved by optimizing the geometry, i.e. reducing the gap between the side gate pairs and increasing the film thickness. Another avenue for improvement is the use of harder ferromagnetic materials like cobalt or iron. The first steps towards new, improved devices have been taken. In the following, preliminary results on a device with cobalt side gates are presented and compared to the Py device.

Cobalt has a saturation magnetization twice as high as Permalloy [209], it is also a much harder magnet as the magnetocrystalline anisotropy is sizeable. Consequently, the magnetization has a built-in preferential orientation and is less susceptible to changes in the geometry of the magnet. This is reflected in the stray field and domain structure measurements in Fig. 8.21. Similarly to Permalloy, the magnetic properties were characterized using magnetic force microscopy (MFM) and X-ray magnetic circular dichroism (XMCD) by Simon Zihlmann and Péter Makk.

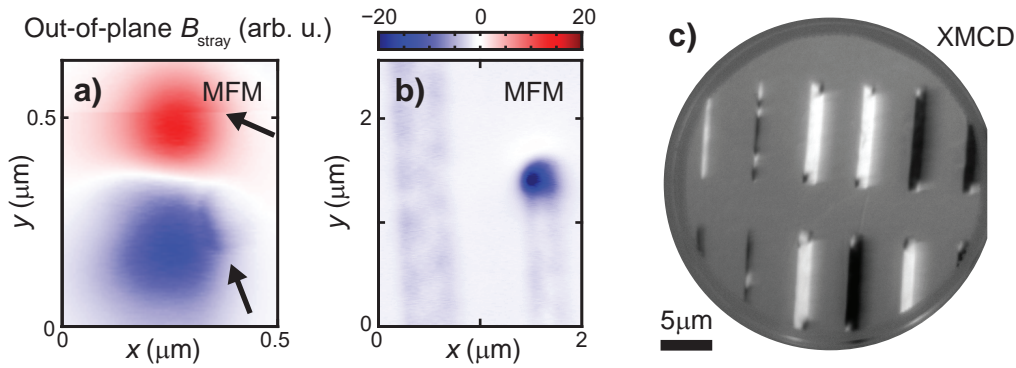


Figure 8.21.: Magnetic properties of cobalt strips | a-b) Magnetic force micrographs of the out-of-plane stray field of a pair of cobalt strips and a single strip, respectively. c) X-ray magnetic circular dichroism images of the magnetization of cobalt strips with different widths.

The spatial distribution of the stray field – measured using MFM – is shown in Fig. 8.21.a-b). We find a stray field pattern similar to that of the Permalloy strips, however some discrepancies are found, as highlighted by arrows in Fig. 8.21.a), indicating non-uniform magnetization of the strips. Unfortunately, comparative measurements of the magnitude of the stray field in Co and Py could not be performed.

This is even more visible in XMCD images of the distribution of the magnetization, probed along the long axis of the strips, shown in Fig. 8.21.c). Once again, the domain structure is found to be dominated by a single, large domain in the bulk. Compared to Permalloy, the formation of closure domains at the tips is more pronounced for wider strips. We also find a more segmented domain structure in the bulk for the narrowest strips. These might be avoidable by the magnetization of the strips with an external field, which could not be performed in the XMCD setup.

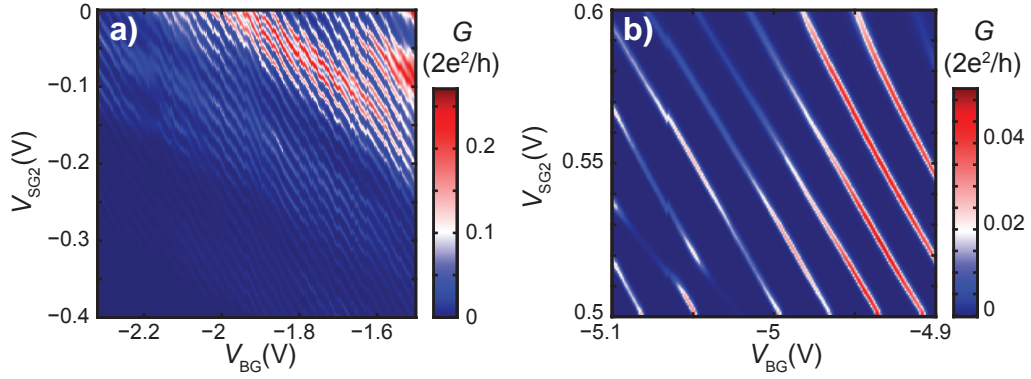


Figure 8.22.: Charge stability diagrams of device with Co side gates as a function of back and one side gate voltage.

Samples were fabricated following the protocol established for Py devices. The magnetoconductance of the sample was recorded in the same setup as the previous experiments. Similarly, the magnetic field is applied along the axis of the side gate strips.

Conductance maps as a function of two gate voltages, shown in Fig. 8.22, reveal Coulomb oscillations, tuned by the back gate and one of the side gates (SG1). The second side gate (SG2) is grounded as it did not exhibit any gating effect, possibly due to a broken contact. Similarly to the Permalloy device, the conductances of the peaks are strongly modulated but the broadening of the resonances was much more prominent. The stability of the device is also noticeably inferior, with charge instabilities and gate jitter clearly observable in Fig. 8.22.a). Frequent charge rearrangements, especially during magnetic field sweeps, significantly restricted the number of comparable measurements and the extent of the studied gate regions, like in Fig. 8.22. We believe that this lack of stability is related to SG1 not working, thus can be improved upon in subsequent samples.

The magnetoconductance of two conductance resonances is presented and examined in Fig. 8.23. The conductance maps in Figs. 8.23.a-d) are evaluated by extracting the maximum conductance, width, and position of the resonances from the gate sweeps recorded at different magnetic fields, for both field sweep directions. A clear hysteresis is encountered between the magnetic field sweeps for both resonances. The maps in Figs. 8.23.a-b) show a clear difference for the sweep directions, with pronounced changes around zero field. The resonance in Fig. 8.23.c-d) shows a similar magnetic signal, although much weaker. Note that the maps in Figs. 8.23.a-b) are measured on a field scale four times larger than in Figs. 8.23.c-d). Unlike the resonances encountered in the Py sample, no sharp changes are observed which would help us identify the coercive field of the strips.

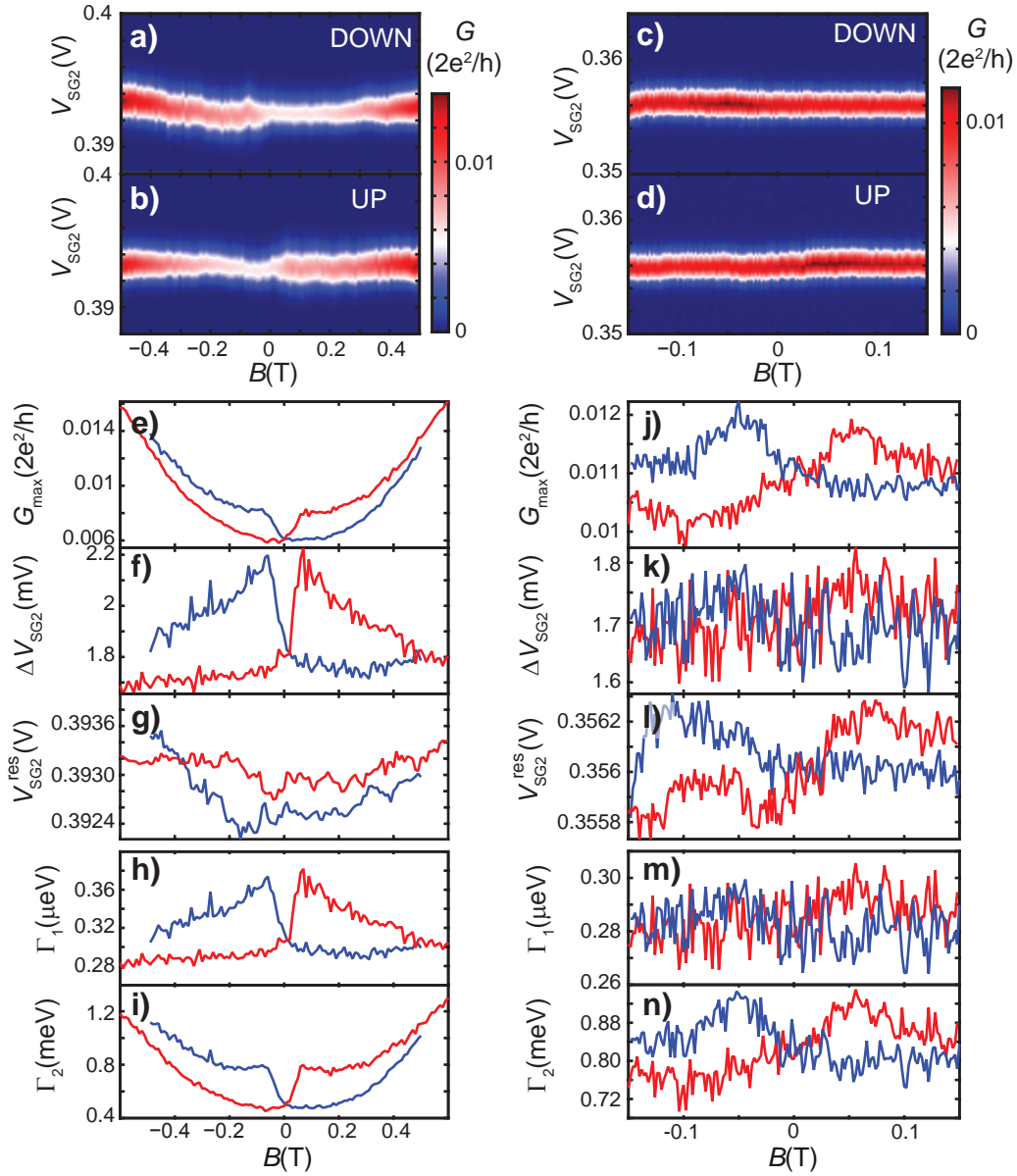


Figure 8.23.: Magnetoconductance of Coulomb resonances in a device with cobalt side gates | a-b) & c-d) Conductance maps as a function of one side gate voltage and the magnetic field for both sweep directions for two different resonances. e-g) & k-m) Magnetic field dependence of resonance amplitude, width, and position, respectively. h-i) & n-o) $\Gamma_{1,2}$ coupling parameters, calculated from the extracted parameters fitting Lorentzian curves to gate traces of the map.

The extracted amplitudes in Fig. 8.23.e) and j) show smooth changes, asymmetric with respect to the sweep direction. As the field changes sign at 0 T, the amplitude increases smoothly up to ± 50 -70 mT, and subsequently starts to converge to the values of the curve measured for the opposite sweep direction, eventually reaching common values at much higher fields (up to ~ 400 mT).

The widths of the resonances are presented in Figs. 8.23.f) and k). We observe a more significant difference for the two examined resonances. The resonance width shows a large ($> 25\%$) increase in Fig. 8.23.f), which seems to vary on the same field scales as the amplitude in Fig. 8.23.e), exhibiting an onset around zero field and a maximum around 50-70 mT, and a gradual decrease, eventually recovering to the initial values. Similarly, in Fig. 8.23.f), the resonance width shows an increase on the same field scale as the changes in the amplitude, however it is barely discernible from the noise. The main variations in the amplitude and width occur below 100 mT, and are on the field scale of the expected $B_c \approx 50$ mT [210], which could not be inferred from the plots as no sharp changes were encountered.

Similarly to the data previously examined for Permalloy side gates, the resonance positions in Figs. 8.23.g) and l) show no systematic and reproducible changes. The random shifts are most probably due to the instability of the electrostatic environment of the quantum dot, which often resulted in irreversible changes and was probably related to SG1 showing no gating action.

The coupling strengths were calculated from the amplitude and width. As before, the low conductance values yield a strong coupling asymmetry, where the variations in width are dominated by the larger Γ_1 , while the changes in the amplitude are reflected in the smaller Γ_2 , shown in Figs. 8.23.h) and m) and Figs. 8.23.i) and n).

The resonance parameters do not show sudden changes, we tentatively attribute the smooth changes in the couplings on a large field scale to the non-uniform magnetization of the Co strips, observed in XMCD measurements. The magnetization of the different domains of the strips might occur at different fields producing considerable variations in the stray field, which can qualitatively account for the characteristics of the observed magnetoconductance.

These results demonstrate magnetotransport features, with a clear hysteresis in the magnetoconductance, due to the ferromagnetic side gates. The lack of stability considerably limited the amount of data that could be evaluated, which was not sufficient to disentangle phenomena originating from the quantum dot and from the magnetic attributes of the Co strip.

Cobalt proved to be a material where the less controlled domain structure of the strips made the examination of magnetoconductance phenomena in the employed geometry quite difficult. This is in sharp contrast to spin-valve structures, e.g. on graphene [210], where the contact area is situated away from the tips, where the single domain in the bulk of the strip is relevant. Here, the tips of the structure are of interest where closure domain formation is prominent. Thus, we perceive Permalloy as a more suitable material for magnetic side gates.

8.8. Conclusions

InAs nanowire quantum dot devices – equipped with a pair of ferromagnetic side gates made of Permalloy and cobalt – were investigated. Different transport regimes were found, which were strongly dependent on the gate configuration.

In some cases, the devices exhibited clear signatures of a double quantum dot, with easily identifiable features belonging to two separate structures. Magnetoresistance was investigated in different positions of the charge stability diagram and a characteristic behaviour could be identified as we were able to distinguish the individual features of the DQD system. Other regions with parallel resonance lines were reminiscent of a single structure, however the multitude of conductance features meant that the identification of a clear cut behaviour was absolutely hampered.

We found exotic magnetoconductance features for certain resonances at gate configurations close to the charge carrier depletion of the nanowire, reminiscent of tunnelling magnetoresistance in spin-valve devices. Spin valves require ferromagnetic contacts, in contrast, our devices are connected by normal, non-magnetic contacts and utilize the stray field of ferromagnetic side gates. We observe large relative changes in conductance, up to $\frac{\Delta G}{G} = \pm 50\%$, which considerably surpasses the few percent values found in carbon nanotube spin valves [15, 16]. Also, in comparison to previous measurements on quantum dot-based spin valves [17], these enhanced values are not a result of a shift in the resonance position but purely a change in the amplitude of resonance.

The findings were further corroborated by simple models of the system, allowing a better understanding of the origin of the phenomena. By considering the tuning of the local density of states at the contact interfaces, we were able to capture the on- and off-triple-point behaviour in the strongly coupled double-dot regime, as well as the typical quadratic magnetoconductance in this regime. The exotic TMR-like behaviour of the weakly coupled double-dot regime could also be accounted for in a second model, in which we examined ground-state transitions in magnetic field sweeps, and how these influence the magnetoconductance.

The stray field still requires considerable improvement, which could be attainable by optimized geometry. The elimination of spurious quantum dots would also aid our understanding of the phenomena in a more simple system. Nanowires with as-grown barriers provide a solution to this problem and can simultaneously lead to more symmetrical couplings.

Preliminary results on a cobalt-based structure are presented, as a viable substitute for the previously discussed Permalloy-based devices with possibly stronger stray fields. These studies provide some promising results, however, no clear advantage could be identified for cobalt, as opposed to Permalloy.

9 Summary and outlook

In this thesis, we investigated multiple facets of magnetoconductance phenomena in InAs nanowire quantum dot systems. Here, we summarize the main results, and discuss further avenues of improvement.

We carried out a thorough study of the orientation dependence of the g factor [34], finding strongly anisotropic behaviour with comparable results to other studies [144]. The reduced g factor values, along with the lack of correlation between the device geometry and the principal axes of the g tensor, lead us to believe that the quantum dot was mainly defined by mesoscopic details, on smaller length scales than the dimensions of the nanowire segment between the contacts. Investigation of the g -factor anisotropy as a function of electric fields, applied using side gates would allow us to examine the effect of slight modifications to the wave function of the quantum dot. This would also shed some light on the confinement of the quantum dot, which would lead to a better comparison of the geometry and the principal axes of the anisotropy.

We introduced a new fabrication process for the creation of quantum dot-based spin valves in nanowires. We created quasi-suspended ferromagnetic contacts on a polymer layer, which solved the problem of discontinuities in electrodes caused by the large difference between the nanowire diameter and film thickness. We characterized the magnetic properties and electrical contact to nanowires, both yielding satisfactory results. Spin-valve signals have not yet been observed, most probably due to the strong coupling of the leads and the quantum dot. Well-defined barriers, of thin oxide layers below the ferromagnetic contacts should solve this problem, however, the combination of the delicate fabrication process and tunnel barriers might prove difficult

The major focus of this thesis was the effect of stray fields on a quantum dot created by nanomagnets in close proximity of the nanowire where the quantum dot is formed. We explored the effect of electrostatic gating in quantum dot devices equipped with normal metal side gates, and developed fabrication procedure required for creating InAs nanowire quantum dot devices with ferromagnetic side gate pairs. This design makes use of both the electrostatic gating and the stray fields stemming from the nanomagnets. The advantage of our new approach using magnetic gate electrodes, is that the ferromagnets are not in contact with the material, as opposed to spin-valve devices. This approach is also expected to be more robust, as it does not hinge on the efficient spin injection and detection, which are very sensitive to the quality of the contact.

We performed proof-of-principle magnetoconductance experiments on devices based on Permalloy, demonstrating the presence of a ~ 50 mT local stray field. Hysteretic magnetoconductance was found in different transport regimes, assigned to changes in

coupling strengths, induced by the magnetic field. Furthermore, exotic spin-valve-like magnetoconductance signals are encountered for certain resonances, exhibiting $\sim 50\%$ changes in conductance.

Our experiments demonstrate first steps in the fabrication of magnetostatic gates for InAs nanowire quantum dot devices. For future devices, larger emphasis should be placed on achieving the near-perpendicular relative alignment of the nanowires and side gates. Our experiments lacked precise control over the formation of the quantum dots, however, the addition of bottom gate arrays might improve control over the potential landscape [173] and allow fine tuning of a double quantum, or the creation of a less extended single quantum dot. However, one should keep in mind that the proximity of the nanomagnet pairs might result in considerable screening of the gates and reduce their efficiency [54, 55]. As-grown barriers are more promising in terms of creating well-defined single [77] or double quantum dots [211], however in-situ tunability of the coupling strengths is considerably limited.

Now we turn to the possible improvements one could make to the nanomagnets, and a possible path of follow-up experiments. An enhancement of the stray field may be achievable with harder magnetic materials (Fe, Co) [209]. Further experiments using such materials would be particularly interesting for studying the effect of the nanomagnet domain structure, and how stray fields created by closure domains affect the quantum dot. In this thesis, we presented preliminary result from the first experiments on a device with cobalt side gate pairs.

Reducing the gap between the strips and slightly increasing their height are expected to lead to improvements in the magnitude of the stray field and homogeneity could be enhanced by the use of a side gate array [40], however, the size of the quantum dot is a limiting factor. A comparison of side gates with different tip geometries [203] could help optimize the stray field and also examine the effect of inhomogeneities in the stray field.

An interesting situation could arise if the two magnetic side gates reversed their magnetization direction at different fields. This can be engineered using strips of different widths, and thus coercive fields. Such a situation would give rise to more exotic stray field patterns and might be interesting in terms of examining the coupling of the magnetizations of the two side gates. Using two pairs of closely spaced side gates could allow better control over the electrostatics of a double dot system as well as the homogeneity of the stray field. Furthermore, two nanomagnet pairs with different coercive fields would allow the identification of the magnetic response of the individual quantum dots.

The realization of theoretically proposed exotic quasiparticles [46–48] may be possible with more elaborate structures, such as large scale arrays of nanomagnets, warranting further studies of the magnetoconductance in semiconducting nanowire devices putting the stray field of nanomagnets to use.

Bibliography

- [1] E. H. Hall, *Amer. J. Math.* **2**, 287 (1879)
- [2] Y. Aharonov and D. Bohm, *Phys. Rev.* **115**, 485 (1959)
- [3] P. Zeeman, *Nature* **55**, 347 (1897)
- [4] M. N. Baibich, J. M. Broto, A. Fert, F. N. Van Dau, F. Petroff, P. Etienne, G. Creuzet, A. Friederich and J. Chazelas, *Phys. Rev. Lett.* **61**, 2472 (1988)
- [5] G. Binasch, P. Grünberg, F. Saurenbach and W. Zinn, *Phys. Rev. B* **39**, 4828 (1989)
- [6] I. Žutić, J. Fabian and S. Das Sarma, *Rev. Mod. Phys.* **76**, 323 (2004)
- [7] D. Ralph and M. Stiles, *J. Magn. Magn. Mater.* **320**, 1190 (2008)
- [8] J. Fabian, A. Matos-Abiague, C. Ertler, P. Stano and I. Zutic, *Acta Phys. Slovaca* **57**, 565 (2007)
- [9] D. D. Awschalom and M. E. Flatté, *Nature Phys.* **3**, 153 (2007)
- [10] S. Datta and B. Das, *Appl. Phys. Lett.* **56**, 665 (1990)
- [11] B. Huang, D. J. Monsma and I. Appelbaum, *Phys. Rev. Lett.* **99**, 177209 (2007)
- [12] D. D. Awschalom, L. C. Bassett, A. S. Dzurak, E. L. Hu and J. R. Petta, *Science* **339**, 1174 (2013)
- [13] L. P. Kouwenhoven, C. M. Marcus, P. L. McEuen, S. Tarucha, R. M. Westervelt and N. S. Wingreen, In L. L. Sohn, L. P. Kouwenhoven and G. Schön (Eds.), *Mesoscopic Electron Transport*, vol. 345 of *NATO ASI Series*, Springer Netherlands, pp. 105–214 (1997)
- [14] L. P. Kouwenhoven, D. G. Austing and S. Tarucha, *Reports on Progress in Physics* **64**, 701 (2001)
- [15] S. Sahoo, T. Kontos, J. Furer, C. Hoffmann, M. Gräber, A. Cottet and C. Schönenberger, *Nature Phys.* **1**, 99 (2005)
- [16] H. Aurich, A. Baumgartner, F. Freitag, A. Eichler, J. Trbovic and C. Schönenberger, *Appl. Phys. Lett.* **97**, 153116 (2010)
- [17] J. Samm, J. Gramich, A. Baumgartner, M. Weiss and C. Schönenberger, *J. Appl. Phys.* **115**, 174309 (2014)

- [18] D. Loss and D. P. DiVincenzo, *Phys. Rev. A* **57**, 120 (1998)
- [19] C. Kloeffer and D. Loss, *Annu. Rev. Condens. Matter Phys.* **4**, 51 (2013)
- [20] L. O. Olsson, C. B. M. Andersson, M. C. Håkansson, J. Kanski, L. Ilver and U. O. Karlsson, *Phys. Rev. Lett.* **76**, 3626 (1996)
- [21] S. Csonka, L. Hofstetter, F. Freitag, S. Oberholzer, C. Schönenberger, T. S. Jespersen, M. Aagesen and J. Nygård, *Nano Lett.* **8**, 3932 (2008)
- [22] R. S. Deacon, Y. Kanai, S. Takahashi, A. Oiwa, K. Yoshida, K. Shibata, K. Hirakawa, Y. Tokura and S. Tarucha, *Phys. Rev. B* **84**, 041302 (2011)
- [23] C. Fasth, A. Fuhrer, L. Samuelson, V. N. Golovach and D. Loss, *Phys. Rev. Lett.* **98**, 266801 (2007)
- [24] S. Takahashi, R. S. Deacon, K. Yoshida, A. Oiwa, K. Shibata, K. Hirakawa, Y. Tokura and S. Tarucha, *Phys. Rev. Lett.* **104**, 246801 (2010)
- [25] S. Nadj-Perge, S. M. Frolov, E. P. A. M. Bakkers and L. P. Kouwenhoven, *Nature* **468**, 1084 (2010)
- [26] J. Klinovaja, P. Stano and D. Loss, *Phys. Rev. Lett.* **109**, 236801 (2012)
- [27] J. Klinovaja and D. Loss, *Phys. Rev. Lett.* **110**, 126402 (2013)
- [28] J. Klinovaja and D. Loss, *Phys. Rev. B* **90**, 045118 (2014)
- [29] B. Braunecker, P. Burset and A. Levy Yeyati, *Phys. Rev. Lett.* **111**, 136806 (2013)
- [30] L. Hofstetter, S. Csonka, J. Nygård and C. Schönenberger, *Nature* **461**, 960 (2009)
- [31] L. Hofstetter, S. Csonka, A. Baumgartner, G. Fülöp, S. d'Hollosy, J. Nygård and C. Schönenberger, *Phys. Rev. Lett.* **107**, 136801 (2011)
- [32] M. D. Schroer, K. D. Petersson, M. Jung and J. R. Petta, *Phys. Rev. Lett.* **107**, 176811 (2011)
- [33] Y. Kato, R. Myers, D. Driscoll, A. Gossard, J. Levy and D. Awschalom, *Science* **299**, 1201 (2003)
- [34] S. d'Hollosy, G. Fábíán, A. Baumgartner, J. Nygård and C. Schönenberger, *AIP Conf. Proc.* **1566**, 359 (2013)
- [35] M. Pioro-Ladrière, Y. Tokura, T. Obata, T. Kubo and S. Tarucha, *Appl. Phys. Lett.* **90**, 024105 (2007)
- [36] M. Pioro-Ladrière, T. Obata, Y. Tokura, Y.-S. Shin, T. Kubo, K. Yoshida, T. Taniyama and S. Tarucha, *Nature Phys.* **4**, 776 (2008)
- [37] T. Obata, M. Pioro-Ladrière, Y. Tokura, Y.-S. Shin, T. Kubo, K. Yoshida, T. Taniyama and S. Tarucha, *Phys. Rev. B* **81**, 085317 (2010)

-
- [38] R. Brunner, Y.-S. Shin, T. Obata, M. Pioro-Ladrière, T. Kubo, K. Yoshida, T. Taniyama, Y. Tokura and S. Tarucha, *Phys. Rev. Lett.* **107**, 146801 (2011)
- [39] X. Wu, D. R. Ward, J. Prance, D. Kim, J. K. Gamble, R. Mohr, Z. Shi, D. Savage, M. Lagally, M. Friesen, S. N. Coppersmith and M. A. Eriksson, *Proc. Natl. Acad. Sci. U.S.A.* **111**, 11938 (2014)
- [40] R. P. G. McNeil, R. J. Schneble, M. Kataoka, C. J. B. Ford, T. Kasama, R. E. Dunin-Borkowski, J. M. Feinberg, R. J. Harrison, C. H. W. Barnes, D. H. Y. Tse, T. Trypiniotis, J. A. C. Bland, D. Anderson, G. A. C. Jones and M. Pepper, *Nano Lett.* **10**, 1549 (2010)
- [41] J. Alicea, *Rep. Prog. Phys.* **75**, 076501 (2012)
- [42] V. Mourik, K. Zuo, S. Frolov, S. Plissard, E. Bakkers and L. Kouwenhoven, *Science* **336**, 1003 (2012)
- [43] M. Deng, C. Yu, G. Huang, M. Larsson, P. Caroff and H. Xu, *Nano Lett.* **12**, 6414 (2012)
- [44] A. Das, Y. Ronen, M. Heiblum, D. Mahalu, A. V. Kretinin and H. Shtrikman, *Nat. Commun.* **3**, 1165 (2012)
- [45] H. O. H. Churchill, V. Fatemi, K. Grove-Rasmussen, M. T. Deng, P. Caroff, H. Q. Xu and C. M. Marcus, *Phys. Rev. B* **87**, 241401 (2013)
- [46] D. Rainis, A. Saha, J. Klinovaja, L. Trifunovic and D. Loss, *Phys. Rev. Lett.* **112**, 196803 (2014)
- [47] D. Rainis and D. Loss, *Phys. Rev. B* **90**, 235415 (2014)
- [48] A. Saha, D. Rainis, R. P. Tiwari and D. Loss, *Phys. Rev. B* **90**, 035422 (2014)
- [49] P. Recher, E. V. Sukhorukov and D. Loss, *Phys. Rev. B* **63**, 165314 (2001)
- [50] G. B. Lesovik, T. Martin and G. Blatter, *Eur. Phys. J. B* **24**, 287 (2001)
- [51] A. Kleine, A. Baumgartner, J. Trbovic and C. Schönenberger, *Europhys. Lett.* **87**, 27011 (2009)
- [52] L. G. Herrmann, F. Portier, P. Roche, A. Levy Yeyati, T. Kontos and C. Strunk, *Phys. Rev. Lett.* **104**, 026801 (2010)
- [53] J. Schindele, A. Baumgartner and C. Schönenberger, *Phys. Rev. Lett.* **109**, 157002 (2012)
- [54] S. d'Hollosy, *Locally Tunable InAs Nanowire Quantum Dots for Cooper Pair Splitting*. Ph.D. thesis, University of Basel (2014)
- [55] G. Fülöp, S. d'Hollosy, A. Baumgartner, P. Makk, V. Guzenko, M. Madsen, J. Nygård, C. Schönenberger and S. Csonka, *Phys. Rev. B* **90**, 235412 (2014)

- [56] G. Fülöp, F. Domínguez, S. d'Hollosy, A. Baumgartner, P. Makk, M. H. Madsen, V. A. Guzenko, J. Nygård, C. Schönenberger, A. Levy Yeyati and S. Csonka, *Phys. Rev. Lett.* **115**, 227003 (2015)
- [57] S. Kawabata, *J. Phys. Soc. Jpn.* **70**, 1210 (2001)
- [58] O. Malkoc, C. Bergenfeldt and P. Samuelsson, *Europhys. Lett.* **105**, 47013 (2014)
- [59] W. Kłobus, A. Grudka, A. Baumgartner, D. Tomaszewski, C. Schönenberger and J. Martinek, *Phys. Rev. B* **89**, 125404 (2014)
- [60] A. Cottet, *Phys. Rev. B* **86**, 075107 (2012)
- [61] A. Cottet, T. Kontos and A. Levy Yeyati, *Phys. Rev. Lett.* **108**, 166803 (2012)
- [62] Z. Scherübl, A. Pályi and S. Csonka, *Phys. Rev. B* **89**, 205439 (2014)
- [63] E. C. Stoner and E. P. Wohlfarth, *Phil. Trans. R. Soc. Lond. A* **240**, 599 (1948)
- [64] T. McGuire and R. Potter, *IEEE Trans. Magn.* **11**, 1018 (1975)
- [65] G. Dresselhaus, *Phys. Rev.* **100**, 580 (1955)
- [66] M. Julliere, *Phys. Lett. A* **54**, 225 (1975)
- [67] S. S. Parkin, C. Kaiser, A. Panchula, P. M. Rice, B. Hughes, M. Samant and S.-H. Yang, *Nature Mater.* **3**, 862 (2004)
- [68] S. Yuasa, T. Nagahama, A. Fukushima, Y. Suzuki and K. Ando, *Nature Mater.* **3**, 868 (2004)
- [69] S. Ikeda, J. Hayakawa, Y. Ashizawa, Y. M. Lee, K. Miura, H. Hasegawa, M. Tsunoda, F. Matsukura and H. Ohno, *Appl. Phys. Lett.* **93**, 082508 (2008)
- [70] T. Ihn, *Semiconductor Nanostructures*. Oxford University Press (2009)
- [71] C. W. J. Beenakker, *Phys. Rev. B* **44**, 1646 (1991)
- [72] R. Hanson, L. P. Kouwenhoven, J. R. Petta, S. Tarucha and L. M. K. Vandersypen, *Rev. Mod. Phys.* **79**, 1217 (2007)
- [73] Y. Meir, N. S. Wingreen and P. A. Lee, *Phys. Rev. Lett.* **70**, 2601 (1993)
- [74] S. M. Cronenwett, T. H. Oosterkamp and L. P. Kouwenhoven, *Science* **281**, 540 (1998)
- [75] A. Kogan, S. Amasha, D. Goldhaber-Gordon, G. Granger, M. A. Kastner and H. Shtrikman, *Phys. Rev. Lett.* **93**, 166602 (2004)
- [76] L. M. Roth, B. Lax and S. Zwerdling, *Phys. Rev.* **114**, 90 (1959)
- [77] M. T. Björk, A. Fuhrer, A. E. Hansen, M. W. Larsson, L. E. Fröberg and L. Samuelson, *Phys. Rev. B* **72**, 201307 (2005)

- [78] C. E. Pryor and M. E. Flatté, *Phys. Rev. Lett.* **96**, 026804 (2006)
- [79] A. De and C. E. Pryor, *Phys. Rev. B* **76**, 155321 (2007)
- [80] E. E. Vdovin, A. Levin, A. Patanè, L. Eaves, P. C. Main, Y. N. Khanin, Y. V. Dubrovskii, M. Henini and G. Hill, *Science* **290**, 122 (2000)
- [81] A. Patanè, R. J. A. Hill, L. Eaves, P. C. Main, M. Henini, M. L. Zambrano, A. Levin, N. Mori, C. Hamaguchi, Y. V. Dubrovskii, E. E. Vdovin, D. G. Austing, S. Tarucha and G. Hill, *Phys. Rev. B* **65**, 165308 (2002)
- [82] K. Ono, H. Shimada and Y. Ootuka, *J. Phys. Soc. Jpn.* **67**, 2852 (1998)
- [83] H. Shimada, K. Ono and Y. Ootuka, *J. Appl. Phys.* **93**, 8259 (2003)
- [84] S. J. van der Molen, N. Tombros and B. J. van Wees, *Phys. Rev. B* **73**, 220406 (2006)
- [85] K. A. Matveev, L. I. Glazman and H. U. Baranger, *Phys. Rev. B* **54**, 5637 (1996)
- [86] C. Thelander, P. Agarwal, S. Brongersma, J. Eymery, L. F. Feiner, A. Forchel, M. Scheffler, W. Riess, B. J. Ohlsson, U. Gösele and L. Samuelson, *Materials Today* **9**, 28 (2006)
- [87] W. Lu and C. M. Lieber, *J. Phys. D: Appl. Phys.* **39**, R387 (2006)
- [88] J. Du, D. Liang, H. Tang and X. P. Gao, *Nano Lett.* **9**, 4348 (2009)
- [89] P. Offermans, M. Crego-Calama and S. H. Brongersma, *Nano Lett.* **10**, 2412 (2010)
- [90] J. Bao, M. A. Zimmler, F. Capasso, X. Wang and Z. Ren, *Nano Lett.* **6**, 1719 (2006)
- [91] J. Law and J. Thong, *Appl. Phys. Lett.* **88**, 133114 (2006)
- [92] A. B. Greytak, C. J. Barrelet, Y. Li and C. M. Lieber, *Appl. Phys. Lett.* **87**, 151103 (2005)
- [93] S. A. Dayeh, D. P. Aplin, X. Zhou, P. K. Yu, E. T. Yu and D. Wang, *Small* **3**, 326 (2007)
- [94] S. A. Dayeh, C. Soci, P. K. L. Yu, E. T. Yu and D. Wang, *Journal of Vacuum Science & Technology B* **25**, 1432 (2007)
- [95] A. Konar, J. Mathew, K. Nayak, M. Bajaj, R. K. Pandey, S. Dhara, K. V. R. M. Murali and M. M. Deshmukh, *Nano Lett.* **15**, 1684 (2015)
- [96] T. Bryllert, L.-E. Wernersson, L. Froberg and L. Samuelson, *Electron Device Letters, IEEE* **27**, 323 (2006)
- [97] M. Egard, S. Johansson, A.-C. Johansson, K.-M. Persson, A. W. Dey, B. M. Borg, C. Thelander, L.-E. Wernersson and E. Lind, *Nano Lett.* **10**, 809 (2010)

- [98] A. M. Burke, D. J. Carrad, J. G. Gluschke, K. Storm, S. Fahlvik Svensson, H. Linke, L. Samuelson and A. P. Micolich, *Nano Lett.* **15**, 2836 (2015)
- [99] A. C. Ford, J. C. Ho, Y.-L. Chueh, Y.-C. Tseng, Z. Fan, J. Guo, J. Bokor and A. Javey, *Nano Lett.* **9**, 360 (2009)
- [100] Y.-L. Chueh, A. C. Ford, J. C. Ho, Z. A. Jacobson, Z. Fan, C.-Y. Chen, L.-J. Chou and A. Javey, *Nano Lett.* **8**, 4528 (2008)
- [101] S. De Franceschi, L. Kouwenhoven, C. Schönenberger and W. Wernsdorfer, *Nature Nanotech.* **5**, 703 (2010)
- [102] Y.-J. Doh, J. A. van Dam, A. L. Roest, E. P. Bakkers, L. P. Kouwenhoven and S. De Franceschi, *Science* **309**, 272 (2005)
- [103] L. Hofstetter, A. Geresdi, M. Aagesen, J. Nygård, C. Schönenberger and S. Csonka, *Phys. Rev. Lett.* **104**, 246804 (2010)
- [104] S. Nadj-Perge, V. S. Pribiag, J. W. G. van den Berg, K. Zuo, S. R. Plissard, E. P. A. M. Bakkers, S. M. Frolov and L. P. Kouwenhoven, *Phys. Rev. Lett.* **108**, 166801 (2012)
- [105] R. S. Wagner and W. C. Ellis, *Appl. Phys. Lett.* **4**, 89 (1964)
- [106] R. S. Wagner and W. C. Ellis, *Transactions of the Metallurgical Society of AIME* **233**, 1053 (1965)
- [107] M. Madsen, M. Aagesen, P. Krogstrup, C. Sørensen and J. Nygård, *Nanoscale Research Letters* **6**, 516 (2011)
- [108] M. H. Madsen, *Indium Arsenide Nanowires: Fabrication, Characterization, and Biological Applications*. Ph.D. thesis, University of Copenhagen (2012)
- [109] M. E. Messing, K. Hillerich, J. Johansson, K. Deppert and K. A. Dick, *Gold Bulletin* **42**, 172 (2009)
- [110] M. Aagesen, *MBE Grown Nanorods and Nanoplates*. Ph.D. thesis, University of Copenhagen (2007)
- [111] M. T. Björk, B. J. Ohlsson, T. Sass, A. I. Persson, C. Thelander, M. H. Magnusson, K. Deppert, L. R. Wallenberg and L. Samuelson, *Appl. Phys. Lett.* **80**, 1058 (2002)
- [112] C. Thelander, M. T. Björk, M. W. Larsson, A. E. Hansen, L. R. Wallenberg and L. Samuelson, *Solid State Commun.* **131**, 573 (2004)
- [113] Ö. Gül, N. Demarina, C. Blömers, T. Rieger, H. Lüth, M. I. Lepsa, D. Grützmacher and T. Schäpers, *Phys. Rev. B* **89**, 045417 (2014)
- [114] Ö. Gül, H. Y. Günel, H. Lüth, T. Rieger, T. Wenz, F. Haas, M. Lepsa, G. Panaitov, D. Grützmacher and T. Schäpers, *Nano Lett.* **14**, 6269 (2014)

-
- [115] <http://education.mrsec.wisc.edu/pmk/pages/ZnS.html>
- [116] http://upload.wikimedia.org/wikipedia/commons/8/8e/Wurtzite_polyhedra.png
- [117] K. A. Dick, C. Thelander, L. Samuelson and P. Caroff, *Nano Lett.* **10**, 3494 (2010)
- [118] C. Thelander, P. Caroff, S. Plissard, A. W. Dey and K. A. Dick, *Nano Lett.* **11**, 2424 (2011)
- [119] M. D. Schroer and J. R. Petta, *Nano Lett.* **10**, 1618 (2010)
- [120] H. Shtrikman, R. Popovitz-Biro, A. Kretinin, L. Houben, M. Heiblum, M. Bukala, M. Galicka, R. Buczko and P. Kacman, *Nano Lett.* **9**, 1506 (2009)
- [121] M. H. Madsen, P. Krogstrup, E. Johnson, S. Venkatesan, E. Mühlbauer, C. Scheu, C. B. Sørensen and J. Nygård, *J. Cryst. Growth* **364**, 16 (2013)
- [122] S. Upadhyay, T. S. Jespersen, M. H. Madsen, P. Krogstrup and J. Nygård, *Appl. Phys. Lett.* **103**, 162104 (2013)
- [123] C. Blömers, *Electronic Transport in Narrow-Gap Semiconductor Nanowires*. Ph.D. thesis, RWTH Aachen University (2012)
- [124] S. Chuang, Q. Gao, R. Kapadia, A. C. Ford, J. Guo and A. Javey, *Nano Lett.* **13**, 555 (2013)
- [125] A. C. Ford, S. B. Kumar, R. Kapadia, J. Guo and A. Javey, *Nano Lett.* **12**, 1340 (2012)
- [126] F. Vigneau, V. Prudkovkiy, I. Duchemin, W. Escoffier, P. Caroff, Y.-M. Niquet, R. Leturcq, M. Goiran and B. Raquet, *Phys. Rev. Lett.* **112**, 076801 (2014)
- [127] G. W. Holloway, D. Shiri, C. M. Haapamaki, K. Willick, G. Watson, R. R. LaPierre and J. Baugh, *Phys. Rev. B* **045422**, 045422 (2015)
- [128] S. Estévez Hernández, M. Akabori, K. Sladek, C. Volk, S. Alagha, H. Hardtdegen, M. G. Pala, N. Demarina, D. Grützmacher and T. Schäpers, *Phys. Rev. B* **82**, 235303 (2010)
- [129] I. van Weperen, B. Tarasinski, D. Eeltink, V. S. Pribiag, S. R. Plissard, E. P. A. M. Bakkers, L. P. Kouwenhoven and M. Wimmer, *Phys. Rev. B* **91**, 201413 (2015)
- [130] M. Scheffler, S. Nadj-Perge, L. P. Kouwenhoven, M. T. Borgström and E. P. a. M. Bakkers, *J. Appl. Phys.* **106**, 124303 (2009)
- [131] C. Blömers, M. I. Lepsa, M. Luysberg, D. Grützmacher, H. Lüth and T. Schäpers, *Nano Lett.* **11**, 3550 (2011)
- [132] T. Wenz, M. Rosien, F. Haas, T. Rieger, N. Demarina, M. I. Lepsa, H. Lüth, D. Grützmacher and T. Schäpers, *Appl. Phys. Lett.* **105**, 113111 (2014)

- [133] T. Richter, C. Blömers, H. Lüth, R. Calarco, M. Indlekofer, M. Marso and T. Schäpers, *Nano Lett.* **8**, 2834 (2008)
- [134] T. S. Jespersen, J. R. Hauptmann, C. B. Sørensen and J. Nygård, *Phys. Rev. B* **91**, 041302 (2015)
- [135] A. Hansen, M. Björk, C. Fasth, C. Thelander and L. Samuelson, *Phys. Rev. B* **71**, 205328 (2005)
- [136] S. Dhara, H. Solanki, V. Singh, A. Narayanan, P. Chaudhari, M. Gokhale, A. Bhattacharya and M. Deshmukh, *Phys. Rev. B* **79**, 121311 (2009)
- [137] P. Roulleau, T. Choi, S. Riedi, T. Heinzl, I. Shorubalko, T. Ihn and K. Ensslin, *Phys. Rev. B* **81**, 155449 (2010)
- [138] D. Liang and X. P. A. Gao, *Nano Lett.* **12**, 3263 (2012)
- [139] Z. Scherübl, *Weak Localization in InAs Nanoelectronic Circuits*. Master's thesis, Budapest University of Technology and Economics (2012)
- [140] A. Pfund, I. Shorubalko, K. Ensslin and R. Leturcq, *Phys. Rev. B* **76**, 161308 (2007)
- [141] Y. Kanai, R. S. Deacon, S. Takahashi, A. Oiwa, K. Yoshida, K. Shibata, K. Hirakawa, Y. Tokura and S. Tarucha, *Nature Nanotech.* **6**, 511 (2011)
- [142] S. Nadj-Perge, S. M. Frolov, J. W. W. van Tilburg, J. Danon, Y. Nazarov, R. Algra, E. P. A. M. Bakkers and L. P. Kouwenhoven, *Phys. Rev. Lett.* **81**, 201305 (2010)
- [143] E. Rashba, *Sov. Phys. Solid State* **1**, 368 (1959)
- [144] S. Takahashi, R. S. Deacon, A. Oiwa, K. Shibata, K. Hirakawa and S. Tarucha, *Phys. Rev. B* **87**, 161302 (2013)
- [145] R. A. Lai, H. O. H. Churchill and C. M. Marcus, *Phys. Rev. B* **89**, 121303 (2014)
- [146] Zeonrex and Zeon Corporation, ZEP520A Technical Report. <https://www.zeonchemicals.com/pdfs/ZEP520A.pdf> (2010)
- [147] D. B. Suyatin, C. Thelander, M. T. Björk, I. Maximov and L. Samuelson, *Nanotechnology* **18**, 105307 (2007)
- [148] M. J. L. Sourribes, I. Isakov, M. Panfilova and P. A. Warburton, *Nanotechnology* **24**, 045703 (2013)
- [149] Ö. Gül, D. J. van Woerkom, I. van Weperen, D. Car, S. R. Plissard, E. P. A. M. Bakkers and L. P. Kouwenhoven, *Nanotechnology* **26**, 215202 (2015)
- [150] A. A. Kiselev, E. L. Ivchenko and U. Rössler, *Phys. Rev. B* **58**, 16353 (1998)
- [151] F. H. L. Koppens, C. Buizert, I. T. Vink, K. C. Nowack, T. Meunier, L. P. Kouwenhoven and L. M. K. Vandersypen, *J. Appl. Phys.* **101**, 081706 (2007)

-
- [152] H. A. Nilsson, P. Caroff, C. Thelander, M. Larsson, J. B. Wagner, L.-E. Wernersson, L. Samuelson and H. Q. Xu, *Nano Lett.* **9**, 3151 (2009)
- [153] V. N. Golovach, M. Borhani and D. Loss, *Phys. Rev. B* **74**, 165319 (2006)
- [154] J. van Bree, A. Y. Silov, P. M. Koenraad, M. E. Flatté and C. E. Pryor, *Phys. Rev. B* **85**, 165323 (2012)
- [155] R. Zielke, F. Maier and D. Loss, *Phys. Rev. B* **89**, 115438 (2014)
- [156] I. Hapke-Wurst, U. Zeitler, R. Haug and K. Pierz, *Physica E* **12**, 802 (2002)
- [157] T. P. M. Alegre, F. G. G. Hernández, A. L. C. Pereira and G. Medeiros-Ribeiro, *Phys. Rev. Lett.* **97**, 236402 (2006)
- [158] B. J. Witek, R. W. Heeres, U. Perinetti, E. P. A. M. Bakkers, L. P. Kouwenhoven and V. Zwiller, *Phys. Rev. B* **84**, 195305 (2011)
- [159] M. Buitelaar, T. Nussbaumer and C. Schönenberger, *Phys. Rev. Lett.* **89**, 256801 (2002)
- [160] A. Eichler, M. Weiss, S. Oberholzer, C. Schönenberger, A. L. Yeyati, J. Cuevas and A. Martín-Rodero, *Phys. Rev. Lett.* **99**, 126602 (2007)
- [161] T. S. Jespersen, J. Paaske, B. M. Andersen, K. Grove-Rasmussen, H. I. Jørgensen, M. Aagesen, C. B. Sørensen, P. Lindelof, K. Flensberg and J. Nygård, *Phys. Rev. Lett.* **99**, 126603 (2007)
- [162] R. Deacon, Y. Tanaka, A. Oiwa, R. Sakano, K. Yoshida, K. Shibata, K. Hirakawa and S. Tarucha, *Phys. Rev. B* **81**, 121308 (2010)
- [163] K. Franke, G. Schulze and J. Pascual, *Science* **332**, 940 (2011)
- [164] K. Grove-Rasmussen, H. I. Jørgensen, B. M. Andersen, J. Paaske, T. S. Jespersen, J. Nygård, K. Flensberg and P. E. Lindelof, *Phys. Rev. B* **79**, 134518 (2009)
- [165] B. M. Andersen, K. Flensberg, V. Koerting and J. Paaske, *Phys. Rev. Lett.* **107**, 256802 (2011)
- [166] V. Koerting, B. M. Andersen, K. Flensberg and J. Paaske, *Phys. Rev. B* **82**, 245108 (2010)
- [167] J. E. Moore and X.-G. Wen, *Phys. Rev. Lett.* **85**, 1722 (2000)
- [168] J. S. Lee, J.-W. Park, J. Y. Song and J. Kim, *Nanotechnology* **24**, 195201 (2013)
- [169] A. Dirnaichner, M. Grifoni, A. Prüfling, D. Steininger, A. K. Hüttel and C. Strunk, *Phys. Rev. B* **91**, 195402 (2015)
- [170] K. Hamaya, M. Kitabatake, K. Shibata, M. Jung, M. Kawamura, K. Hirakawa, T. Machida, T. Taniyama, S. Ishida and Y. Arakawa, *Appl. Phys. Lett.* **91**, 022107 (2007)

- [171] K. Hamaya, S. Masubuchi, M. Kawamura, T. Machida, M. Jung, K. Shibata, K. Hirakawa, T. Taniyama, S. Ishida and Y. Arakawa, *Appl. Phys. Lett.* **90**, 053108 (2007)
- [172] K. Hamaya, M. Kitabatake, K. Shibata, M. Jung, M. Kawamura, S. Ishida, T. Taniyama, K. Hirakawa, Y. Arakawa and T. Machida, *Appl. Phys. Lett.* **93**, 222107 (2008)
- [173] C. Fasth, A. Fuhrer, M. T. Björk and L. Samuelson, *Nano Lett.* **5**, 1487 (2005)
- [174] A. Fuhrer, C. Fasth and L. Samuelson, *Appl. Phys. Lett.* **91**, 052109 (2007)
- [175] F. Giazotto, P. Spathis, S. Roddaro, S. Biswas, F. Taddei, M. Governale and L. Sorba, *Nature Phys.* **7**, 857 (2011)
- [176] S. d’Hollosy, M. Jung, A. Baumgartner, V. A. Guzenko, M. H. Madsen, J. Nygård and C. Schönenberger, *Nano Lett.* **15**, 4585 (2015)
- [177] E.-S. Liu, J. Nah, K. M. Varahramyan and E. Tutuc, *Nano Lett.* **10**, 3297 (2010)
- [178] J. Tarun, S. Huang, Y. Fukuma, H. Idzuchi, Y. Otani, N. Fukata, K. Ishibashi and S. Oda, *J. Appl. Phys.* **109**, 07C508 (2011)
- [179] S. Zhang, S. A. Dayeh, Y. Li, S. A. Crooker, D. L. Smith and S. T. Picraux, *Nano Lett.* **13**, 430 (2013)
- [180] O. van’t Erve, A. Friedman, C. Li, J. Robinson, J. Connell, L. Lauhon and B. Jonker, *Nat. Commun.* **6**, 7541 (2015)
- [181] S. Heedt, C. Morgan, K. Weis, D. E. Bürgler, R. Calarco, H. Hardtdegen, D. Grützmacher and T. Schüpers, *Nano Lett.* **12**, 4437 (2012)
- [182] F. Zwanenburg, D. Van der Mast, H. Heersche, L. Kouwenhoven and E. Bakkers, *Nano Lett.* **9**, 2704 (2009)
- [183] P. Rickhaus, R. Maurand, M.-H. Liu, M. Weiss, K. Richter and C. Schönenberger, *Nat. Commun.* **4**, 2342 (2013)
- [184] R. Maurand, P. Rickhaus, P. Makk, S. Hess, E. Tóvari, C. Handschin, M. Weiss and C. Schönenberger, *Carbon* **79**, 486 (2014)
- [185] N. Tombros, A. Veligura, J. Junesch, J. Jasper van den Berg, P. J. Zomer, M. Wojtaszek, I. J. Vera Marun, H. T. Jonkman and B. J. van Wees, *J. Appl. Phys.* **109**, 093702 (2011)
- [186] K. Storm, F. Halvardsson, M. Heurlin, D. Lindgren, A. Gustafsson, P. M. Wu, B. Monemar and L. Samuelson, *Nature Nanotech.* **7**, 718 (2012)
- [187] W. Liang, M. P. Shores, M. Bockrath, J. R. Long and H. Park, *Nature* **417**, 725 (2002)

-
- [188] A. V. Kretinin, R. Popovitz-Biro, D. Mahalu and H. Shtrikman, *Nano Lett.* **10**, 3439 (2010)
- [189] A. N. Pasupathy, R. C. Bialczak, J. Martinek, J. E. Grose, L. A. Donev, P. L. McEuen and D. C. Ralph, *Science* **306**, 86 (2004)
- [190] J. Martinek, M. Sindel, L. Borda, J. Barnaś, R. Bulla, J. König, G. Schön, S. Maekawa and J. von Delft, *Phys. Rev. B* **72**, 121302 (2005)
- [191] K. Hamaya, M. Kitabatake, K. Shibata, M. Jung, M. Kawamura, K. Hirakawa, T. Machida, T. Taniyama, S. Ishida and Y. Arakawa, *Appl. Phys. Lett.* **91**, 232105 (2007)
- [192] J. R. Hauptmann, J. Paaske and P. E. Lindelof, *Nature Phys.* **4**, 373 (2008)
- [193] M. Gaaß, A. K. Hüttel, K. Kang, I. Weymann, J. Von Delft and C. Strunk, *Phys. Rev. Lett.* **107**, 176808 (2011)
- [194] S. Roddaro, A. Pescaglioni, D. Ercolani, L. Sorba and F. Beltram, *Nano Lett.* **11**, 1695 (2011)
- [195] L. Romeo, S. Roddaro, A. Pitanti, D. Ercolani, L. Sorba and F. Beltram, *Nano Lett.* **12**, 4490 (2012)
- [196] F. Rossella, D. Ercolani, L. Sorba, F. Beltram and S. Roddaro, *J. Phys. D: Appl. Phys.* **47**, 394015 (2014)
- [197] F. Rossella, A. Bertoni, D. Ercolani, M. Rontani, L. Sorba, F. Beltram and S. Roddaro, *Nature Nanotech.* **9**, 997 (2014)
- [198] R. Winkler, *Spin–Orbit Coupling Effects in Two-Dimensional Electron and Hole Systems*. Springer Tracts in Modern Physics, Springer, Berlin (2003)
- [199] A. De and C. E. Pryor, *Phys. Rev. B* **81**, 155210 (2010)
- [200] G. A. Intronati, P. I. Tamborenea, D. Weinmann and R. A. Jalabert, *Phys. Rev. B* **88**, 045303 (2013)
- [201] J. J. He, T. K. Ng, P. A. Lee and K. T. Law, *Phys. Rev. Lett.* **112**, 037001 (2014)
- [202] H. Kosaka, A. Kiselev, F. Baron, K. W. Kim and E. Yablonovitch, *Electron. Lett* **37**, 464 (2001)
- [203] D. Preusche, S. Schmidmeier, E. Pallecchi, C. Dietrich, A. K. Hüttel, J. Zweck and C. Strunk, *J. Appl. Phys.* **106**, 084314 (2009)
- [204] K. Weis, S. Wirths, A. Winden, K. Sladek, H. Hardtdegen, H. Lüth, D. Grützmacher and T. Schäpers, *Nanotechnology* **25**, 135203 (2014)
- [205] A. Zhukov, C. Volk, A. Winden, H. Hardtdegen and T. Schäpers, *JETP Lett.* **100**, 32 (2014)

- [206] A. K. Hüttel, S. Ludwig, H. Lorenz, K. Eberl and J. P. Kotthaus, *Phys. Rev. B* **72**, 081310 (2005)
- [207] G. Petersen, E. A. Hoffmann, D. Schuh, W. Wegscheider, G. Giedke and S. Ludwig, *Phys. Rev. Lett.* **110**, 177602 (2013)
- [208] F. Forster, M. Mühlbacher, D. Schuh, W. Wegscheider and S. Ludwig, *Phys. Rev. B* **91**, 195417 (2015)
- [209] S. P. Dash, S. Sharma, J. C. Le Breton, J. Peiro, H. Jaffrès, J.-M. George, A. Lemaître and R. Jansen, *Phys. Rev. B* **84**, 054410 (2011)
- [210] N. Tombros, C. Jozsa, M. Popinciuc, H. T. Jonkman and B. J. Van Wees, *Nature* **448**, 571 (2007)
- [211] A. Fuhrer, L. E. Fröberg, J. N. Pedersen, M. W. Larsson, A. Wacker, M.-E. Pistol and L. Samuelson, *Nano Lett.* **7**, 243 (2007)

A Fabrication Recipes

A.1. Wafer Characteristics

- *Substrate material* Si
- *Dopant* *p*-type, boron
- *Resistivity* 0.003 - 0.005 Ωm
- *Capping layer* 400 nm silicon oxide

A.2. Wafer Cleaning

1. Sonicate in acetone for 8 min, rinse and blow dry
2. Sonicate in deionized water for 6 min, rinse and blow dry
3. Sonicate in IPA for 6 min, rinse and blow dry
4. UV/ozone treatment for 10 min (Model 42-220, Jelight Company, USA)

Even then some particles sometimes remained which are likely to be Si debris from the dicing of the wafer. Therefore, care should be taken when the wafers are scratched and cut that the little debris is generated or it is taken up in liquid. The aqueous sonication steps tends to remove them, though.

A.3. EBL Process for PMMA

- *Resist* PMMA 950K diluted with chlorobenzene
- *Spin coating* 4000 rpm yielding a thickness of 350 nm
- *Hardening* 5 min on the hotplate at 180°C
- *Exposure parameters* 220 $\mu\text{C}/\text{cm}^2$ at 20 kV and
~ 17 mm working distance with 8 nm step size
- *Developer* 3:1 isopropyl alcohol (IPA) / methyl isobutyl ketone (MIBK) for 90 s
- *Lift-off* warm acetone

A.4. EBL Process using ZEP

- *Resist* ZEP 520K (ZEON chemicals) diluted with anisol
- *Spin coating* 4000 rpm yielding a thickness of 300 nm
- *Hardening* 3 min on the hotplate at 180°C
- *Exposure parameters* 33 – 37 $\mu\text{C}/\text{cm}^2$ and 500 – 525 pC/cm area and line doses at 10 kV and ~ 17 mm working distance
- *Developer* pure pentyl acetate for 60 s, 1:9 isopropyl alcohol (IPA) / methyl isobutyl ketone (MIBK) for 10 s, rinsing with isopropyl alcohol (IPA)
- *Lift-off* 80°C N-methyl-2-pyrrolidione (NMP) for 15 min and 50° acetone, rinsing in IPA

A.5. O₂ Plasma cleaning

- *Base pressure* 5×10^{-5} mbar
- *O₂ flow* 16%
- *Process pressure* 250 mTorr
- *RF Power* 30 W
- *Exposure time* 35 - 50 s for resist removal and up to 2 min for general cleaning

A.6. Argon Ion Beam Milling

The Ar⁺ sputtering could be done in different evaporation systems in-situ
 For the Balzers system:

- *Base pressure* 2×10^{-6} mbar
- *Ar flow* 3.2 sccm
- *Process background pressure* 1×10^{-4} mbar
- *Ar Plasma* Recipe 2
- *Ar Beam Current* 20 mA
- *Ar Beam Voltage* 500 V
- *Exposure time* 10 - 20 s

For the Bestec system:

- *Base pressure* 7×10^{-6} mbar
- *Ar flow* Needle valve adjusted to give steady process pressure
- *Process pressure* 5×10^{-5} mbar
- *Plasma Power (Magnetron)* Adjust voltage that output current is at 20 mA
- *Extraction voltage* -0.6 kV
- *Anode Voltage* 1 kV
- *Exposure time* 2 – 3.5 min

Curriculum Vitae

Gábor Fábán

Born on July 2, 1987 in Subotica, Yugoslavia.

Education

- 2002–2006 *Matura, Fazekas Mihály Fővárosi Gyakorló Általános Iskola és Gimnázium (Budapest, HU)*
- 2006–2009 *Bachelor of Science in Physics at the Budapest University of Technology and Economics (Budapest, HU)*
- 2009–2011 *Master of Science in Physics at the Budapest University of Technology and Economics (Budapest, HU)*
Master thesis on “Electron Spin Resonance Spectroscopy on Graphite Intercalation Compounds”
- 2011–2015 *PhD in Experimental Physics at the University of Basel (Basel, CH)*
Dissertation in the group of Prof. C. Schönberger: “Engineered Magnetoconductance in InAs Nanowire Quantum Dots”

Positions

- 2007 *Summer Internship at EPFL (L. Forró group)*
Research work on High-temperature Transport Experiments in TaS₂
- Setup of high-temperature measurement probe
- 2008 *Summer Internship at EPFL (L. Forró group)*
Research work on Multi-walled Carbon Nanotubes Growth
- Catalyst synthesis and CVD growth
- SEM and TEM characterization of as-grown nanotubes
- 2009 *Summer Internship at EPFL (L. Forró group)*
Research work on the topics:
- Low-temperature Electron Spin Resonance in Graphite Intercalation Compounds
- 2010 *Summer Internship at Universität Wien (T. Pichler group)*
Research work on Optimization of Micro-Raman Spectrometer for Multi-mode Operation
- Raman spectroscopy of Single-walled Carbon Nanotubes

2009–2010

Teaching assistant at Budapest University of Technology and Economics

Subjects taught:

- Physics 1 & 2 for Electrical Engineering and Computer Sciences students
- Calculus 1 for Architecture students
- Physics lab exercises for Chemical Engineering and Environmental Engineering students

Publications

Publications

- *Identifying the electron spin resonance of conduction electrons in alkali doped SWCNTs*
M. Galambos, G. Fábíán, F. Simon, L. Čirić, L. Forró, L. Korecz, A. Rockenbauer, J. Koltai, V. Zólyomi, Á. Ruzsnyák, J. Kürti, N.M. Nemes, B. Dóra, H. Peterlik, R. Pfeiffer, H. Kuzmany, and T. Pichler
Phys. Status Solidi B **246**, 2760 (2009)
- *A broadband and high throughput single-monochromator Raman spectrometer: Application for single-wall carbon nanotubes*
G. Fábíán, C. Kramberger, A. Friedrich, T. Pichler, and F. Simon
Rev. Sci. Instrum **82**, 023905 (2011)
- *Adaptation of a commercial Raman spectrometer for multiline and broadband laser operation*
G. Fábíán, C. Kramberger, A. Friedrich, T. Pichler, and F. Simon
Phys. Status Solidi B **248**, 2581 (2011)
- *Density of states deduced from ESR measurements on low-dimensional nanostructures; benchmarks to identify the ESR signals of graphene and SWCNTs*
P. Szirmai, G. Fábíán, B. Dóra, J. Koltai, V. Zólyomi, J. Kürti, N.M. Nemes, L. Forró, and F. Simon
Phys. Status Solidi B **248**, 2688 (2011)
- *Testing the Elliott-Yafet spin-relaxation mechanism in KC_8 : A model system of biased graphene*
G. Fábíán, B. Dóra, Á. Antal, L. Szolnoki, L. Korecz, A. Rockenbauer, N.M. Nemes, L. Forró, and F. Simon
Physical Review B **85**, 235405 (2012)
- *Observation of conduction electron spin resonance in boron-doped diamond*
P. Szirmai, G. Fábíán, J. Koltai, B. Náfrádi, L. Forró, T. Pichler, O.A. Williams, S. Mandal, C. Bäuerle, and F. Simon
Physical Review B **87**, 195132 (2013)
- *g -factor anisotropy in nanowire-based InAs quantum dots*
S. d'Hollosy, G. Fábíán, A. Baumgartner, J. Nygård, and C. Schönenberger
AIP Conference Proceedings **1566**, 359-360 (2013)

Poster Contributions

- *Broadband modification of a high throughput commercial single-monochromator Raman spectrometer: Application for SWCNTs,*
G. Fábíán, C. Kramberger, A. Friedrich, T. Pichler, and F. Simon.
Poster at the 25th International Winterschool on the Electronic Properties of Novel Materials (Kirchberg-in-Tirol, AT), February 26 - March 05, 2011.
- *Cooper pair splitting and electron transport in superconductor hybrid nanostructures,*
J. Schindele, S. d'Hollosy, S. Nau, **G. Fábíán**, J. Samm, A. Baumgartner, M. Weiss and C. Schönenberger.
Poster at the 2nd NCCR QSIT General Meeting (Arosa, CH), February 1-3, 2012.
- *g-factor anisotropy in nanowire-based InAs quantum dots,*
S. d'Hollosy, **G. Fábíán**, A. Baumgartner, J. Nygård and C. Schönenberger.
Poster at the 31st International Conference on the Physics of Semiconductors (Zürich, CH), July 29 - August 3, 2012.
- *Magnetic and electrical tunability of InAs nanowire quantum dots,*
S. d'Hollosy, **G. Fábíán**, A. Baumgartner, J. Nygård and C. Schönenberger.
Poster at the Swiss NanoConvention 2013, Basel, CH, May 21-22, 2013.
- *g-factor anisotropy and spin transport in InAs nanowires,*
G. Fábíán, S. d'Hollosy, A. Baumgartner, J. Nygård and C. Schönenberger.
Poster at the 2013 QSIT Junior Meeting, (Passugg, CH), June 11-14, 2013.
- *g-factor anisotropy and spin valves in InAs nanowire quantum dots,*
G. Fábíán, S. d'Hollosy, A. Baumgartner, J. Nygård and C. Schönenberger.
Poster at the Frontiers in Quantum Engineered Devices (Obergurgl, AT), August 19-24, 2013.
- *Magnetic side gating and quantum charge pumping in InAs nanowires,*
G. Fábíán, A. Baumgartner, S. d'Hollosy, M. Jung, M. Madsen, J. Nygård, and C. Schönenberger.
Poster at the 5th NCCR QSIT General Meeting (Arosa, CH), January 7-9 2015.
- *Magnetoresistance of InAs nanowires with magnetic side gates,*
G. Fábíán, A. Baumgartner, M. Madsen, J. Nygård, and C. Schönenberger.
Poster at the 8th International School & Conference on Spintronics and Quantum Information Technology (SpinTech VIII) (Basel, CH), August 10-13 2015.

Talks

- *g-factor Anisotropy and Spin Transport in InAs Nanowire Quantum Dots*,
Talk at the 2013 QSIT Junior Meeting, (Passugg, CH), June 13, 2013.
- *Engineered Magnetoresistance in Quantum Dots for Cooper Pair Splitting*,
Invited Talk at NN Group Seminar at EPFL (Lausanne, CH), March 3, 2015.
- *Magnetic Side Gating of InAs nanowire Quantum Dots*,
Talk at Top-Spin international workshop (Salerno, IT), May 14, 2015.